

https://dspace.org/

Shock-induced flow through a pipe gap

Kapfudzaruwa, Simbarashe

2016-10-11
http://hdl.handle.net/10539/21159

Downloaded from a DSpace repository. https://dspace.org/

Shock-induced flow through a pipe gap

Simbarashe Kapfudzaruwa

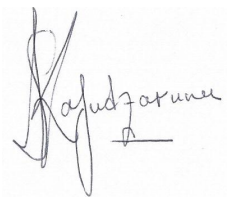
A dissertation submitted to the Faculty of Engineering and the Built Environment, University of the Witwatersrand, Johannesburg, in fulfilment of the requirements for the degree of Master of Science in Engineering.

Johannesburg, April 2016

Declaration

I declare that this dissertation is my own, unaided work, except where otherwise acknowledged. It is being submitted for the degree of Master of Science in Engineering in the University of the Witwatersrand, Johannesburg. It has not been submitted before for any degree or examination at any other university.

Signed this 22nd day of April 2016



Simbarashe Kapfudzaruwa

Acknowledgements

I would like to extend my gratitude to the following people without whom success of the project would have been realised:

- The Almighty for guiding me spiritually to achieve what I have succeeded in doing academically so far in my life.
- Prof Skews and Randall Paton for according me the opportunity to work under their intellectual guidance, mentorship, leadership and for their advice and faith in me as a young post graduate student.
- My mother Mrs. V Kapfudzaruwa who stood by me from my days in primary and high school after the passing away of my father in 1996 to whom I dedicate this dissertation.
- My uncles Mr M T Dzvimbo and Prof. K P Dzvimbo who took over responsibility for my education from my high school days to my studies at the University of Zimbabwe, University of Pretoria and the University of the Witwatersrand. I shall forever remain grateful to them.
- My sister Mrs. N Zembe and her husband; and my brother Dr F Kapfudzaruwa for their love, and financial support throughout my educational career
- Ms. Sharon Njila for her unwavering support and love during the trying times of my research work.

Finally I would like to thank staff in my department at the University of the Witwatersrand and in particular the staff in the Mechanical Engineering laboratory for the great assistance in the machining of my experimental testing facility and technical advice during my practical work.

Abstract

An explosive event in an industrial gas transmission pipe stresses the pipe and can result in pipe rupture and separation at weak points. A shock wave results propagating from the high pressure section of the pipe, through the gap and to the low pressure section. The present study simulates numerically and experimentally the resulting flow field at the position of pipe separation and propagation conditions in both pipe sections. The effects of gap width, gap geometry and shock Mach number variation are investigated. Shock Mach numbers of 1.34, 1.45,1.60 and 2.2, gap widths of 40mm to 310mm were used. All variations of boundary conditions were found to have an effect on the propagation conditions as well as the development of the flow features within the gap. The variation of the gap geometry was done for a pipe gap and a flanged gap experimentally. Extended geometries were simulated numerically. For the pipe gap, the incident shock wave accelerated the gas in the upstream pipe to high subsonic speeds and continued in the downstream pipe at a much reduced strength. A strong expansion propagated into the flow in the upstream pipe causing a significant pressure drop from the initial post-shock pressure. Expansion waves at the outflow resulted in supersonic speeds as the flow entered the gap for Mach 1.45 and 1.6. A notable feature was the formation of a standing shock at the inlet to the downstream pipe. In addition to the standing shock, shock cells of alternating shocks and expansions developed within the gap essentially controlling the propagation conditions in the downstream pipe. For the lower Mach number of 1.3, no sharp discontinuities were noticed. The effect of the gap width was found on the nature of the shock cells within the gap. The propagation conditions in the downstream pipe showed that the pressure is initially unsteady but becomes more uniform, controlled by the developed wave system in the gap. For the flanged gap case, the flow within the gap is confined for much longer and hence produced much more intense and complex flow feature interactions and an earlier transition of the flow to turbulence. Numerical investigations for a burst pipe gap, for a gap with a different diameter downstream pipe and a gap with a 90-degree bend downstream pipe produced peculiar flow features.

Published Work

Aspects of this dissertation have been published in the following references:

Kapfudzaruwa S., Skews B. W., and Paton R.T., "Shock-induced flow through a pipe gap", 30th International Symposium on Shock Waves, July 15 - 19, 2015 in Tel-Aviv, Israel

Contents

Declaration i

Acknowledgements ii

Abstract iii

Published Work iv

Contents v

List of Figures xii

List of Tables xvii

1 Introduction 1

1.1 Background 1

1.2 Problem Statement 2

1.3 Scope of Work 2

2 Literature Survey 3

2.1 Introduction 3

2.2 Shock tube flow 3

2.2.1 Wave propagation in a Shock tube 4

2.3 Shock wave diffraction 5

2.4 Shock wave reflection 6

2.5 Jet structure from an open pipe end 7

2.5.1 Underexpanded Jet 7

2.5.1.1 Intercepting shock 8

2.5.1.2 Prandtl-Meyer Fan 10

2.5.1.3 Jet shear layer 10

2.5.1.4 Vortex Ring 10

2.5.1.5 Second shock 10

2.5.1.6 Shock oscillations in an underexpanded jet - Work by J Panda 11

2.5.1.7 Circular pulse jets - Work by Ishii et al. 12

2.5.2 Supersonic jet impinging on a plate 12

2.6 Flow feature interactions 14

2.6.1 Shock-vortex interaction 14

2.6.2 Vortex ring leap frogging 15

2.6.3 Shock-shear layer interaction 15

2.6.4 Shock wave focusing 15

2.7 Compressible flow through a ruptured pipe - Work by Skews et al. 16

2.7.1 Stationary normal shock 17

2.7.2 Flow in the upstream and downstream pipe 18

2.7.3 Vortex ring leap frogging 18

2.8 Shock-boundary layer interaction under the influence of a normal suction slot - Work by Weiss and Olivier 19

2.9 Propagation and distortion of pressure waves in a pipeline 19

2.9.1 Effect of a flange gap on Shock tube performance - Work by A R Butcher 20

2.9.2 Propagation conditions and wave distortion - Work by Kim et al. . . . 20

2.10 Conclusion 20

3 Objectives **21**

4 Apparatus **22**

4.1 Introduction 22

4.2 Shock tube 22

4.3 Compressed Air Supply 25

4.4 Instrumentation 26

4.5 Shadowgraphy optical system 27

4.6 Diaphragms 28

5 Methodology **29**

5.1 Introduction 29

5.2 Numerical simulations 29

5.2.1 Governing equations 29

5.2.2 Computational domain 32

5.2.3 Meshing 33

5.2.4 Flow Solver Specifications 35

5.2.4.1 Models and Materials 35

5.2.4.2 Initial conditions . . . 35
5.2.4.3 Solution Methods . . . 35
5.2.4.4 Solution Controls . . . 35
5.2.4.5 Adaptive mesh refinement . . . 36
5.2.4.6 Time step size . . . 37
5.3 Experiments . . . 37
5.3.1 Diaphragm Calibration . . . 38
5.3.1.1 Pre-test actions . . . 39
5.3.1.2 Performing the test . . . 39
5.3.1.3 Post-test actions . . . 40
5.3.2 Flanged and Pipe Gap Experiments . . . 40
5.3.2.1 Pre-test actions . . . 41
5.3.2.2 Performing Test . . . 42
5.3.2.3 Post-test actions . . . 43

6 Data Processing **44**

6.1 Introduction . . . 44
6.2 General Observations . . . 44
6.2.1 Diaphragm Calibration . . . 44
6.2.2 Shock tube design validation . . . 45
6.2.3 Wave propagation in both pipes . . . 47
6.3 Data Processing . . . 48
6.3.1 Experimental Data Processing . . . 48

6.3.1.1 Diaphragm Calibration 48

6.3.1.2 Wave propagation in both pipes 49

6.3.1.3 Experimental flow visualisation 50

6.3.2 CFD Data 50

7 Results **52**

7.1 Introduction 52

7.2 CFD Validation 52

7.3 Diaphragm calibration 54

7.4 Transient flow in the upstream and downstream pipe 55

7.4.1 Upstream pipe flow 55

7.4.2 Downstream pipe flow 56

7.4.3 Effect of gap width and shock Mach number 58

7.5 Experimental flow visualisation 61

7.5.1 Pipe gap 61

7.5.2 Flange Gap 61

7.6 CFD Results 64

7.6.1 Pipe gap 64

7.6.2 Flange gap 65

8 Discussion **68**

8.1 Pipe gap 68

8.1.1 Effect of Mach number 68

8.1.2 Effect of gap width 72

8.2 Flange gap . . . 73
8.2.1 Effect of Mach number . . . 73
8.2.2 Effect of gap width . . . 73
8.3 Comparison of flange gap and pipe gap flow . . . 75
8.3.1 Effect on the vortex ring behaviour . . . 76
8.3.2 Effect on the jet structure . . . 77
8.4 Gap Flow Features . . . 79
8.4.1 Standing Shock . . . 79
8.4.2 Second Shock . . . 79
8.4.3 Barrel Shock . . . 80
8.5 Flow feature Interactions . . . 82
8.5.1 Shock-vortex interactions . . . 82
8.5.2 Vortex ring leapfrogging . . . 83
8.6 Extended geometry simulation . . . 84
8.6.1 Burst Pipe Simulation . . . 85
8.6.1.1 Development of the flow . . . 85
8.6.1.2 Shock structure . . . 86
8.6.2 Different pipe diameter simulation . . . 89
8.6.2.1 Development of the flow . . . 89
8.6.2.2 Shock-vortex interaction . . . 90
8.6.2.3 Shock focusing . . . 90
8.6.3 Shock propagation into a 90 degree bend . . . 91

8.6.3.1 Development of the flow 91

9 Conclusions **93**

10 Recommendations **95**

A Digital Appendix **98**

B Technical specifications **99**

C Supplementary experimental pressure-time profiles **101**

D Diaphragm calibration **103**

E Mach number uncertainity **104**

F Engineering drawings **105**

List of Figures

2.1 Wave diagram at the open end of a shock tube.[7] 5

2.2 Schematic diagram of a shock wave diffracting at an open pipe end. 6

2.3 Schematic of a regular to Mach reflection transition. 6

2.4 Underexpanded jet from a pipe end. 8

2.5 Underexpanded jet with the periodic nature. 8

2.6 Shock pattern in an underexpanded jet. 9

2.7 Formation of an Intercepting shock in an underexpanded jet. 9

2.8 Propagation of a vortex ring from a shock tube open end. 11

2.9 Five-exposure shadowgraph of an unsteady standing shock.[8] 13

2.10 Typical shock-vortex interaction of a strong shock and a strong vortex.[16] . . 14

2.11 Vortex ring leap frogging[11]. 16

2.12 Schematic of shock wave focusing for a two-dimensional axisymmetric flow. . 17

2.13 Developed standing shock at downstream pipe inlet for a 20mm and 30mm pipe gap.[12] 17

2.14 Pressure contours for the flow development to steady state in the upstream and downstream pipe.[12] 18

4.1 Schematic for the piping arrangement for the pipe gap geometry. 23

4.2 Schematic for the piping arrangement for the flanged gap geometry. 23

4.3 Isometric view for the pipe arrangement for the pipe gap. 24

4.4 Isometric view for the pipe arrangement for the flange gap. 24

4.5 Shock tube supports. 25

4.6 Air cylinder with pressure regulator valve 26

4.7 Controlboard for pressure regulation 26

4.8 Instrumentation components. 27

4.9 Monochrome schlieren optical system setup 28

5.1 Moving and stationery reference frames for unsteady shock wave motion. . . . 31

5.2 Computational domain. 33

5.3 Initial mesh for a burst pipe simulation showing the sphere of influence. . . . 34

5.4 Tracking of refinement of the shock front and its reflection at different time steps. Images at 0.20ms apart. 37

6.1 Diaphragm calibration. 45

6.2 CFD pressure contours for a 30mm pipe gap at Mach 1.45. From the top, flow time at 6ms, 6.5ms and 7ms respectively. 46

6.3 Voltage-time trace for a pipe gap of 310mm at Mach 1.45. 47

7.1 Comparison of experimental shadowgraphs(upper half) and numerical shadowgraphs(lower half) for 40mm gap Mach 1.6. 53

7.2 Comparison of experimental shadowgraphy(upper half) and numerical density contours(lower half) results for 40mm gap Mach 1.6. 53

7.3 Comparison of experimental shadowgraphs(upper half) and numerical shadowgraphs(lower half) for 80mm gap Mach 1.6. 54

7.4 Diaphragm calibration. 55

7.5 Pressure time profiles for a pipe gap of 60mm Mach 1.45. 56

7.6 CFD pressure plots for 60mm pipe gap at Mach 1.45. 57

7.7 Pressure time profiles for 60mm pipe gap at Mach 1.6. 58

7.8 60mm pipe gap at Mach 1.3 pressure-time profiles. 59

7.9 Pressure time profiles for 180mm pipe gap at Mach 1.45. 60

7.10 Effect of shock Mach number and gap width on downstream pipe flow. 60

7.11 Early stages of propagation of a shock wave through a 40mm pipe gap at Mach 1.45 62

7.12 Later stages of propagation of a shock wave through a pipe gap of 40mm at Mach1.45 63

7.13 Early stages of propagation of a shock wave through a 50mm flanged gap at Mach 1.45 63

7.14 Later stages of propagation of a shock wave through a 50mm flanged gap at Mach1.45 65

7.15 CFD pressure plots for a 80mm pipe gap at Mach 1.60 66

7.16 CFD velocity plots for a flanged gap of 80mm at Mach 1.45. Images at 0.15ms apart. 67

8.1 Flow development for a pipe gap of 40mm at Mach 2.2 69

8.2 40mm pipe gap at Mach 2.2 flow at early stages. SL-Jet boundary, PV-Primary vortex ring, SV-Second vortex ring. 70

8.3 Flow development for a pipe gap of 40mm at Mach 1.60 70

8.4 Flow development of a 40mm pipe gap at Mach 1.30. 71

8.5 Vortex ring interaction for a 40mm pipe gap at Mach 1.3. 72

8.6 Effect of gap width at Mach 1.6. From left to right 40mm, 50mm and 60mm. 73

8.7 Effect of gap width at Mach 1.6. 80mm for the first two frames and 115mm for the last two frames. 73

8.8 Effect of Mach number for a 50mm flanged gap. Mach 1.45 for two images on the left and Mach 1.3 for the latter two. 74

8.9 Effect of Mach number on shock-vortex interaction for a 50mm flanged gap. Mach 1.45 for the first two images on the left and Mach 1.3 for the last two. . 74

8.10 Effect of flange gap width. 50mm for images in the first row and 80mm for the images in the second row. 75

8.11 Effect of flange gap width on transition to turbulence. 50mm for the image on the left and 80mm for the image on the right. Both cases at Mach 1.45. . . . 76

8.12 Effect of gap geometry on shock-vortex interaction. 80mm pipe-gap on the left and 80mm flanged gap on the right. Both cases at Mach 1.45. 77

8.13 Effect of gap geometry on standing shock structure. 40mm pipe-gap on the left and 40mm flanged gap on the right. Both cases at Mach 1.45. 78

8.14 Downstream pressure profiles on the left. Shadowgraphs on the right for 40mm pipe gap at Mach1.45 and Mach 1.30 respectively. 80

8.15 Formation of a second shock for 40mm Mach 1.6. CFD velocity plot on the left and shadowgraph on the right. PV-primary vortex ring, SS-second shock. 80

8.16 CFD density plot showing formation of a barrel shock for 80mm Mach 1.6. *BS*-Barrel shock, *EF*-Expansion fan. 81

8.17 Variation of Barrel shock angle with Mach number. Image for 60mm Mach 1.6 on top and 60mm Mach 1.45 on the bottom. 82

8.18 CFD velocity plots for 80mm pipe gap Mach 1.6 showing vortex ring leapfrogging process. 83

8.19 CFD velocity plots for 40mm pipe gap Mach 1.6. *SL*-Separation line, *ES*-Embedded shock. Images at 0.07ms apart 84

8.20 Shadowgraphs for 40mm pipe gap at Mach 1.45. *VS*-Toroidal shock. 85

8.21 Iso-vorticity surfaces for primary and secondary vortex ring. Images taken at 0.20ms apart. 86

8.22 CFD density plot showing flow development for a 30mm gap burst pipe at Mach 1.6 87

8.23 Developed shock system at later times for a 30mm burst pipe gap at Mach 1.6. 88

8.24 CFD velocity plot showing the shock structure in the 30mm burst pipe gap at Mach 1.6 88

8.25 CFD density plot for Mach 1.6 shock expanding from a 50mm diameter pipe into a 150mm diameter pipe. Images at 0.2ms apart 90

8.26 CFD density plot for shock-induced flow past a 30mm gap into a pipe bend. Images at 0.2ms apart 92

List of Tables

4.1 Relative positions for the pressure transducers 23

5.1 Boundary conditions for Mach 1.60 33

5.2 Specifications for initial mesh 34

5.3 Convergence criteria for different solution variables residuals 36

5.4 Adaptive mesh refinement parameters 36

5.5 Boundary conditions for experiments 38

7.1 Variation of Mach number for different diaphragm bursts 55

B.1 Specifications for Pressure transducers 99

B.2 Specifications for Oscilloscope 99

B.3 Specifications for transducer signal conditioners 99

B.4 Specifications for the high-speed camera 100

B.5 Specifications for the light sources 100

B.6 Specifications for the optical mirrors 100

B.7 Specifications for the electro-delay box 100

D.1 Diaphragm calibration 103

E.1 Individual uncertainties for Mach number calculation 104

1 Introduction

1.1 Background

Shock tubes have been used extensively as valuable gas dynamic instruments in studies of flow field features and shock wave dynamics in compressible duct flows. They have been a basic tool in the understanding of compressible flows in ducts. One of these compressible flow studies relates to the propagation of pressure waves and the ensuing flow features through a gap in a pipeline with the use of a shock tube facility.

An explosive event in a high pressure industrial gas pipe is a practical example were compressible flow through a pipeline gap can occur. The initial explosive event will result in stress loading of the structural material of the pipe. A stress wave results propagating down the piping material at high speeds and could result in pipe rupture, or bolt failure at flanges, causing them to separate. This is then followed by a relatively slower shock wave propagating through the gas from the high pressure pipe section, through the gap and down the low pressure section.

Studies on the nature and behaviour of blast waves have mainly focused on their mitigation following an explosion. This has been done on mitigating blast wave loading effects on architectural structures and on human skull models. Another avenue has been the study of the dynamics of blast waves in the suppression of booms from shock tubes in the laboratory, optimal designs of mufflers for automobile engines and reduction of sonic booms in the high-speed train/tunnel problem.

Despite the dangers associated with effects of blast loading on a high pressure gas pipeline, not many studies have focused on this phenomena. The only study that simulated a flow field through a pipe gap following an explosive event in a gas pipeline was an experimental and numerical study by Skews et al.[12]. The boundary conditions in the study by Skews were limited to an incident shock Mach number of 1.5 for a circular pipe. The gap sizes which were used were 10mm, 20mm and 30mm for both the flanged and pipe gap. Complex features observed could not be fully explained over the limited range.

During the study it was noticed that the flow field within the gap had an influence on the development of the flow field in both the upstream and downstream pipe. The exact nature of the influence could not be ascertained from the study as the experimental investigation was primarily at the position of pipe separation and not in the upstream and downstream pipes.

1.2 Problem Statement

From the background study above, an investigation of the flow features and their interactions within the pipe gap have been done over a limited range of boundary conditions. The effects of gap geometry, gap width and shock Mach number were not done over extended ranges. The studies have been limited to the gap flow field and not explored the propagation conditions in the upstream and downstream pipe and their relationship with the gap flow.

1.3 Scope of Work

In chapter 2 a literature review will be presented on the work by Skews et al.[12]. Studies exhibiting similar flow features will also be reviewed. In chapter 4, details will be provided of the experimental set-up used. This will include details on the shock tube facility, the flow visualisation system and instrumentation. In chapter 5 the research methodology is presented. This will include details for the procedures for numerical simulations and experimental work. Data processing of the primary results will also be covered in chapter 6. In chapter 7, results will be presented for the numerical simulations and the experimental work. In chapter 8, the results are explained and discussed. The study will be concluded in chapter 9 and recommendations for future work are given in chapter 10.

2 Literature Survey

2.1 Introduction

Shock-induced flow through a gap in a pipeline is quite a novel research field. Although explosions in industrial gas pipelines and the resulting flow field can cause serious damage, researchers have mostly focused on shock-induced flow at an open pipe end. This has been brought about mainly by the study of blast waves and its mitigation from gun muzzles, high speed train tunnels and engine exhausts.

Previous literature on explosive-related phenomena and its mitigation in industrial gas transmission pipes have taken slightly different approaches. The past studies have not simulated the initial blast loading on the piping material and the eventual failure and separation of pipes at structurally weak points. The planar shock waves have been simulated to propagate in continuous uniform cross-section pipes with only an open end.

The shock wave on exiting the open end pipe, the flow features in the previous studies resemble some that result in the pipe gap of the present study. Therefore this chapter will review some of the previous work. Some fundamental concepts relating to shock tube flow are reviewed first however.

2.2 Shock tube flow

The shock tube is an instrument used to study compressible flow related phenomena. Shock tubes have been used extensively as a valuable gas dynamic instrument in studies of flow field properties and shock wave dynamics in duct flows. They have been a basic tool in the understanding of compressible flow in ducts. More recently, shock tubes have been used in biomedical research to study how biological specimens are affected by blast waves. In this case they replicate and direct blast waves at a sensor or a model in order to simulate actual explosions and their effects, usually on a smaller scale.

The conventional shock tube consists essentially of a uniform tube divided initially by a diaphragm into two compartments containing gases at different pressures. A shock tube might be open or closed at its end depending on its application. When the diaphragm is ruptured by means of a needle or an electric spark, a normal shock wave moves into the low pressure part of the tube and an expansion wave moves into the high pressure part. The expansion is propagated in the form of a rarefaction wave of finite extent. The head of the rarefaction wave travels with the speed of sound in the high pressure compartment, whilst the tail moves with the speed of sound relative to the fluid. Between these two disturbances, there may be regions in which the gas moves with uniform subsonic, sonic or supersonic speed depending on the initial pressure ratio across the diaphragm. The strength of the shock and the Mach numbers in the low pressure part depend on the initial pressure ratio across the diaphragm. The Mach number of the flow behind the shock wave reaches a limiting value for an infinite shock strength. For $\gamma = 1.40$, this limiting Mach number is 1.89. The duration of steady flow in the low and high pressure regions is limited to times of the order of milliseconds in tubes of reasonable length by reflections of the shock and expansion waves from the ends of the tube.

2.2.1 Wave propagation in a Shock tube

The motion of the shock waves and expansion waves in an open end shock tube is conveniently described with reference to Figure 2.1. These are typical wave diagrams occurring in the vicinity of the open end of a tube. The time, t, that has elapsed since the diaphragm was ruptured is plotted against the pressure, p, at different measuring points. It is assumed in this wave diagram that the same gas was originally contained in the high and low pressure compartments, and that the temperatures in these compartments were initially equal. When the diaphragm is ruptured, a normal shock propagates from left to right and results in the pressure variations at the measuring points 1 and 2. The static pressure suddenly rises when the normal shock passes over the measuring points and remain constant, corresponding to the static pressure just behind a normal shock. Decrease in the static pressures at the two measuring points is due to the reflected expansion wave from an open end of the tube. The line that connects the same pressure p_H values in the two wave diagrams indicates a head of the expansion fan reflected from the open end of the tube, while the line that connects the same pressure p_T values presents a tail of the expansion fan. These lines are extended to meet each other at the location of e away from the tube exit. The distance e is known as the open end correction e. The open end correction was shown to be necessary by Kim et al.[7] at the open end of the shock tube.

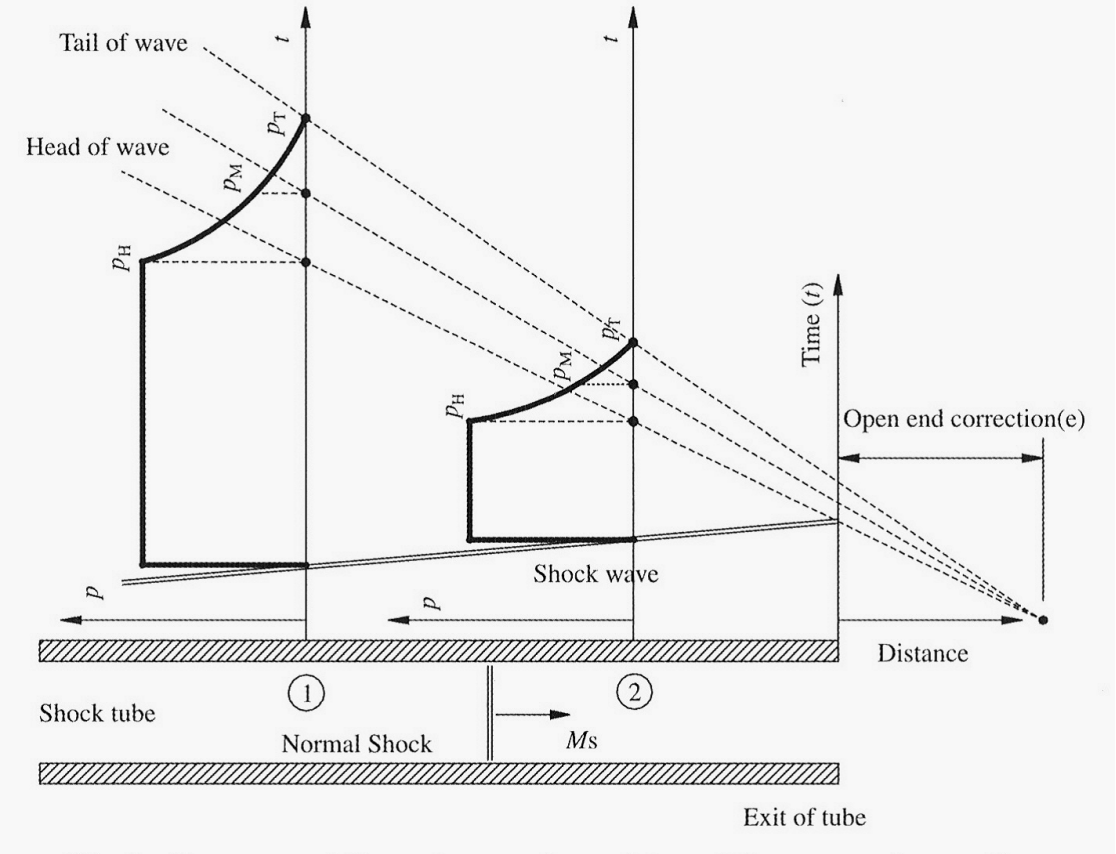


Figure 2.1: Wave diagram at the open end of a shock tube.[7]

2.3 Shock wave diffraction

Another phenomena that occurs when a shock wave exits a pipe is shock wave diffraction. Figure 2.2 illustrates diffraction of a shock wave discharged from a pipe end. IT is the normal shock wave, TR is the expansion wave and TC is the diffracted shock wave, where the flow behind the incident shock is subsonic. In the early stages when the shock discharges from the pipe, the shock is almost normal. As time elapses, the shock is diffracted by interfering with the expansion wave generated at the lip of the pipe. This expansion, as it spreads towards the tube axis, interferes with the shock wave. In this process the shock wave is diffracted more and finally becomes spherical in shape. This is similar to what was pointed out by Abe and Takayama[1], whereby a shock wave exiting a pipe end diffracts into a spherical shape once the curved expansion fan behind the shock coalesces at the axis of symmetry.

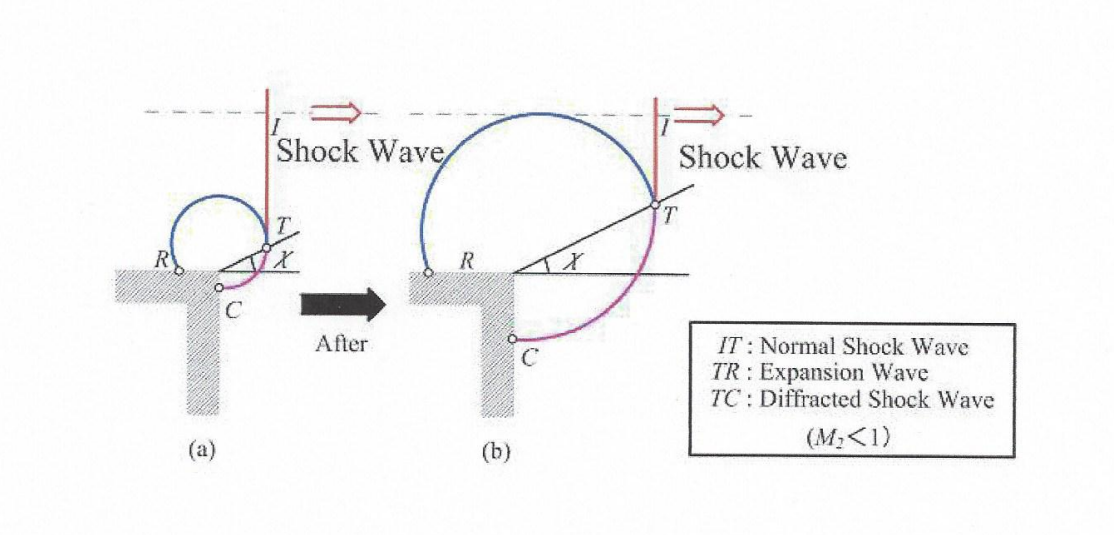


Figure 2.2: Schematic diagram of a shock wave diffracting at an open pipe end.

2.4 Shock wave reflection

An incident shock wave on a solid wall results in the occurrence of a regular or a Mach reflection. In practical flow fields both types of shock reflection can be observed. A change in the angle between the shock wave and the rigid wall will result in a transition in the reflection type. A typical transition from a regular to a Mach reflection is shown schematically in Figure 2.3.

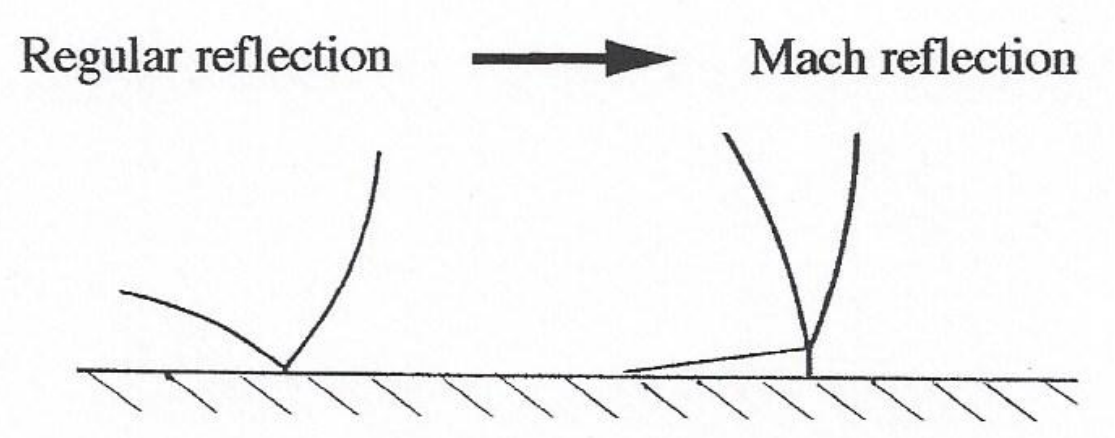


Figure 2.3: Schematic of a regular to Mach reflection transition.

2.5 Jet structure from an open pipe end

As a shock propagates in a shock tube, a mass motion of fast moving gas is induced behind the shock. Upon exiting the shock tube, the shock diffracts and behind it the gas expands and develops into a pulse jet. In the initial stages of flow development of shock-induced flow through a pipe gap, similar flow features are common to those in a pulse jet. Therefore a good understanding of the jet structure from a normal open pipe end is fundamental. This will help explain the initial flow features and their subsequent interactions as the flow develops within the gap.

Depending on the shock Mach number, the gas can exit supersonically or expand to supersonic speeds locally within the pipe gap. The structure of the resulting supersonic jet in both cases is mainly governed by the conditions to which the gas expands to. In the case of the flow from the pipe end, this will be the ambient pressure the gas expands to. If the ambient pressure is more than the exit plane pressure of the jet, an underexpanded jet develops. If the ambient pressure is less than the exit plane pressure of the jet, an overexpanded jet develops.

2.5.1 Underexpanded Jet

The structure of an underexpanded jet exiting from a pipe end is shown in Figure 2.4. It shows the essential flow features of an underexpanded jet near the exit of the pipe.

An underexpanded jet exhausting supersonically into still air has been known to exhibit a periodic or chain-like structure at least as early as the observations of Rayleigh[13] in 1879. A similar periodic jet structure is approached in the pipe gap flow as the gaps get relatively larger. Rayleigh and many others have offered explanations for and elaborated upon the manner in which the expansion and compression waves within a free jet form the periodic patterns at low jet pressure ratios and the not so periodic patterns at high jet pressure ratios. This axisymmetric periodic structure has several complex features. In the periodic pattern jet, the jet boundary oscillates as the underexpanded jet gas periodically overexpands and re-converges in its attempt to match the ambient pressure. The gas continually overshoots the equilibrium position because the effects of the boundary arc communicated to the interior of the jet by sound waves, which, by definition, travel more slowly than the bulk supersonic flow. The characteristic paths of the sound waves converge to form the network of criss-crossed shock waves, or shock diamonds. These standing shocks alternate with rarefaction fans. The gas in the jet interior expands and cools as it flows through the rarefaction fans and is compressed and heats as it passes through the shock diamonds. Figure 2.5 shows the

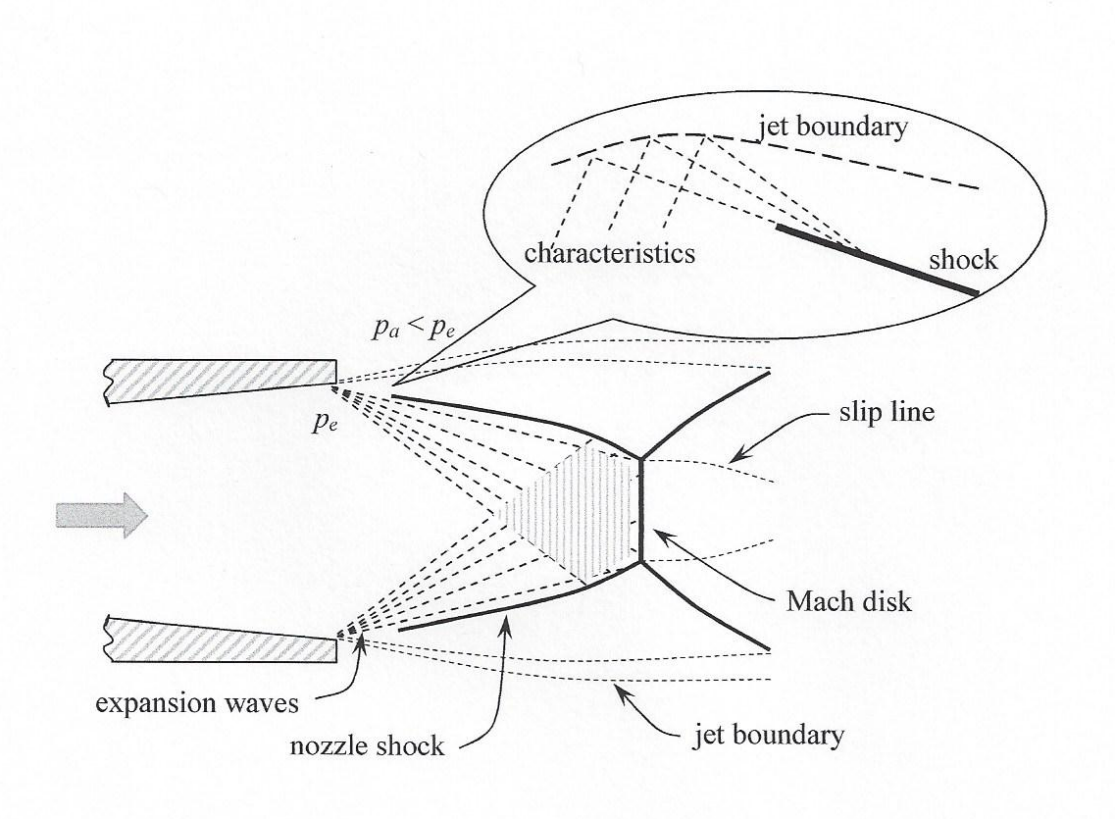


Figure 2.4: Underexpanded jet from a pipe end.

periodic nature of an underexpanded jet. The figure clearly illustrates that the jet interior is always out of step with the jet boundary.

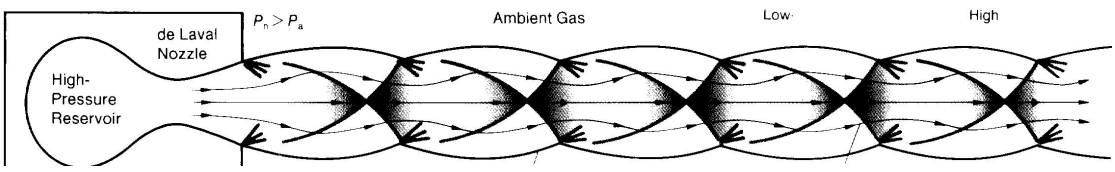


Figure 2.5: Underexpanded jet with the periodic nature.

2.5.1.1 Intercepting shock

As a supersonic jet is emitted from a nozzle with an exit plane pressure which is higher than the ambient pressure, the underexpanded jet expands to match the ambient pressure. At the rim of the opening there occurs an expansion fan tending to lower the pressure of the gas to that of the ambient surroundings, but somewhere along the outer periphery of these waves a shock front develops which cuts across them and intercepts them. The extent of the spreading of the jet boundary is a function of the pressure of the jet at the pipe exit. The larger the pressure of the jet at the pipe exit, the larger the jet expansion into the ambient

surroundings once it leaves the pipe. If the exit plane pressure is reduced then the shock front remains at the pipe lip. Hence there is a continuous transition from intercepting shock fronts to shock fronts formed when the jet is overexpanded in nature. A schematic of the shock pattern commonly found in an underexpanded supersonic gas jet is shown in Figure 2.6.

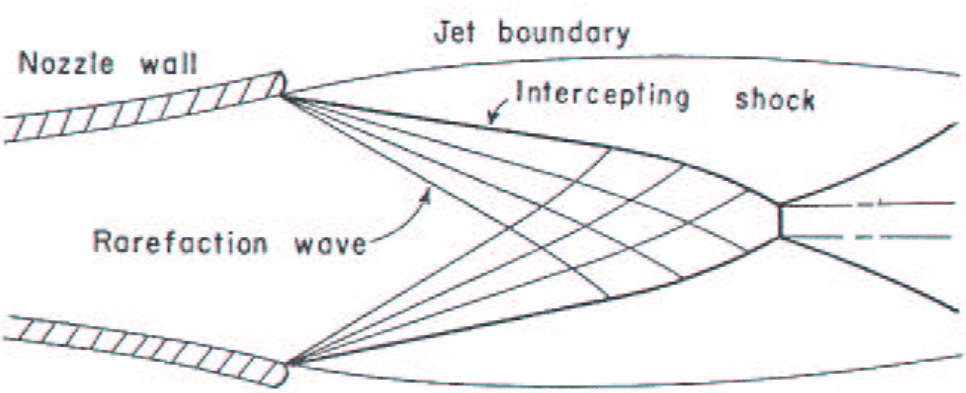


Figure 2.6: Shock pattern in an underexpanded jet.

Courant and Friedrichs[3] suggested the possible reasons for the formation of intercepting shocks which is also known as a Barrel shock. The flow continues uninfluenced by the ambient state until it meets the first Mach line issuing from the pipe exit, i.e. the leading edge of the expansion wave. Owing to the divergence of the jet the pressure decreases along the axis. Across the expansion wave the pressure decreases until it drops below the ambient pressure. Hence there is a pressure gradient existing from the jet boundary where the pressure is equal to the ambient pressure. This will cause an inward curvature of the jet. All the Mach lines issuing from the the jet boundary have the same angle with the jet boundary, since at the boundary the pressure, hence the sound speed and velocity remain constant. Hence these Mach lines would tend to converge with the converging jet and would have an envelope unless they were to be cut off by an intercepting shock as shown by Figure 2.7 below. Thus an intercepting shock would have to exist to prevent the formation of the above mentioned envelope.

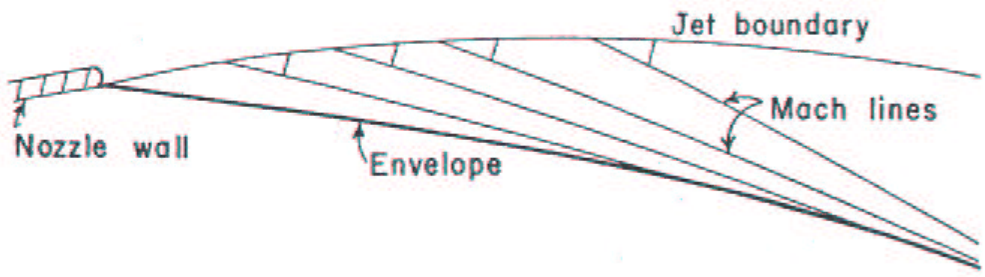


Figure 2.7: Formation of an Intercepting shock in an underexpanded jet.

2.5.1.2 Prandtl-Meyer Fan

When a supersonic flow is turned away from itself a Prandtl-Meyer expansion fan forms as a series of characteristics. A similar flow feature forms at a shock tube end when a supersonically accelerated gas in the gap is turned away from itself. This happens when the jet issuing from the upstream pipe is underexpanded. To expand the gas to the ambient pressure a Prandtl-Meyer expansion fan forms at the lip of the upstream pipe.

2.5.1.3 Jet shear layer

The shear layer originates at the corner of the pipe. The shear layer is due to the separation of the gas and is brought about by the inability of the boundary layer of the upstream flow to negotiate the corner. The shear layer is a narrow region in which the high velocity gas issuing from the pipe interacts with the almost stationery gas at the pipe end. The shear layer is essentially straight and radial as it issues from the pipe corner. One end of the shear layer originates at the pipe corner and the other end embedded in the vortex. The angle at which the shear layer occurs depends on the ratio of the exit plane pressure to the pressure the gas expands to.

2.5.1.4 Vortex Ring

When a shock wave exits a pipe, the impulsively started flow results in an unsteady boundary layer separation at the pipe exit. Further on, the boundary layer rolls up and forms a separated vortex ring. The name 'ring' is as a result of the characteristic shape for a three-dimensional axisymmetric flow. For shock-induced flow, they are referred as 'compressible vortex rings' since they move at considerably higher velocities. Upon generation, the vortex ring evolution is influenced by factors such as cross-sectional shape of the pipe end and initial conditions of the driver. Figure 2.8 shows schematically the formation and propagation of a vortex ring at an open pipe end.

2.5.1.5 Second shock

The so called second shock, is the shock with one end attached to the vortex ring and is in the plane of the vortex ring. As the jet exits the pipe it expands and goes supersonic in the gap. The supersonic flow sees a reduced cross-sectional area through the vortex ring and adverse pressure gradient and the second shock forms in the jet. This implies the second shock forms even if the flow exits the pipe subsonically. The second shock is swept downstream with the

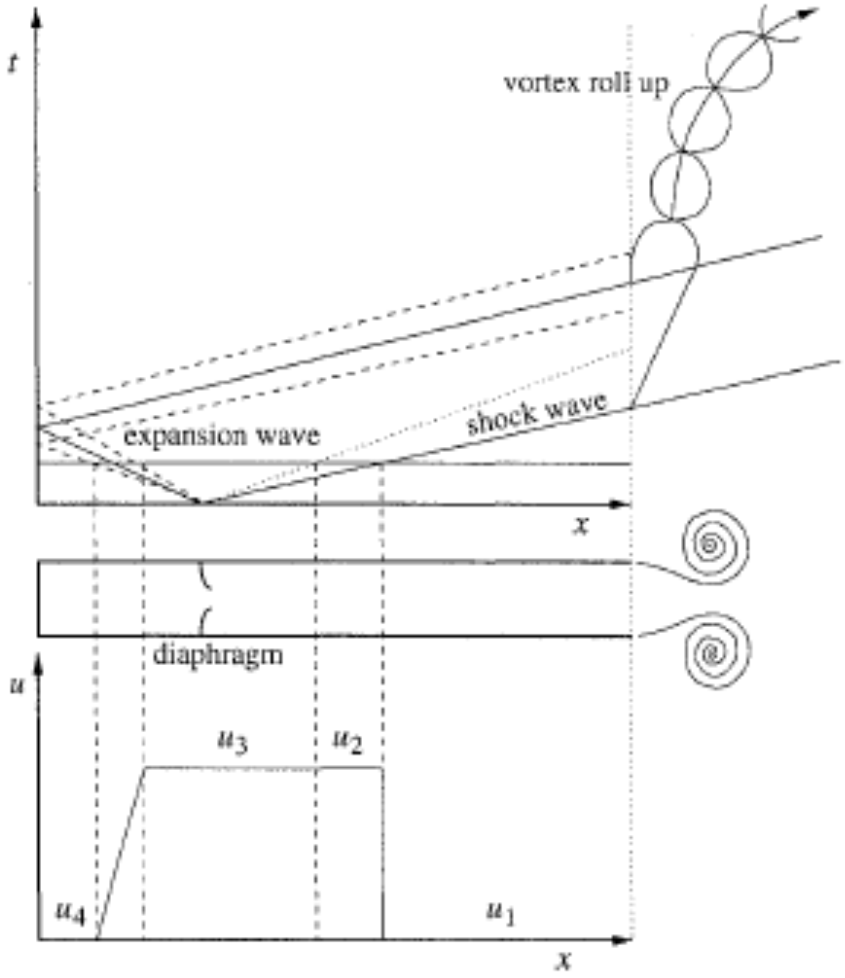


Figure 2.8: Propagation of a vortex ring from a shock tube open end.

vortex. Endo and Iwamoto[4] detailed the mechanism of the formation of the second shock. Sun and Takayama[14] outlined the flow conditions necessary for the formation of a second shock behind a diffracting shock.

2.5.1.6 Shock oscillations in an underexpanded jet - Work by J Panda

Shock-associated noise has been associated with the oscillation of the shocks in a supersonic jet. Passing of sound waves (from shock-shear layer interactions) cause periodic pressure perturbations and cause oscillation of the shocks in the jet. Panda[10] investigated the periodic oscillation of the shock waves in screeching underexpanded supersonic gas jets issuing from a choked axisymmetric nozzle at fully expanded Mach numbers of 1.19 and 1.42. The investigation was performed experimentally and through analytical means. The experimentation was performed using standard schlieren photography and a new shock detection technique

that depends on the scattering of laser light by shock waves. The scattered light is sensed by a photomultiplier tube (PMT). The time averaged and phase averaged statics of the PMT data revealed significant insight into the motion of the shock wave within the jet core. It was observed that the shocks oscillated more in the jet core and the least in the jet shear layer.

2.5.1.7 Circular pulse jets - Work by Ishii et al.

Unsteady circular jets were investigated experimentally and numerically for a wide range of jet strength by Ishii et al.[5]. In their studies, they described three types of exit conditions for a pulsed jet. They showed their dependence on the initial pressure ratio in the shock tube p_4/p_1, where p_4 is the initial driver pressure and p_1 is the initial driven pressure. In their analysis, they concluded that the exit conditions fall into three categories.

1. Subsonic matched jets for $1 < p_4/p_1 < 4.1$
2. Sonic underexpanded jets for $4.1 < p_4/p_1 < 41.2$
3. Supersonic underexpanded jets for $p_4/p_1 > 41.2$.

After a sudden gas outflow, it was observed that there are several stages in the subsequent time evolution of a sonic or supersonic underexpanded jet. The first stage is the diffraction of the first shock round the end corner. The second stage is the formation of an unsteady Mach disk or a normal shock. Even in a jet which does not have a quasi-steady Mach disk, an unsteady Mach disk can be formed, at least temporarily. The third stage is the formation of the first shock-cell structure. This stage is strongly affected by the presence of the first vortex and the Mach disk. After the connection between the second shock and the reflected shock is broken, the shock-cell length becomes maximum and thereafter it tends to shrink to a certain asymptotic size. The jet with a strong Mach disk is very unstable and rapidly breaks up. The jet tip is folded back on itself and is entrained into the first vortex ring and the jet soon evolves to a fully developed turbulent flow. At least up to $500\mu s$, circular jets with 2 cm diameter experience a substantially axially symmetric time evolution.

2.5.2 Supersonic jet impinging on a plate

Supersonic jets impinging on a solid structure were studied by Konstantin Vladimirovich Klinkov[8]. In the impingement zone just upstream of the solid structure, an unsteady standing shock developed. The unsteady behaviour of the standing shock was studied by a newly developed method of multi-exposure photography. The motion of the standing shock wave

ahead of the solid structure was detected by combining several light pulses with different time parameters. In order to observe the relatively slow motion of the shock wave, sequences of 5 pulses (duration: 100 ns) with time intervals betweens the pulses ranging from 2 to 10 s were applied . A typical shadowgraph image of the unsteady standing shock that was obtained with five light pulses, is shown in Figure 2.9 below.

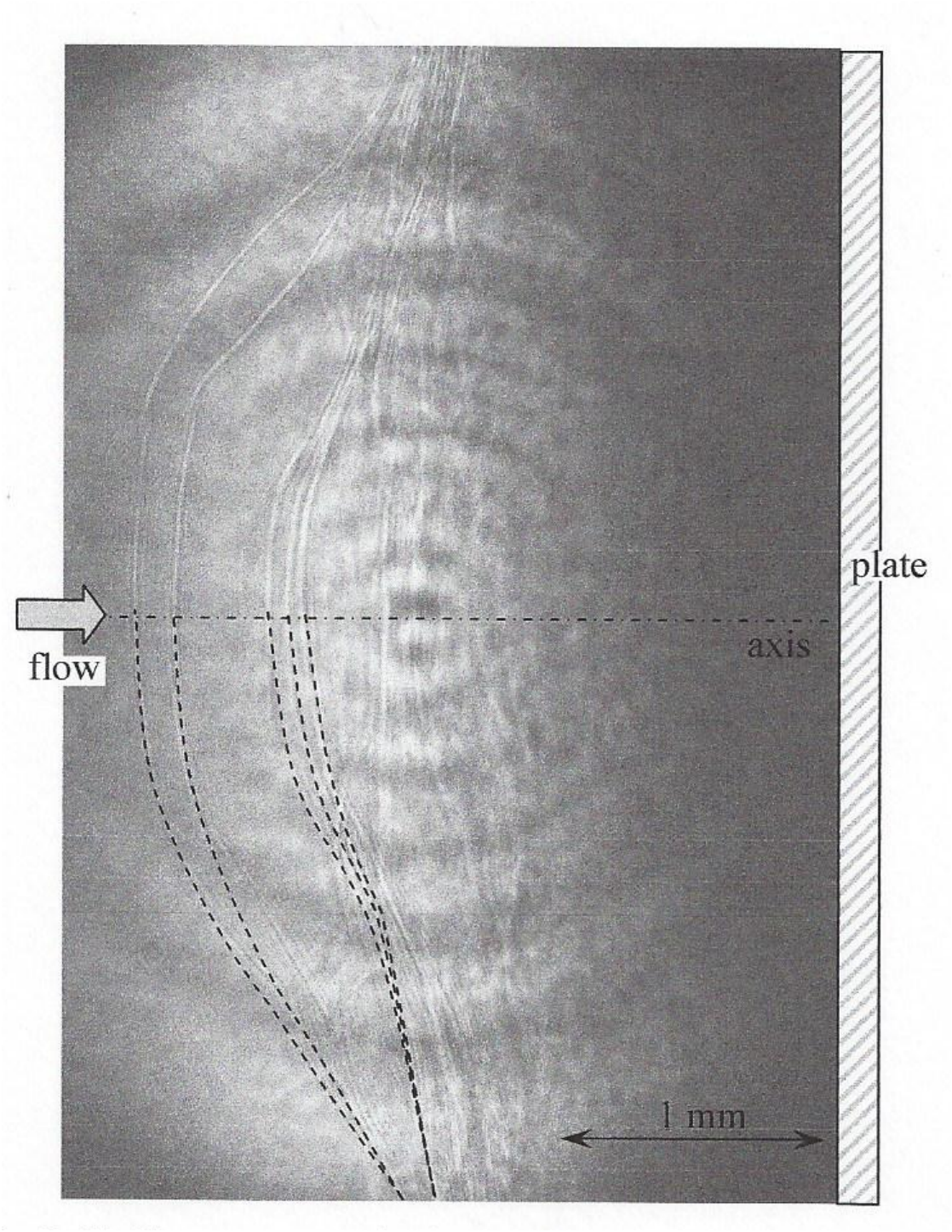


Figure 2.9: Five-exposure shadowgraph of an unsteady standing shock.[8]

Oscillation in the position of the standing shock was observed. A synchronized pressure measurement on the surface of the solid structure linked the pressure variation with the oscillating position of the standing shock.

2.6 Flow feature interactions

The basic flow features described in section 2.5 do interact in practical flow fields. In shock induced flow from a pipe these interactions mainly influence the evolution of the flow to steady state. These will be briefly outlined below.

2.6.1 Shock-vortex interaction

The study of shock-vortex interactions has been a fertile field of investigation for several decades. The interaction of a vortex and a shock wave is a major flow interaction in pipe gap flow. The interaction is a result of the vortex from the upstream pipe interacting with the reflected shock wave from the downstream pipe. In some cases the interaction is a major source of noise. The effect of the interaction on the shock profile and vortex distortion depends strongly on the relative strengths of the shock and the vortex. If the vortex is weak relative to the shock, there is no significant distortion of the shock front. A strong vortex however, distorts both a weak and a strong shock in such a way that the structure of the transmitted shock is much more complex. A typical interaction of a strong shock and a strong vortex interaction was investigated by Zhang et al.[16] and is shown in Figure 2.10. It shows the interaction of a strong shock wave and a strong vortex. An incident shock distorts into an S shape. At a later time, the incident shock splits into its two components *S1* and *S2*. Reflected shocks *R1* and *R2* emanate from the shock-vortex interaction.

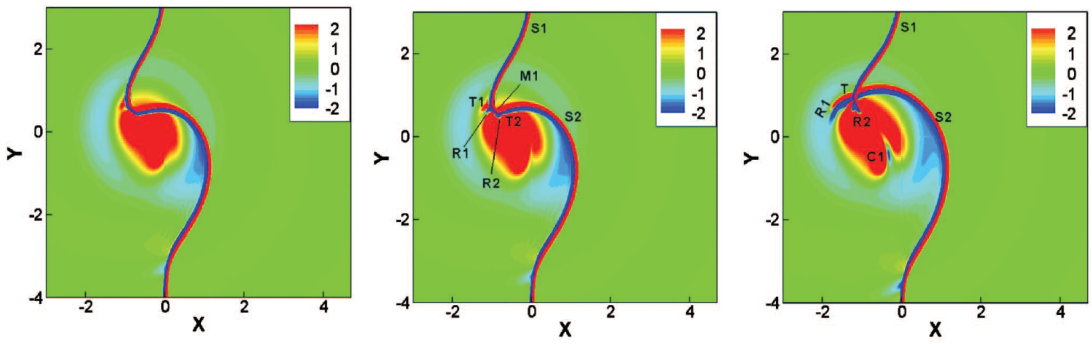


Figure 2.10: Typical shock-vortex interaction of a strong shock and a strong vortex.[16]

2.6.2 Vortex ring leap frogging

In shock induced flow through a pipe gap, diffraction of the incident shock at the downstream pipe can produce a second vortex ring. This can lead to a phenomenon known as vortex ring leap frogging between the two vortex rings. This is whereby vortex rings roll over one another. In general, vortex leap frogging occurs when two vortices in close proximity share the same axis. In terms of the properties of the vortices, the velocity, diameter and evolution of each vortex plays a role in influencing the nature of leapfrogging. The size ratio of the vortices dictates how long the leap frogging carries on for. The critical ratio was determined to be $3 + 2\sqrt{2}$ (equal to 5.83) by Love[9]. This ratio is the ratio of the breadths of each vortex at the instant that they pass through one another. For this exact ratio, the leap frogging occurs once and two vortices of the same breadth remain. For values less than this, periodic motion of the leap frog phenomenon occurs. However, when the ratio is greater than this value, the smaller vortex ring moves through the larger one and widens while the larger one contracts and falls behind. In Figure 2.11 the phenomena is shown between a primary vortex ring and a second vortex ring in shock-induced flow from a pipe end. The primary vortex ring is pushed through the second vortex ring and in the process the second vortex ring leap frogs over the primary vortex ring.

2.6.3 Shock-shear layer interaction

It was observed by Jiang et al.[6] that when a shock wave interacts with a shear layer this part of the shear layer is separated from that grows longer again from the sharp corner of the shock tube. The reason is that after the shock wave sweeps over the shear layer, the radial particle velocity behind the shock wave is increased. Therefore, this part of the shear layer is moved into the jet flow that carries it faster downstream. This results in shear layer splitting and has nothing to do with viscosity.

2.6.4 Shock wave focusing

Shock waves can focus on a plane in a two-dimensional case or on the axis of symmetry for an axisymmetric case. For the axisymmetric case, the focusing will induce accumulation of more energy and lead to generation of a stronger jet [6]. The shock focusing in an axisymmetric case is shown schematically in Figure 2.12. The high pressure generated at the focal point can induce flow features which can otherwise be absent in shock wave focusing in a two-dimensional planar flow.



Figure 2.11: Vortex ring leap frogging[11].

2.7 Compressible flow through a ruptured pipe - Work by Skews et al.

The only study on shock-induced flow through a pipe gap the author is aware of was the one done by Skews et al.[12]. A preliminary study, over a limited range, was done numerically and

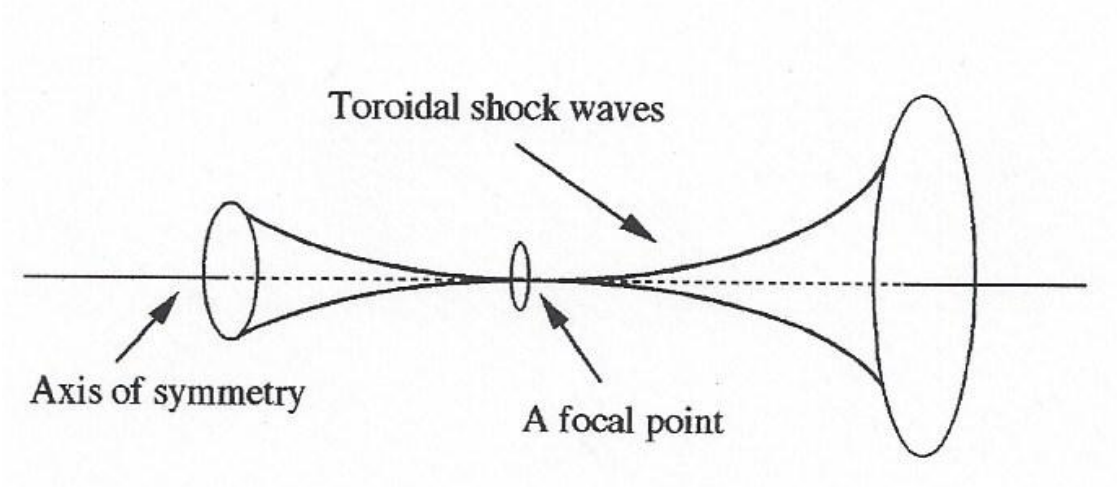


Figure 2.12: Schematic of shock wave focusing for a two-dimensional axisymmetric flow.

experimentally for a shock wave propagating past a gap in a pipeline. The study discussed the resulting gas dynamic phenomena primarily those at the position of pipe separation, with the passage of the shock wave. They were two noticeable effects from the study and these will be briefly described.

2.7.1 Stationary normal shock

Although the flow behind the incident shock was subsonic, the outflow in the pipe gap produced a supersonic jet. This resulted in a stationary standing shock forming at the inlet to the downstream pipe. As steady state was approached, there was oscillation in the position of the standing shock as well as flow emerging from the upstream pipe. The developed standing normal shock is shown for a pipe gap of 20 and 30mm respectively in Figure 2.13.

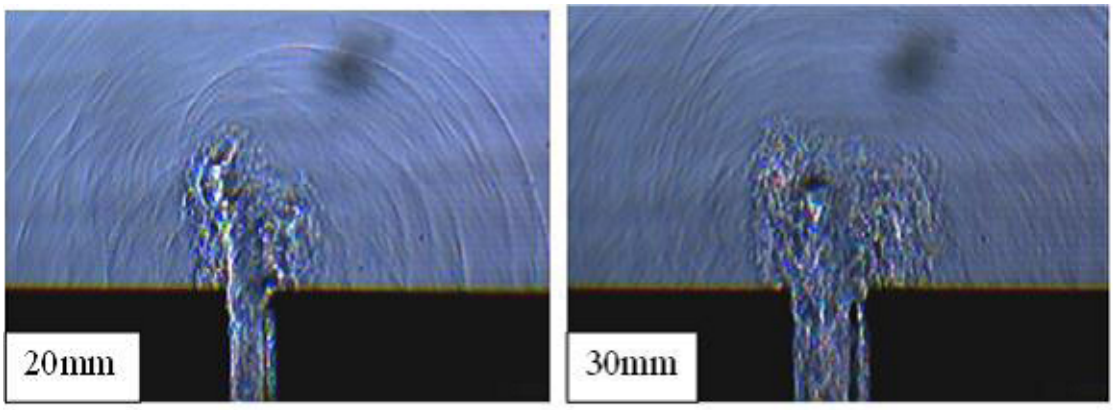


Figure 2.13: Developed standing shock at downstream pipe inlet for a 20mm and 30mm pipe gap.[12]

2.7.2 Flow in the upstream and downstream pipe

Numerical simulations showed that the stationery standing shock essentially controlled propagating conditions of the incident shock wave in the downstream pipe, although as it propagated its strength was significantly diminished from its original value. The flow in the downstream pipe is initially unsteady but then becomes more uniform, controlled by the developed standing shock. The simulations also showed that a strong expansion wave propagates back in the upstream pipe causing a significant drop in pressure in the initial post-shock flow. The upstream flow also tends to steady state with time. Figure 2.14 shows CFD pressure plots of the development of the upstream and downstream pipe to steady state.

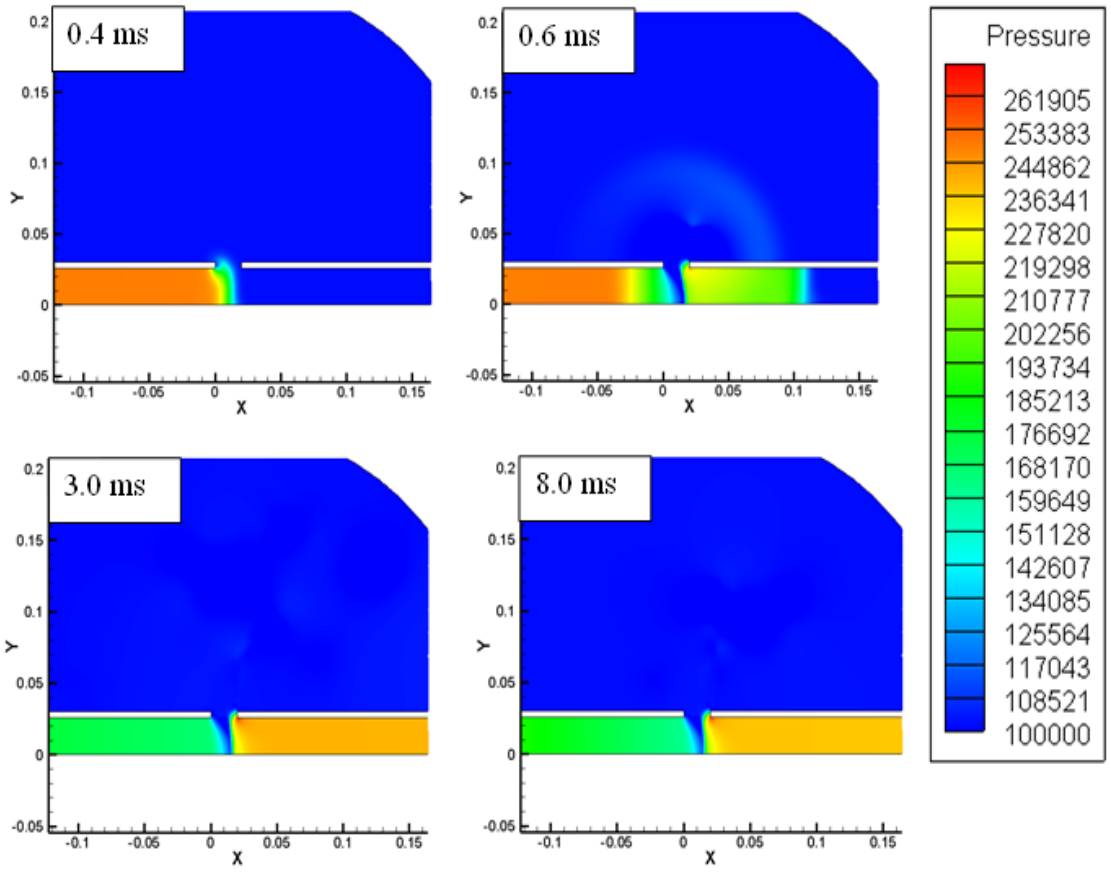


Figure 2.14: Pressure contours for the flow development to steady state in the upstream and downstream pipe.[12]

2.7.3 Vortex ring leap frogging

As the incident shock wave diffracted around the upstream pipe a vortex ring followed.The flow path of the vortex ring was influenced by the velocity field produced after the shock wave propagated through the gap. The vortex ring moves outward into the external flow

field which has been generated by the outward propagating toroidal shock wave resulting from the initial high pressure behind the incident shock. Upon diffraction of the shock wave at the downstream pipe, a second vortex ring was generated. This second vortex interacts with the first one, eventually leapfrogging over it.

2.8 Shock-boundary layer interaction under the influence of a normal suction slot - Work by Weiss and Olivier

In their work, A.Weiss and H.Olivier[15] derived a flow model which explains the transition of a shock train into a single shock under the influence of boundary layer suction slot for a supersonic intake. The geometry of the suction system was a circumferential suction slot similar to a gap in a pipeline. The suction slot was found to be sufficient to stabilize the primary shock of a shock train in as much as the back pressure of the shock train was increased until the shock train gradually changes into a single normal shock.

Their work originated from the study of a flow phenomenon called a 'shock train'. If a supersonic flow passes through a duct of certain length and a back pressure is applied, a shock wave forms. Under certain conditions successive shocks appear downstream of the first shock. This series of shocks is called a shock train.

In their study on the influence of the suction slot onto the position and length of the shock train, wall pressure measurements were done upstream and downstream of the suction slot. With an increasing back pressure, the measurements showed the gradual change of a shock train to a single normal shock. The normal shock was found to stabilise at the slot position and there is a static pressure jump at the slot position.

2.9 Propagation and distortion of pressure waves in a pipeline

When a shock wave propagates and discharges at the pipe end or a pipe gap of a shock tube, wave interactions result in the pipes as was noted in section 1.1. This replicates wave motions in compressible flows in practical industrial pipe systems like the present study. A review is given below for previous studies which focused on wave propagation and distortion in pipes.

2.9.1 Effect of a flange gap on Shock tube performance - Work by A R Butcher

The experimental investigation by A.R Butcher[2] focused on the effects of different sized flange gaps on shock tube performance. Pressure profiles upstream and downstream of the gap were used for the wave propagation in the shock tube. An expansion wave propagated in the upstream pipe reducing the upstream pressure more than the downstream pressure. In the downstream pipe, the shock wave propagated with a reduced strength as compared to the case without a flange gap. Without flow visualisation and numerical simulations, Butcher could not explain the observed pressure profiles. Therefore the observed pressure profiles could not explain the wave propagation and interaction in the two pipes. An exact correlation of gap configuration and shock tube performance was not achieved.

2.9.2 Propagation conditions and wave distortion - Work by Kim et al.

Kim et al.[7] experimentally and numerically addressed the distortion of the compression wave reflected from an open end of a shock tube. The generation and development mechanisms of the compression wave, which was reflected from the open end of the shock tube, were obtained in detail. The effect of the configuration of the pipe end was found negligible. It was found out that the distance necessary for the reflected compression wave to transit to a shock wave does not depend on the magnitude of the incident expansion as well as its wavelength.

2.10 Conclusion

To conclude, as the literature review shows previous work has focused on flow fields at an open-ended shock tube. Shock-induced through a pipe gap has not been fully investigated.

3 Objectives

The objectives of the current study are;

1. A numerical and experimental investigation of the resulting flow features and their interactions within the gap in a pipeline after a simulated explosive event. Variation of boundary conditions to include gap geometry, gap width and shock Mach number. From this, the influence of the individual boundary conditions on the flow development is to be ascertained.

2. Determination of the propagation conditions in the upstream and downstream pipe after passage of the shock wave through the gap. An influence, if any of the gap flow features on the propagation conditions in both the upstream and downstream pipe.

4 Apparatus

4.1 Introduction

The experimental apparatus that has been used in the work described in this report consists of the following components

1. Shock tube (including piping, compressed air supply ports, pressure measurement ports and pipe supports.)
2. Compressed air supply (consisting of the supply lines and its regulation).
3. Instrumentation and Shadowgraphy system.

4.2 Shock tube

A fabricated shock tube was used for the experimental investigation. Honed piping was used with a 50mm internal diameter and 62mm outer diameter. The wall thickness of 6mm was determined to be adequate to withstand the high pressures involved in the typical high shock Mach numbers used. The honed pipe was cut at specified lengths for easier machining of the pressure measurement ports as well as for structural strength. The different pipe sections were joined together by bolted flanged joints. Flanges were laser cut to be welded onto the ends of the tubing. These flanges were designed according to the South African National Standard (SANS 1123). At these cuts, the flanges were welded on using the Tungsten Inert Gas (TIG) welding technique. The flanged joint separating the driver and driven section had a rubber gasket for effective sealing during pressurisation.

For the testing of the two different gap geometries, different piping arrangements were used for the flanged and pipe gap geometry. The two arrangements are shown below schematically in Figure 4.1 and Figure 4.2. The relative positions of the pressure measurement points are

numbered. The points for pressurisation and pressure monitoring in the driver are shown by P and M respectively. Table B.1 shows the positions of the pressure measurement points relative to the gap.

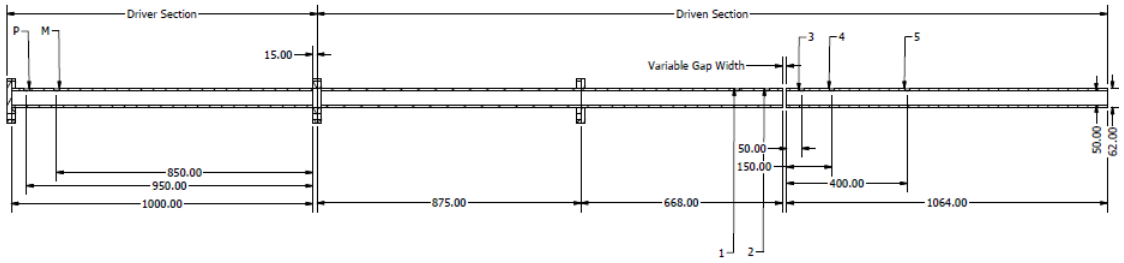


Figure 4.1: Schematic for the piping arrangement for the pipe gap geometry.

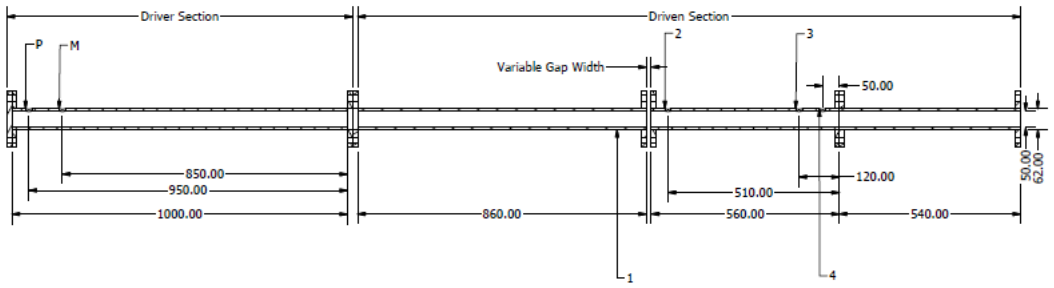


Figure 4.2: Schematic for the piping arrangement for the flanged gap geometry.

Table 4.1: Relative positions for the pressure transducers

Gap geometry	**Station number**	**Relative position**
Pipe gap	1	675mm upstream
	2	150mm upstream
	3	50mm downstream
	4	150mm downstream
	5	400mm downstream
Flange gap	1	50mm upstream
	2	50mm downstream
	3	440mm downstream
	4	510mm downstream

In isometric view, the pipe gap and the flange gap arrangements are shown in Figure 4.3 and Figure 4.4.

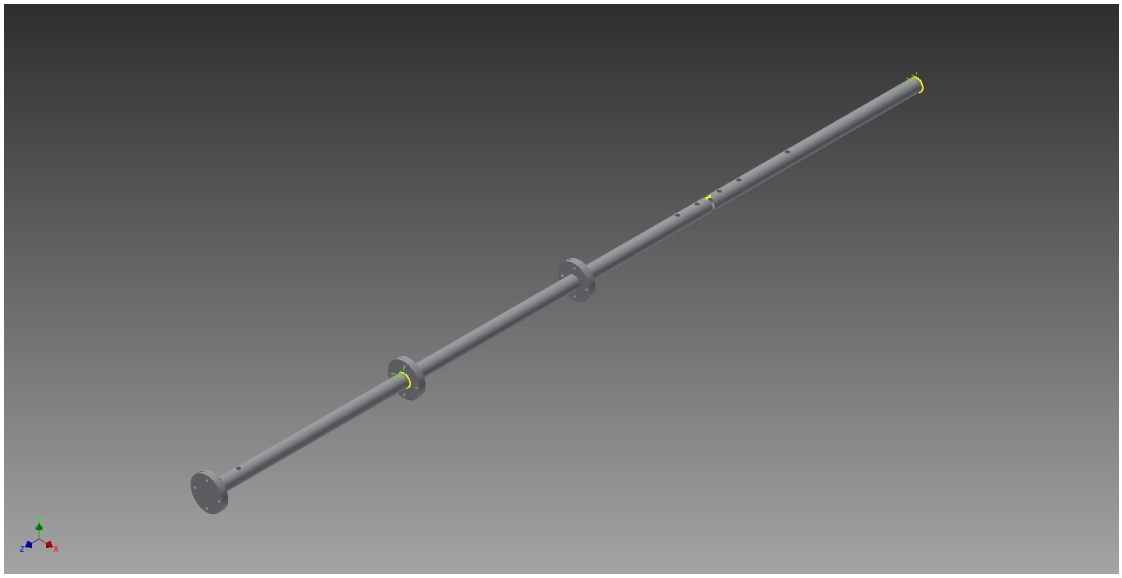


Figure 4.3: Isometric view for the pipe arrangement for the pipe gap.

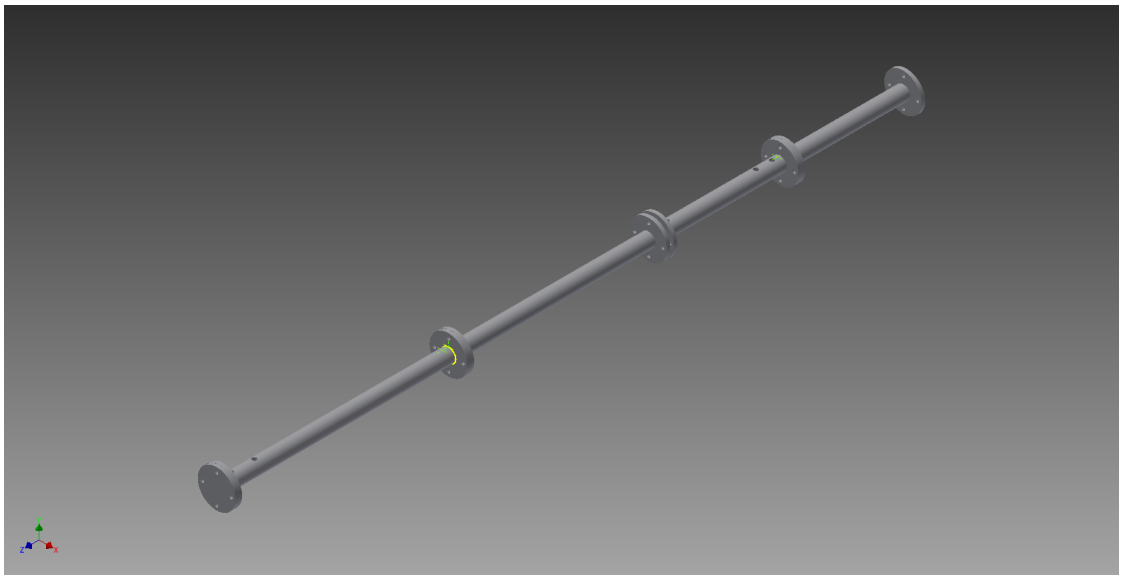


Figure 4.4: Isometric view for the pipe arrangement for the flange gap.

The length of the tube from the diaphragm to the open end for the upstream pipes was chosen to be at least 30 times the tube diameter. This was done to ensure a fully formed planar shock wave was readily obtained at the open end. The driver section was made to be 1000mm in length. This would ensure the reflected expansion waves from the driver wall would not affect the development of the gap flow. From an initial Computational Fluid Dynamics (CFD) simulation, the length of downstream piping section for the flanged and pipe gap geometry were determined to be 1064mm and 1100mm respectively. These lengths ensured no wave reflections from the end of the downstream pipes affected the development of the gap features within the testing time.

The driver and pressure measurement ports were made using 19mm round bar and then machined precisely by the Mechanical Engineering Laboratory at the University of the Witwatersrand. The pressure transducers were installed in such a way there were flush with the inner wall. An initial CFD simulation was done to determine the relevant positions along the shock tube for pressure measurement ports. A drawing of the pressure port is shown below in Appendix F.

For flow visualisation of the test section, the shock tube assembly had to be lifted to a height suitable for the optics. For this the shock tube was supported by piping supports. The piping supports would also allow the adjustment of the gap width for the various testing conditions. The pipe support is now shown in isometric view in Figure 4.5.

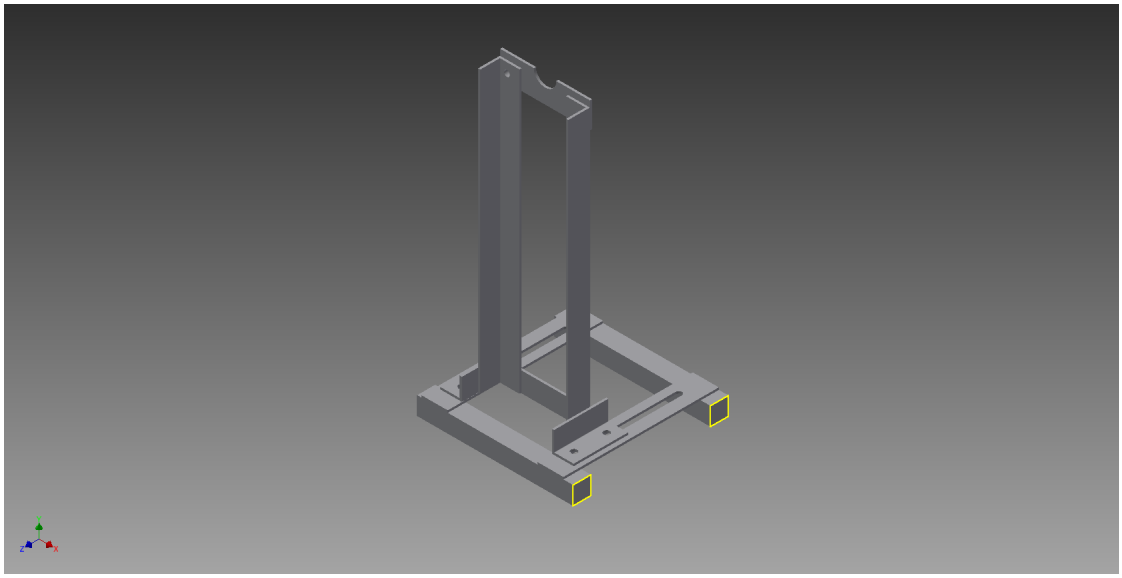


Figure 4.5: Shock tube supports.

4.3 Compressed Air Supply

To be able to produce the range of Mach numbers necessary for experimental investigation, a compressed air cylinder was used to deliver the compressed air. For regulation of the driver pressure, a pressure regulating valve was fitted at the outlet of the cylinder. The regulating valve had a range of 0 to 16 bar. Once regulated to the required driver pressure, the compressed air is filled to the shock tube driver through the control board. The control board consists of valves and gauges that control the filling rate and monitoring of driver pressure. The compressed air cylinder and the control board are now shown in Figure 4.6 and Figure 4.7.



Figure 4.6: Air cylinder with pressure regulator valve

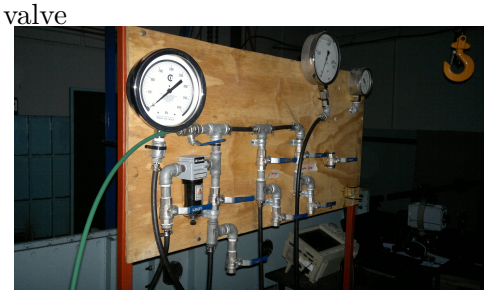


Figure 4.7: Controlboard for pressure regulation

Quarter inch British Standard Pipe (BSP) adapters were used to attach 6mm internal diameter pressure hose to the driver section. The maximum pressure that could be experienced by the hose is 1500 kPa while the hose was rated at 2000 kPa.

4.4 Instrumentation

For the experimental data acquisition, various instruments were used for the measurement,monitoring and control of different variables. These instruments are best shown in Figure 4.8 by a schematic diagram. The schematic shows how the instruments were connected and interacted with each other.

The compressed air supply pressure to the driver was controlled through the regulating valve and the control board. The control board also had a pressure gauge for monitoring driver pressure. Flush-mounted PCB pressure transducers measured the shock tube pressure transients at specified locations after diaphragm rupture. The voltage signal from the pressure transducers was conditioned and amplified by the signal conditioners and were input to the Hantek oscilloscope. The pressure readings are displayed on a laptop as voltage through the oscilloscope software. The oscilloscope software also enabled the pressure data to be saved in different formats for later post-processing.

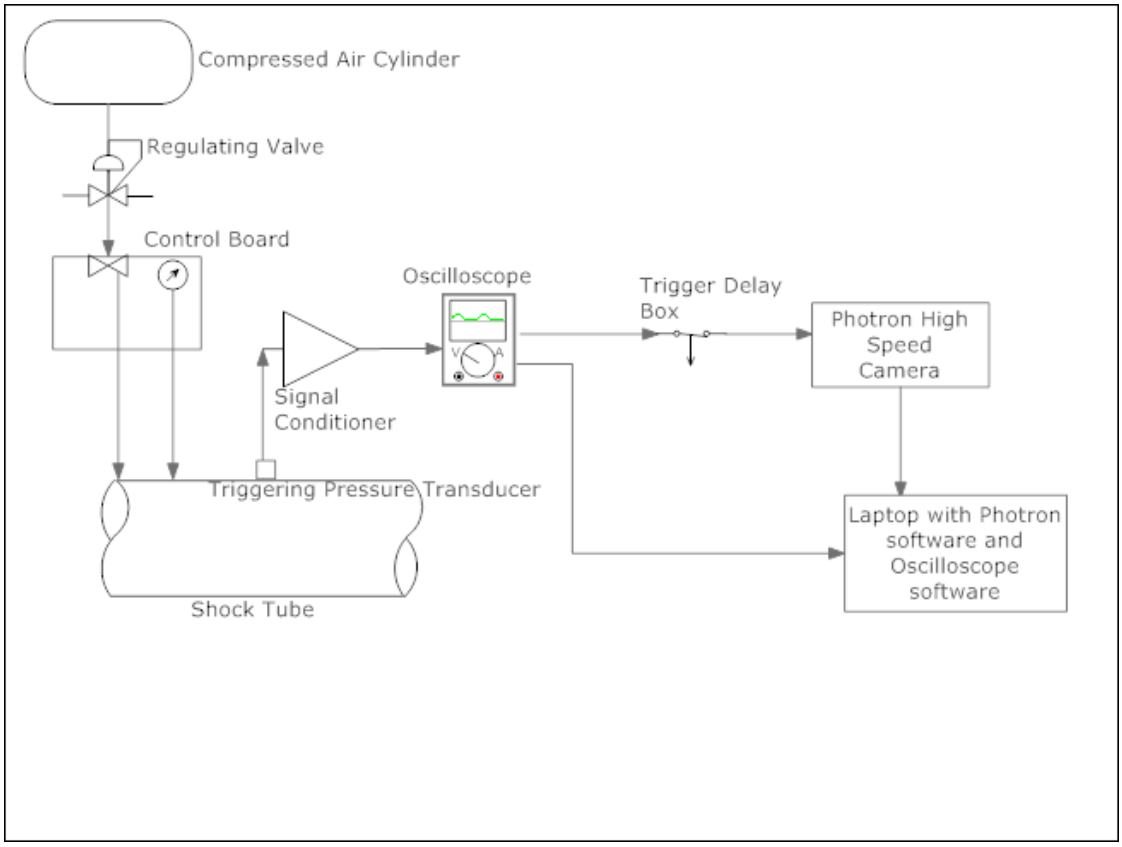


Figure 4.8: Instrumentation components.

For flow visualisation the signal from the oscilloscope is fed to the programmable electro-delay trigger box. After the set delay time the trigger delay box sends a triggering signal to the high speed camera to start capturing. For the present study, capturing started at the time the incident shock wave exited the upstream pipe. The images and videos are viewed and processed by the Photron software on a laptop.

Specifications for the pressure transducers, oscilloscope and the high speed camera are given in Appendix B.

4.5 Shadowgraphy optical system

For experimental flow visualisation of the flow discontinuities, a conventional Z-format shadowgraphy system was used with high-speed imaging using a Photron camera. The schematic of the optical set-up is shown in Figure 4.9. The only difference for the shadowgraphy was the ommission of the cut-off at the camera side. Each rail is directed towards a parabolic front-silvered mirror with f-number of $f/4.5$ and 16 inch diameter. All the vertical and horizontal cut-offs are made from stainless-steel Lion razer blades. All optical rails, lenses and

parabolic mirrors were accurately leveled and aligned using a digital inclinometer and a rail-mounted cross-hair laser. The full specifications for the Megaray high density light source, Photron high speed camera are shown in Appendix B. Full instructions on how the rails and lenses were correctly set-up, the file *Guide to Setup-Schliren Optical System.pdf* located in Appendix A describes the set-up procedure.

Two different light sources were used for the Photron high-speed camera. A Megaray high density light source and a Canon Speedlite flash were used. The Canon Speedlite flash had a pulse duration of about 20ms whilst the Megaray high density light source was a continuous light source.

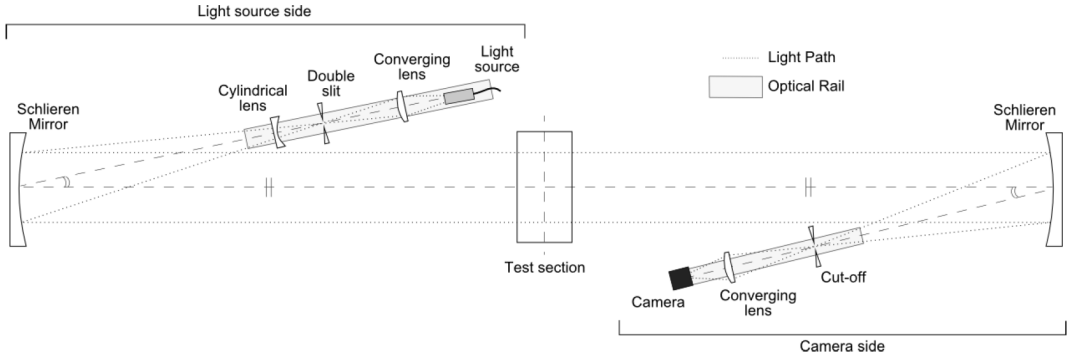


Figure 4.9: Monochrome schlieren optical system setup

4.6 Diaphragms

The material used for the diaphragms was polyester sheet. There were four different thicknesses available namely, 25, 50, 100 and 190 microns. The diaphragms were cut into squares of approximately 120mm sides by use of a cardboard template. The square shape used ensured effective clamping area of the diaphragms between the flanged coupling. An effective clamping area ensured the diaphragms were secured adequately and there was effective sealing for the driver during pressurisation. In order for the burst of a diaphragm to be an even burst, the diaphragm should be mechanically burst within about 2% of the natural burst pressure.

5 Methodology

5.1 Introduction

For the present study, the research tools which were used were experimental testing and numerical simulations. Both gas dynamic simulation sciences have their advantages and disadvantages, but both used together can be effective. Numerical simulations in the form of CFD will complement experimental testing. This will entail testing experimentally at the critical and important boundary conditions, and use validated CFD to cover extended boundary conditions. This will mean 'smart' experimental testing where repetitive testing is avoided.

5.2 Numerical simulations

As has been outlined in the section 5.1, CFD will complement experimental testing in covering extended boundary conditions. In the current study, simulations for high Mach number flows and complex pipe geometries which are difficult to do experimentally will be covered with CFD. In addition, CFD will enhance the ability to highlight physics in fluid flows that are too complicated to be clearly visualised experimentally. The initial design stages of the experimental facility were also done by CFD. This included the position of pressure measurement points along the shock tube and piping lengths for the different sections of the shock tube.

5.2.1 Governing equations

In order to interpret experimental shadowgraphs and produce a flow field without effects of three dimensionality, the axisymmetric Euler equations were solved by using a commercially available code Fluent 15 ©. The coupled solver in Fluent 15 solves the governing equations of

continuity, momentum and energy simultaneously as a set, or vector, of equations. Governing equations for additional scalars will be solved sequentially (i.e., segregated from one another and from the coupled set). The system of governing Euler equations for conservation laws for a perfect gas in integral, Cartesian form for an arbitrary control volume V with differential surface area dA are given in equation (5.1).

$$\frac{\partial}{\partial t}\int_V \mathbf{W}dV + \oint \mathbf{F}dA = \int_V \mathbf{H}dV \tag{5.1}$$

where the vectors W and F are defined as

$$\mathbf{W} = \begin{pmatrix} \rho \\ \rho u \\ \rho v \\ \rho E \end{pmatrix} \qquad \mathbf{F} = \begin{pmatrix} \rho\mathbf{v} \\ \rho\mathbf{v}u + p\hat{\mathbf{i}} \\ \rho\mathbf{v}v + p\hat{\mathbf{j}} \\ \rho v E + p\mathbf{v} \end{pmatrix}$$

and the vector H contains source terms such as body forces and energy sources. Here ρ, v, E, and p are the density, velocity, total energy per unit mass, and pressure of the fluid, respectively.

The equation of state for the perfect gas is given by equation (5.2)

$$E = \frac{p}{\gamma - 1} + \frac{1}{2}\rho(u^2 + v^2) \tag{5.2}$$

where γ, the specific heat ratio in air, is taken as 1.4.

For the numerical implementation of inlet boundary conditions within Fluent, one dimensional shock equations for a moving shock were made use of. The inlet boundary is modelled as a pressure inlet boundary. For the pressure inlet boundary condition, Fluent requires the stagnation conditions and static pressure behind the moving shock wave.

For the analysis and solution of the moving shock equations, the relations used for a stationery normal shock can also be used for a moving shock. The reference frame for the moving shock wave was converted from a moving reference frame to a stationery reference frame. The two frames of reference are illustrated below in Figure 5.1.

The stationery reference frame entails superimposing a reference velocity on the observer so that the moving shock appears stationery to the observer. The static properties of pressure, temperature and density refer to the thermodynamic state of the gas and are independent

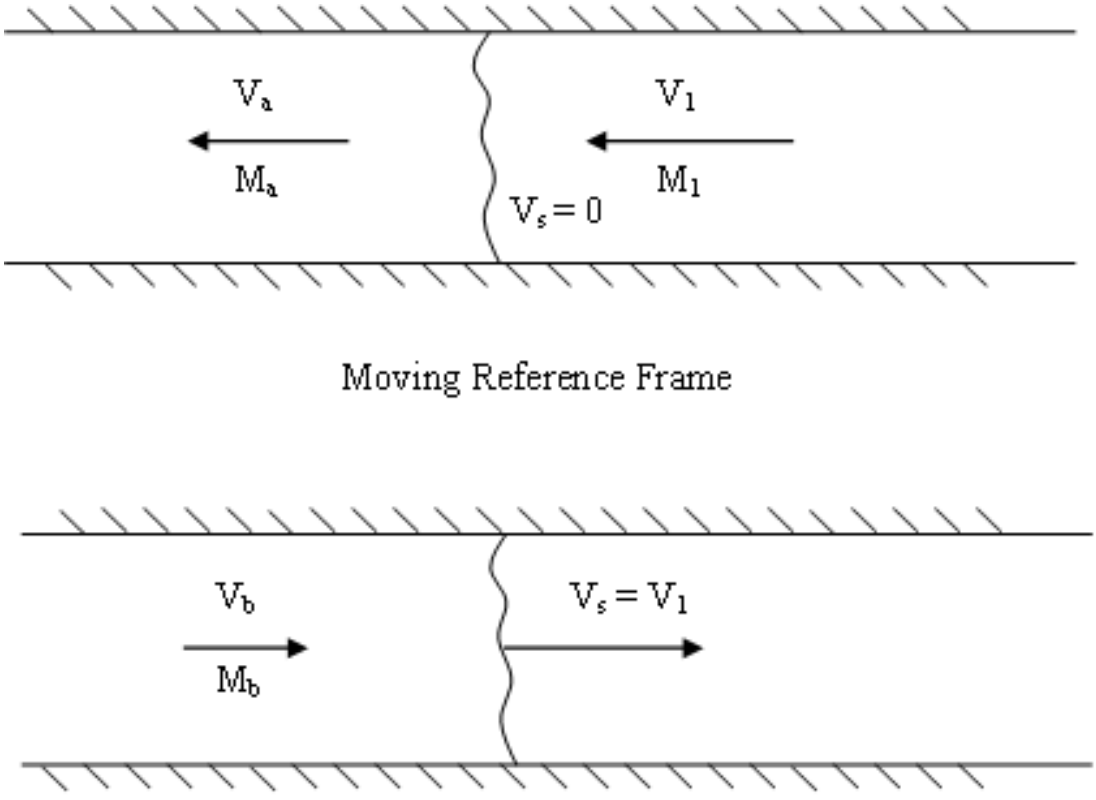


Figure 5.1: Moving and stationery reference frames for unsteady shock wave motion.

of the reference frame from which they are measured. However the stagnation properties depend on the velocity of the reference frame.

Therefore to calculate the static pressure P_a and the static temperature T_a behind the moving shock, the stationery normal shock equations are used with the moving reference frame. From the stationery normal shock relations, the downstream Mach number can be determined from the upstream Mach number. The equation relating the upstream Mach number M_1 and downstream Mach number M_a is given by equation(5.3).

$$M_a^2 = \frac{\frac{2}{\gamma-1} + M_1^2}{M_1^2 \frac{2\gamma}{\gamma-1} - 1} \tag{5.3}$$

With the downstream Mach number M_a, the quantities P_a and T_a can now be calculated from equation (5.4) and equation (5.5)

$$P_a = P_1 \frac{(1 + \gamma M_1^2)}{(1 + \gamma M_2^2)} \tag{5.4}$$

$$T_a = T_1 \frac{(1 + M_1^2 \frac{\gamma - 1}{2})}{(1 + M_2^2 \frac{\gamma - 1}{2})} \tag{5.5}$$

The value of P_a is the input to the supersonic initial gauge pressure in Fluent for the pressure inlet boundary.

To calculate the stagnation conditions behind the moving shock, the stationery reference frame is used to solve the normal shock equations. First, the velocity behind the shock, V_b, is calculated by subtracting V_a from V_1 in the moving reference frame, as this is the velocity an observer moving with the shock sees behind the moving shock. This value is then used to calculate the Mach number behind the shock, M_b. The static conditions P_b and T_b are the same as P_a and T_a as they do not depend on the reference frame. Since the air in front of the shock is stagnant, P_1 is the same as P_{01} and T_1 is the same as T_{01}. The stagnation temperature behind the shock wave, T_{0b}, and stagnation pressure, P_{0b}, are calculated using equation (5.6) and equation (5.7) respectively.

$$T_{ob} = T_b(1 + M_b^2 \frac{\gamma - 1}{2}) \tag{5.6}$$

$$P_{ob} = P_b(1 + M_b^2 \frac{\gamma - 1}{2})^{\frac{\gamma}{\gamma - 1}} \tag{5.7}$$

These two values are the total temperature and total gauge pressure inputs for the pressure inlet boundary condition in Fluent respectively.

5.2.2 Computational domain

The geometry was modelled as a native CAD geometry and imported as a STEP file to Ansys©. The geometry was modelled as axisymmetric with a hemisphere to account for the external flow field. The length of the downstream section of the computational domain of 1064mm, was chosen after performing an initial simulation. It was found that the expansion at the end of the tube propagated back down the tube, thus affecting the flow development within the gap. Therefore, a long enough tube length after the pipe gap was required to ensure that the expansion from the end did not affect the results. Pre-processing of the geometry for numerical simulations preparation was done in Ansys Geometry©. Pre-processing

also included naming of the boundaries of the computational domain for later implementation in the flow solver. Figure 5.2 shows the computational domain for the pipe gap. The corresponding boundary conditions for a pipe at Mach 1.6 and their respective locations are shown in Table 5.1. The geometric locations are in reference to Figure 5.2.

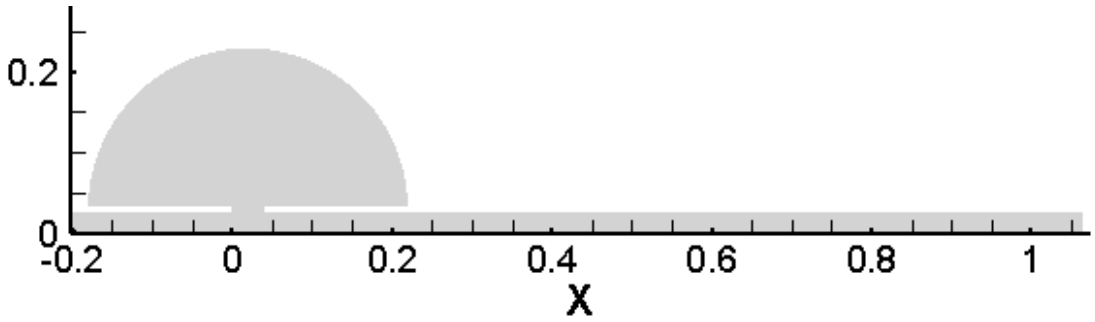


Figure 5.2: Computational domain.

Table 5.1: Boundary conditions for Mach 1.60

Boundary type	**Location**	**Pressure**		**Temperature**	
		Static(Pa)	**Total(Pa)**	**Static(K)**	**Total(K)**
Pressure inlet	Right boundary	285 736.5	392 725.7	300	456
Axis	Lower boundary	N/A	N/A	N/A	N/A
Pressure outlet	Left boundary	101 325	N/A	300	N/A
Wall	Boundaries of tube	N/A	N/A	N/A	N/A
Pressure far-field	Hemisphere edge	101 325	N/A	300	N/A

The operating condition was specified as zero Pascals so that the system was working in absolute pressure.

5.2.3 Meshing

After preprocessing of the geometry, meshing could now be done on the computational domain. Initial meshing was done with Ansys meshing ©. An unstructured mesh was applied composed of quad-dominant cells for two-dimensional simulations. For the three-dimensional mesh an unstructured mesh was used with tetrahedral cells with a triangle surface mesher.

Different local meshing techniques were used for the initial meshes. Refinement of the region near the wall was done by the inflation method. Refinement of the wall was done to capture the reflection of the incident shock at the exterior and interior walls of the downstream pipe. A sphere of influence was also used to refine the flow features within the gap. A typical initial mesh with a sphere of influence is shown in Figure 5.3 for the burst pipe simulation. The specifications for the initial mesh and local meshing technique are shown in Table 5.2. The

initial mesh was deemed fine enough from a grid dependence study to capture the necessary flow features.

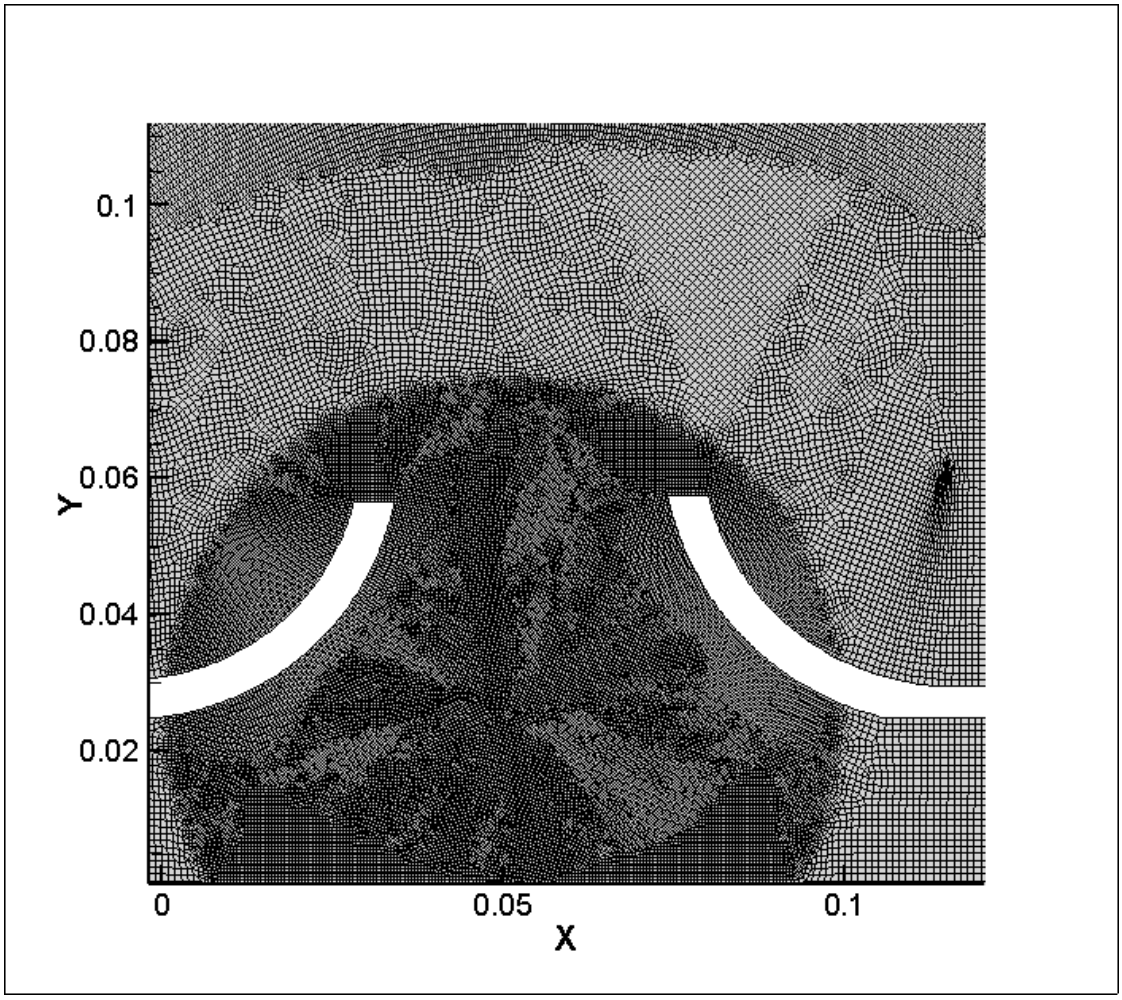


Figure 5.3: Initial mesh for a burst pipe simulation showing the sphere of influence.

Table 5.2: Specifications for initial mesh

Specification	**Value**
Physics preference	CFD
Solver preference	Fluent
Advanced sizing function	Off
Relevance centre	Fine
Element size	1.0mm
Sphere of influence element size	0.5mm
Sphere of influence radius	50mm
Number of nodes	134000
Number of elements	138967

5.2.4 Flow Solver Specifications

The density-based solver was used with a transient formulation to simulate the moving shock waves. An absolute velocity formulation was chosen for a two-dimensional axisymmetric model.

5.2.4.1 Models and Materials

Simulations were done with the inviscid Euler model as well as the energy equation. The inviscid model was deemed to be sufficient for the concerned flow physics as well as the time scales under consideration. The fluid was modelled as air as an ideal gas.

5.2.4.2 Initial conditions

In addition to the boundary conditions specified in Table 5.1 the simulations were initialised using standard initialisation. An absolute formulation was chosen. The fluid interior was initialised with a pressure of 101 325K and a temperature of 300K.

5.2.4.3 Solution Methods

An implicit solver was used for solving. Spacial discretisation was done using the third order MUSCL scheme. The use of the third-order MUSCL scheme ensured a conservative and dissipative scheme. The flow discontinuities like shock waves could be resolved without any numerical oscillations. The third-order scheme also ensured the strength of the vortical structures was conserved even at later time steps once shed at the edges of the pipe gap. Temporal discretisation was done with the second order implicit method.

5.2.4.4 Solution Controls

Linear stability theory determined a range of permissible values for the Courant number(i.e., the range of values for which a given numerical scheme will remain stable). A Courant number of 1 was specified as a permissible value for the coupled implicit solver used for the present simulations.

During the solution process convergence was monitored dynamically by checking residuals of solution variables. Table 5.3 gives the convergence criteria for the different solution variables

residuals. The print reports for the residuals of the solution variables were displayed during the simulations. Elapsed time was also monitored during the simulation.

Table 5.3: Convergence criteria for different solution variables residuals

Solution variable residual	**Convergence criteria**
Continuity	0.0001
x-velocity	0.0001
y-velocity	0.001
Energy	0.00001

5.2.4.5 Adaptive mesh refinement

For optimum resolution of the flow discontinuities with the present third-order MUSCL scheme, adaptive local mesh refinement within Fluent was essential in the region of the flow discontinuities. The refinement has the capability of tracking and resolving travelling shock waves. The refinement aims to capture and refine shock fronts and its reflected components, shear layers and vortices. By using this method, the computational overhead is kept to a minimum. This was done via a set of user defined commands in the calculation activities tab. The parameter which was used to mark cells for refinement and coarsening of the mesh was the gradient for velocity and density. The two cell registers are then combined. The parameters for adaptive mesh refinement are summarised in Table 5.4. Figure 5.4 show the refined meshes at different time steps for a burst pipe simulation and shows how the shock fronts are tracked and refined. The adaptive mesh refinement method is shown to accurately track the shock fronts and its associated reflections during the simulation.

Table 5.4: Adaptive mesh refinement parameters

Adaptation parameter	**Value**
Gradient adaptation options	Refine/Coarsen
Adaptation method	Curvature
Curvatures of	Density and Velocity
Normalisation	Scale
Thresholds	Refine = 0.2
	Coarsen = 0.4
Maximum level of refinement	5

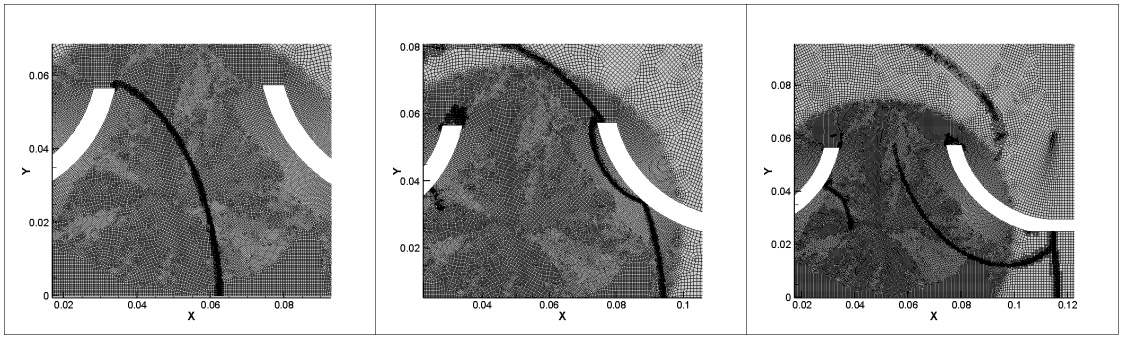


Figure 5.4: Tracking of refinement of the shock front and its reflection at different time steps. Images at 0.20ms apart.

5.2.4.6 Time step size

A time step size of 0.0000017s was chosen. This was small enough for the time scales for the present flow field. The time step was also comparable to duration of a single frame in the experimental high-speed imaging. This would allow the comparison of numerical and experimental results at similar flow times. The time frame for the full development of the gap flow was determined to be about 3ms, therefore the number of time steps was set to 1800.

5.3 Experiments

Experimental investigation was done for different geometries, gap widths and shock Mach numbers which could be modelled experimentally. Experimental testing was carried for the pipe and flanged gap geometries. The boundary conditions for the experimental tests are summarised in Table 5.5.

The experiments carried out can be broadly categorised into three sections

- Diaphragm calibration.
- Pipe gap geometry flow visualisation.
- Flanged gap geometry flow visualisation.

The experimental procedures for each test is now described below. For each of the tests, the procedures consist of pre-test actions, performing the test and post-test actions.

Table 5.5: Boundary conditions for experiments

Gap geometry	**Boundary conditions**	
	Gap width	**Shock Mach number**
Pipe gap	40mm	1.60
	40mm	1.56
	50mm	1.60
	50mm	1.56
	60mm	1.60
	60mm	1.56
	60mm	1.45
	60mm	1.30
	70mm	1.60
	70mm	1.56
	70mm	1.45
	80mm	1.60
	80mm	1.45
	80mm	1.30
	100mm	1.60
	100mm	1.56
	115mm	1.60
	115mm	1.45
Flanged	40mm	1.45
	40mm	1.30
	50mm	1.45
	50mm	1.30
	60mm	1.45
	70mm	1.45
	70mm	1.30
	80mm	1.45
	115mm	1.45

5.3.1 Diaphragm Calibration

Diaphragm calibration was the first set of experiments carried out. This enabled the determination of the natural burst pressure for different diaphragm thicknesses. The Mach number of the shock resulting from the natural burst is also determined from the diaphragm calibration tests.

5.3.1.1 Pre-test actions

1. Set up the experimental rig for the pipe gap piping arrangement. Secure the diaphragm of 25nm thickness as specified by Table D.1 in Appendix D. Ensure all the shock tube piping connections are secure.

2. Connect the hose for pressure supply to the control board from the regulating valve of compressed air cylinder. Ensure the cylinder pressure is above the test pressure. Connect the hoses for driver pressurisation and driver pressure monitoring to the appropriate ports at the control board. Connect the two hoses to the corresponding ports on the driver. Ensure all hose connections are secure.

3. Install pressure transducers at station 1 and station 2 for unflanged piping arrangement as designated in chapter 4. Connect the pressure transducer wires to the appropriate ports of the signal conditioner. Turn on the signal conditioner and ensure they are reading the signal from the two pressure transducers(the needle stays in the green region).

4. Connect the connection wires from ports scope 1 and scope 2 on the signal conditioner to channel 1 and channel 2 respectively of the oscilloscope. Connect the usb cable from the oscilloscope to the laptop.

5. Turn on the oscilloscope and launch the oscilloscope software on the laptop.

6. Turn the tab for channel 1 and channel 2 to ON. Set the vertical axis setting to 100mV/div for both channels. Set the horizontal axis setting to 1ms/div for both channels. Set the trigger mode to single and trigger level to 188mV. Set the trigger source to channel 1. Click the tab RUN and the software will display the WAITING message to acknowledge its waiting for a trigger.

5.3.1.2 Performing the test

1. Trigger the warning alarm in the laboratory to alert the test is about to commence.

2. Open the main valve on the compressed air cylinder about one full turn.

   - Precaution: Ensure the regulating valve on the cylinder is at the fully closed position.

3. Turn the knob on the regulating valve until the gauge on the valve reads the required outlet pressure.

   - Precaution: The outlet pressure is set in such a way that the value is slightly above the test pressure.

4. Open the main supply valve at the control board. Blow the warning whistle to alert the laboratory the pressurisation of the driver is about to commence.

    - Precaution: Ensure all the other valves at the control board are in the closed position.
    - Precaution: Ensure ear protection is worn.

5. Vent the driver by opening the vent valve until the driver pressure is at zero bars. Close the vent valve.

6. Open the driver pressurisation valve and start monitoring the driver pressure from the driver pressure gauge.

    - Precaution: Slightly open the driver pressurisation valve to ensure controlled pressurisation of the driver. This will ensure a smooth driver pressure increase and effective pressure monitoring.
    - Precaution: Blow the whistle at each one bar increase in driver pressure.

7. Continue the driver pressurisation until the diaphragm bursts and note the burst pressure. Close the driver supply valve and main supply valve on the cylinder.

8. Vent the supply line by opening the vent valve on the control board whilst the control board main supply is open.

5.3.1.3 Post-test actions

9. Using the measure function on oscilloscope software, determine the time taken by the shock wave to reach the pressure transducer at station 2 after leaving the pressure transducer at station 1. This will be the time between the two peaks for the respective channels. Note this time and the value of the temperature on the thermometer in the laboratory.

10. Repeat steps 1-9 for two more identical tests.

11. Repeat steps 1-10 for the other diaphragm thicknesses as specified in Table D.1 in Appendix D.

5.3.2 Flanged and Pipe Gap Experiments

Having calibrated the different diaphragm thicknesses for the natural burst pressure and the shock Mach number produced, flow visualisation is carried out for different gap width, gap geometry and Mach number.

5.3.2.1 Pre-test actions

1. Set up the experimental rig for the pipe gap piping arrangement with the specific gap width. Secure the appropriate diaphragm thickness depending on the required shock Mach number from Table D.1 in Appendix D. Ensure all the shock tube piping connections are secure.

    - Precaution: Ensure the upstream and downstream pipe are perfectly level and lie in the same plane. To perfectly level the pipes, use a stub pipe of 50mm internal diameter placed inside both pipes at the gap. With the stub pipe inside, bring the two pipes are brought close together. Once level, the downstream pipe is pulled back and the temporary stub pipe is removed.

2. Set up the Z-format shadowgraph apparatus with the high speed camera in place using the set-up procedure in the file *Guide to Setup-Schliren Optical System.pdf* located in Appendix A. Test the sensitivity of the system using a gas heater at the test section. The density gradients should be visible in the test section through the high speed camera as a heated gas has density gradients.

    - Precaution: Once the optics have been set up, disturbance to the alignment of the optical instruments should be avoided.

3. Connect the hose for pressure supply to the control board from the regulating valve of compressed air cylinder. Ensure the cylinder pressure is above the test pressure. Connect the hoses for driver pressurisation and driver pressure monitoring to the appropriate ports at the control board. Connect the two hoses to the corresponding ports on the driver. Ensure all hose connections are secure.

4. Install pressure transducers at station 2,3,4 and 5 for pipe gap piping arrangement as designated in Figure 4.1. Connect the pressure transducer to the appropriate ports of the signal conditioner. Turn on the signal conditioner and ensure they are reading the signal from the four pressure transducers (the needle stays in the green region).

5. Connect the ports scope 1,2,3 and 4 on the signal conditioner to channels 1,2,3 and 4 respectively of the oscilloscope. Connect the oscilloscope to the laptop through the USB cable.

6. Turn on the oscilloscope and launch the oscilloscope software on the laptop.

7. Turn the tab for channel 1,2,3 and 4 to ON. Set the vertical axis setting to 100mV/div for all the channels. Set the horizontal axis setting to 1ms/div for all the channels. Set the trigger mode to single and trigger level to 188mV. Set the trigger source to channel 1. Click the tab RUN and the software will display the WAITING message to acknowledge its waiting for a trigger.

8. Connect the oscilloscpe 'trigger out' port to the input of the trigger delay box designated 'trigger in'. Turn on the trigger delay box and set the delay to $296\mu s$. Connect the 'trigger out' port of the trigger delay box to the 'trig ttl in' port of the high speed camera.

9. Connect the high speed camera to the laptop through the ethernet cable. Turn on the camera and the light source.

10. Launch the camera software on the laptop. Set the frame rate to 75 000 frames per second and the shutter speed to 1/1000000 seconds.

11. Perform the camera shading calibration by blocking light entering the camera and clicking the shading and calibrate tab.

12. Click record.

13. Arm the trigger delay box

5.3.2.2 Performing Test

14. Trigger the warning alarm in the laboratory to alert the test is about to commence.

15. Open the main valve on the compressed air cylinder about one full turn.

    - Precaution: Ensure the regulating valve on the cylinder is at the fully closed position before opening the main compressed air cylinder valve.

16. Turn the knob on the regulating valve until the gauge on the valve reads the required outlet pressure.

    - Precaution: The outlet pressure is set in such a way that the value is slightly above the test pressure.

17. Open the main supply valve at the control board. Blow the warning whistle to alert the laboratory the pressurisation of the driver is about to commence.

    - Precaution: Ensure all the other valves at the control board are in the closed position.
    - Precaution: Ensure ear protection is worn.

18. Vent the driver by opening the vent valve until the driver pressure is at zero bars. Close the vent valve.

19. Open the driver pressurisation valve and start monitoring the driver pressure from the driver pressure gauge as the driver pressurises.

- Precaution: Slightly open the driver pressurisation valve to ensure controlled pressurisation of the driver. This will ensure a smooth driver pressure increase and effective pressure monitoring.
- Precaution: Blow the whistle at each one bar increase in driver pressure.

20. Continue the driver pressurisation until the diaphragm bursts. Close the driver supply valve and main supply valve on the cylinder.

21. Vent the supply line by opening the vent valve on the control board whilst the control board main is open.

5.3.2.3 Post-test actions

1. Save the recorded flow visualisation data in the desired formats. Turn off the camera to avoid it overheating.

2. Save the pressure time profiles from the four channels through the save tab on the oscilloscope software.

3. Repeat steps 1-21 in subsubsection 5.3.2.2 and steps 1-2 in subsubsection 5.3.2.3 for a different set of boundary conditions in terms of gap width and Mach number.

4. Set up the alternate piping arrangement for the flanged gap geometry. For the flanged gap geometry the pressure transducer is placed at station 1 as designated in Figure 4.2. Set trigger delay to $88\mu s$.

5. Repeat steps 1-21 in subsubsection 5.3.2.2 and steps 1-3 with with only one channel of pressure measurement active.

6 Data Processing

6.1 Introduction

General observations and subsequent data processing will be covered in this chapter.

6.2 General Observations

General observations will present the primary, unprocessed data from the experimental investigations.

6.2.1 Diaphragm Calibration

Before the actual experimental data could be collected, diaphragm calibration had to be carried out. The calibration determined the natural burst pressure and shock strength for different diaphragm thicknesses. The thicknesses used were 25, 50, 75 and 100 micrometers. For the 50, 75 and 100 micrometer thickness, multiple layers of diaphragms were used. A testing log was kept as the diaphragms were burst naturally. The natural burst pressure was logged for each test done. Three tests were performed for each diaphragm thickness.

To summarise the observations, consistency of the natural burst for each diaphragm thickness was checked over the three tests. Figure 6.1 shows the observed natural burst pressures for the various diaphragm thicknesses.

The effect of the number of layers of diaphragms for a given thickness was analysed as well. From Figure 6.1 it was observed that for a given thickness, the more the number of diaphragms the higher the natural burst pressure. This is the best shown for the 50 micrometres thickness. In one test two diaphragms of 25 micrometres each had a burst pressure of 5 on average. In the other test, one diaphragm of 50 micrometers had a burst pressure of 4.2 on average.

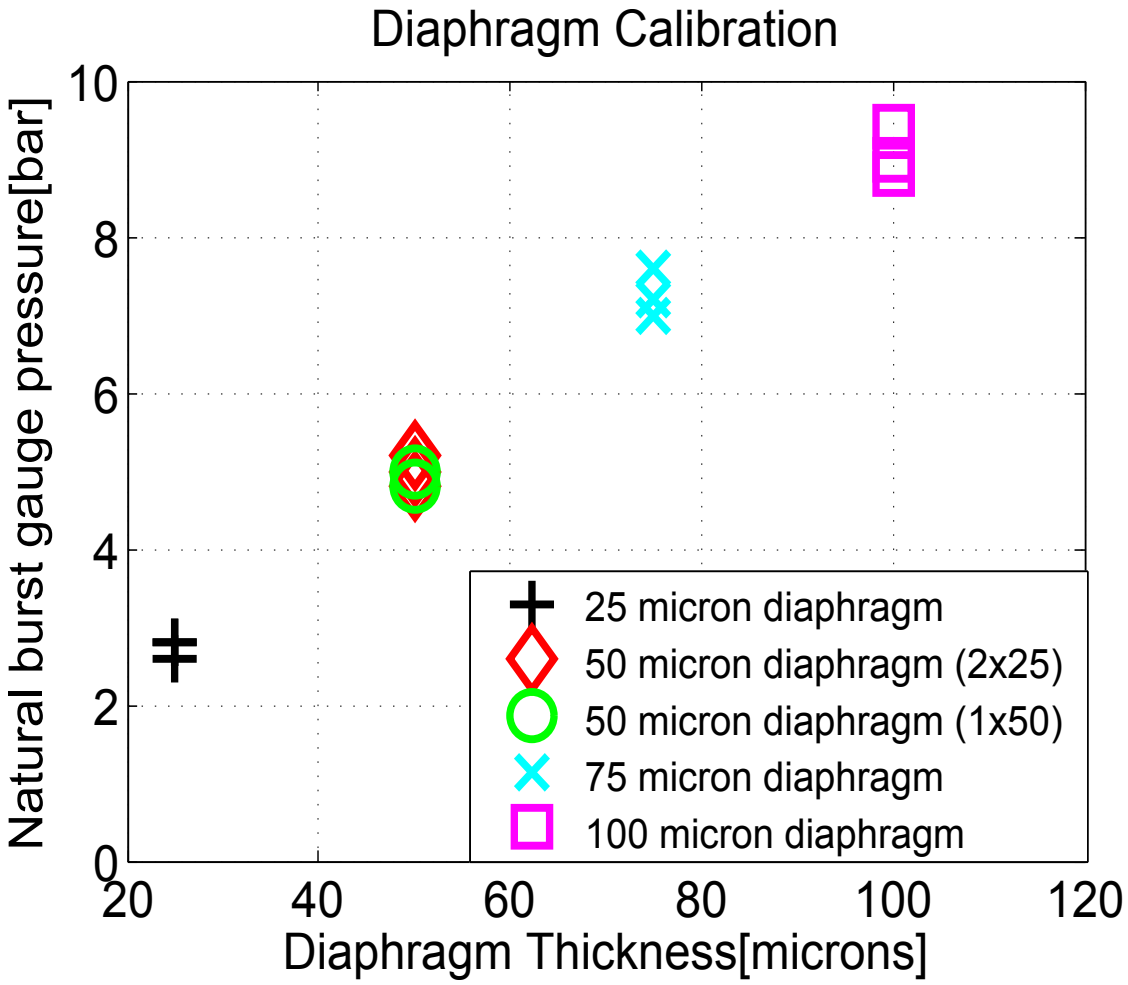


Figure 6.1: Diaphragm calibration.

6.2.2 Shock tube design validation

The length of the downstream section of the shock tube was critical for the present study. It was essential to prevent wave reflections from the end of the downstream pipe affecting the gap flow development. To ensure pressure transients in the downstream were solely due to the gap flow features, it was imperative as well to prevent the reflections. An optimum length was chosen from an initial CFD simulation. The results of the CFD simulation are now shown in Figure 6.2 as pressure plots. Frames are shown of the flow field at 6ms, 6.5ms and 7ms. The flow time is measured from the instant the incident shock exits the upstream pipe. A black solid line in all the frames indicates the furthest pressure measurement point in the downstream pipe as measured from the gap. This corresponds to the station numbered 5 in Figure 4.1 in chapter 4. The three frames show that at these later flow times, the reflected expansion wave from the pipe end does not affect the pressure field at all pressure measurement points. This is indicated by a uniform pressure caused by passage of the initial incident shock in the greater portion of the downstream pipe. The reflected expansion wave

still has not reached the pressure measurement points. This indicates the downstream pipe is long enough to investigate the propagation conditions for about 8ms without the effects of wave reflections.

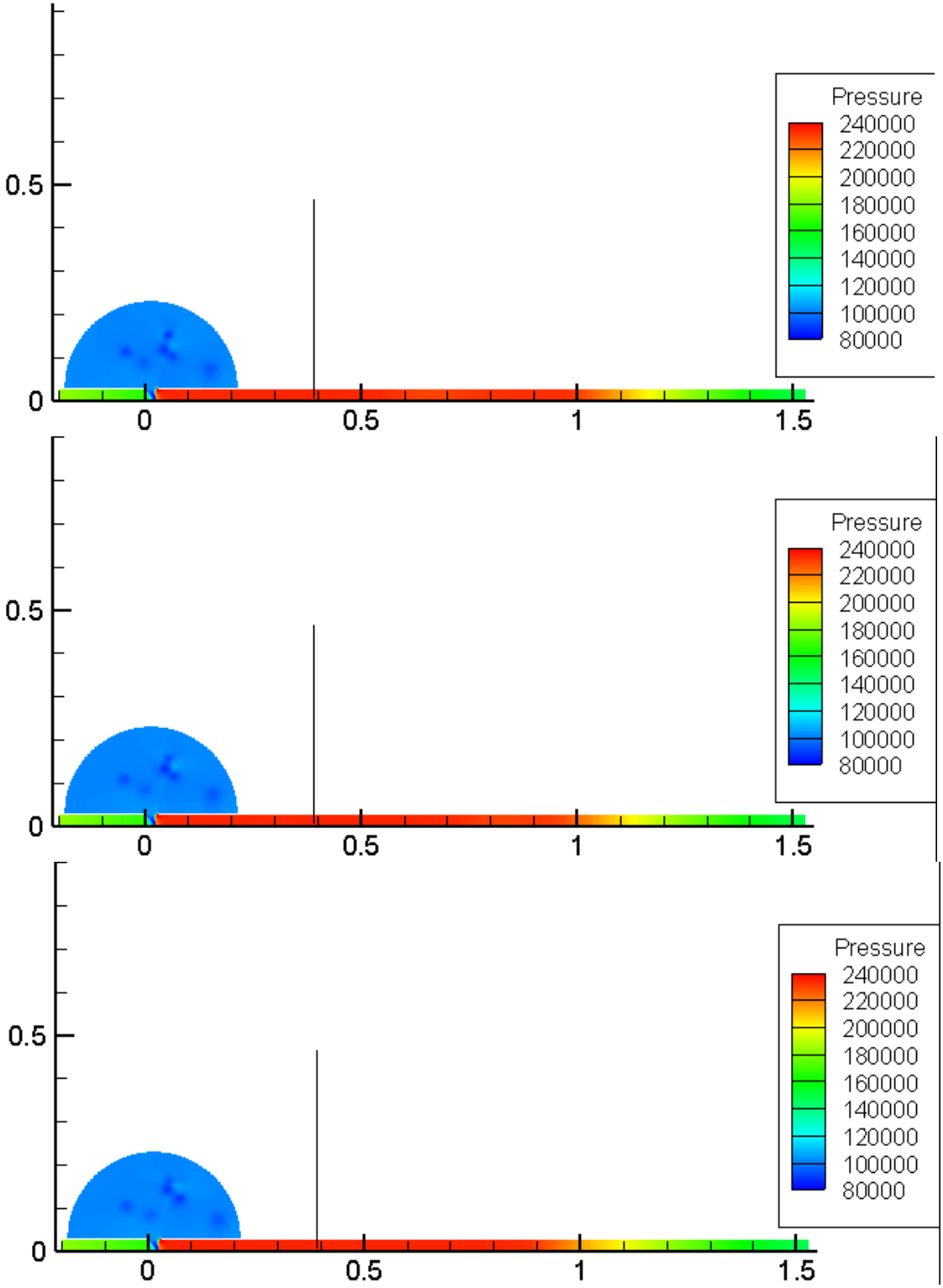


Figure 6.2: CFD pressure contours for a 30mm pipe gap at Mach 1.45. From the top, flow time at 6ms, 6.5ms and 7ms respectively.

6.2.3 Wave propagation in both pipes

The observations for the wave propagations were based on the primary output of the oscilloscope. The oscilloscope output were traces of voltage, in millivolts against time, in milliseconds. An example of such a trace is shown in Figure 6.3 for a pipe gap width of 310mm at a Mach number of 1.45.

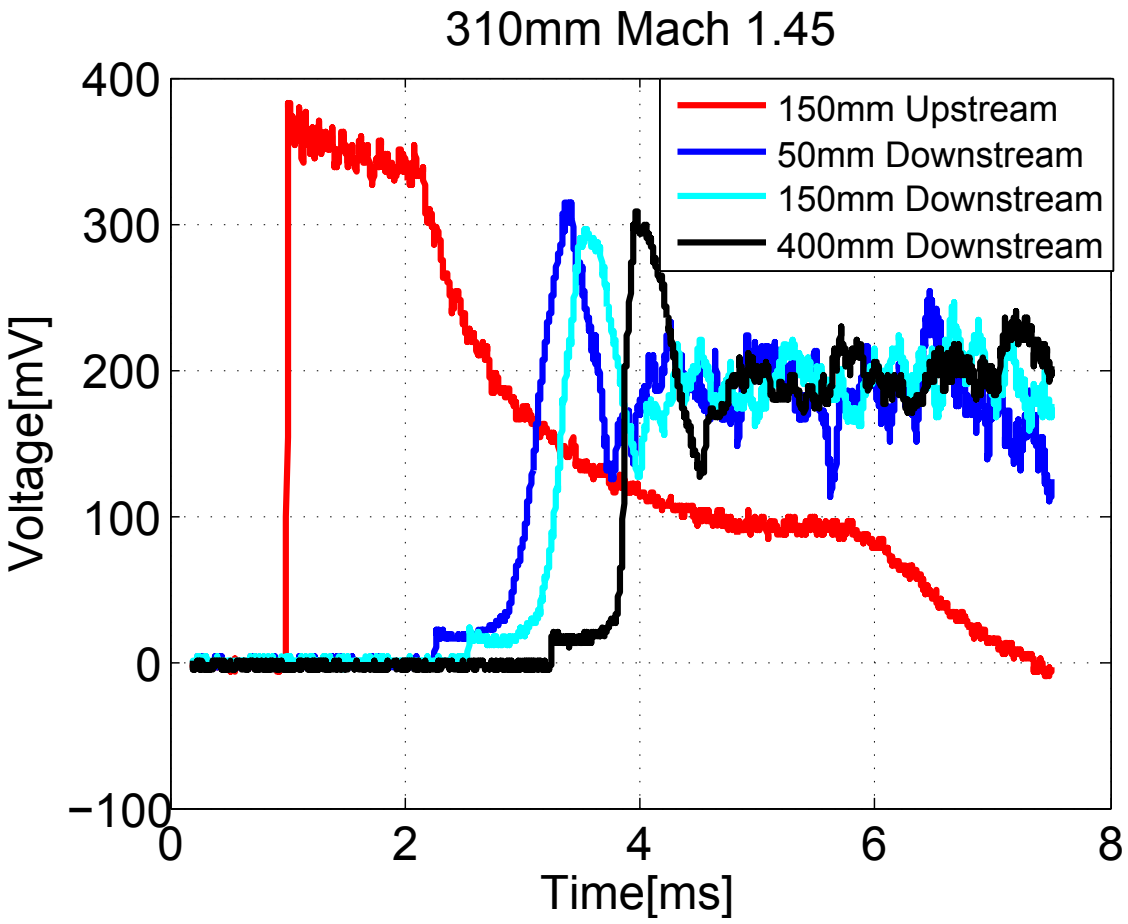


Figure 6.3: Voltage-time trace for a pipe gap of 310mm at Mach 1.45.

The voltage time trace shows an initial voltage spike in the upstream pipe which corresponds to the initial incident shock. Constant voltage follows the initial spike after the passage of the shock. The constant phase is then followed by a sudden reduction in voltage. This is due to an expansion wave travelling back in the upstream pipe from the gap.

For the downstream pipe, all the measurement points showed that the incident shock arrives at a much reduced strength from its original value. The incident shock voltage spike is then followed by a steady state phase of about 1ms. A voltage spike comparable in magnitude to the intial incident shock follows the steady state phase. This occurs as a standing shock develops at the inlet to the downstream pipe. As shown in Figure 6.3, this is observed at all the measurement points in the downstream pipe.

6.3 Data Processing

The raw data from the experiments and the numerical simulations will be processed for detailed analysis in later chapters.

6.3.1 Experimental Data Processing

6.3.1.1 Diaphragm Calibration

For the direct comparison of experimental and numerical results, it is desirable for the shock Mach numbers to be the same. The experimental shock Mach numbers will also be used to analyse the degree of repeatability for shock Mach numbers. Therefore it is important to calculate the experimental shock Mach numbers from the diaphragm calibration tests. The calculation will be outlined for the second test in the second diaphragm calibration test in Appendix D. The Mach number, M_a is given by equation(6.1).

$$Ma = \frac{V_s}{a} \tag{6.1}$$

Therefore the velocity of the shock and the sonic velocity in air have to be determined. Assuming air to be an ideal gas, the sonic velocity a, can be determined from equation(6.2).

$$a = \sqrt{\gamma RT} \tag{6.2}$$

For the test the absolute temperature was found to be 294.56K. Assuming a calorically perfect gas, the ratio of specific heats γ is 1.4 and the gas constant $R = 287.1$ J.kg^{-1}.K^{-1}. Substituting in equation(6.2), the sonic velocity is

$$a = \sqrt{(1.4 \times 287.1 \times 294.56)} = 344.09 m/s.$$

The shock velocity can be determined from the distance between two known measuring points and the time it takes for the shock to traverse the distance. Two pressure transducers in the upstream pipe placed at a distance, x of 587mm apart were used. The measure function from the oscilloscope software was used to determine the time it took the shock to traverse the distance. For the second test, the time t was determined to be 1.3ms. From this the shock velocity V_s is found to be,

$$V_s = \frac{x}{t} = \frac{890}{1.3} = 451.54 m/s.$$

From equations (6.1) and (6.2), the shock Mach number M_a can be determined.

$$M_a = \frac{V_s}{a} = \frac{451.54}{344.09} = 1.31 \pm 0.0151.$$

The uncertainity in the measurement of the shock Mach numbers using this method is outlined in Appendix E. The small uncertainities were contributed to the determination of the time by use of the measure function as well as measurement of transducer separation distance.

6.3.1.2 Wave propagation in both pipes

Since the primary measurements for pressure from the oscilloscope was in Volts, the data had to be processed to obtain the absolute pressures in bars. In addition to this a scaling factor had to be applied to the experimental results. This was necessary since the numerical simulations were done at an atmospheric pressure of 1 bar and the experiments were done at an atmospheric pressure of 0.83 bar. In this way validation and comparison of numerical results with experimental results was then possible.

Firstly the calibration constants from the pressure transducers were used to convert the Volts into bars. Four pressure transducers were used, the calibration constants for all of them was 2.417 bar/Volt. To ensure independence of atmospheric pressure between numerical and experimental results, a scaling factor of 1.205 (inverse of 0.83) was applied to experimental results. In addition to the conversion and scaling, the experimental pressures had to be converted to absolute pressures. This was because the CFD data through the use of Fluent's operating conditions were absolute pressures. Since an atmospheric pressure of 1 bar was used, 1 bar was added to the experimental gauge pressures. Equation(6.3) summarises the calculation of experimental absolute pressures,P_{abs}.

$$P_{abs} = VkS + P_{atm} \tag{6.3}$$

Where V is the measured voltage, k is the calibration constant, S is the scaling factor and P_{atm} is the atmospheric pressure.

The peak voltage in the upstream pipe for 310mm gap at Mach 1.45 will now be used as an example to calculate experimental absolute pressures. For this case the observed peak voltage was 300mV. Applying equation(6.3), the absolute pressure for this case is,

$$P_{abs} = 0.300 \times 2.417 \times 1.205 + 1 = 1.87bar.$$

Using equation(6.3) the raw voltage-time plots in csv format were processed in Matlab to give the pressure-time plots. The pressure-time profiles will be used in later sections of the report to analyse the transient flow in both the upstream and downstream pipe.

For signal noise elimination, the pressure-time plots were also filtered in Matlab. A second order Butterworth filter was used.

6.3.1.3 Experimental flow visualisation

A Canon camera flash was used as the light source in the shadowgraphy visualisation system for the first experimental runs performed. Although the flash is a microsecond duration the disadvantage of this was that the light intensity varied from earlier frames to the later frames. The contrast and brightness of the later images was affected. To maintain higher resolution to visualise the flow features, the image contrast and brightness for the later frames was adjusted by a free online software called Lunapic.

6.3.2 CFD Data

The Fluent solver used for the numerical simulations produced case and data files. The post-processing was done in the commercial packages Tecplot© and Ansys Results©. In Tecplot contours of density, velocity ,Mach number were extracted from the case and data files. Streamlines were plotted to show the velocity vectors at various positions within the computational domain. As an adaptive mesh was used with Fluent, Tecplot was also used to track the mesh topology evolution as the simulation progressed. For later comparison and validation of CFD results with experimental results, numerical shadowgraphs were also extracted using Tecplot. The calculation of variables feature in Tecplot was used to display the numerical shadowgraphs. Tecplot uses the divergence of the density to calculate the numerical shadowgraphy variable. In Ansys Results, pressure time profiles were extracted at specified positions.

Three dimensional numerical results were also post-processed with Tecplot. From the data, isosurfaces of vorticity were plotted. It did a good job of showing the vortex rings and subsequent leapfrogging and the three-dimensional effects.

7 Results

7.1 Introduction

Processed results are now presented in this chapter. The flow times indicated in the images unless otherwise stated, are measured from the instant the incident shock exits the upstream pipe.

7.2 CFD Validation

Before explaining any physics with numerical results, computational solutions must be validated. It is necessary because not only modelling of physical phenomena often induces some simplifications both in governing equations and boundary conditions but also good agreement between numerical and experimental results is helpful for confirmation of the observed physical phenomena. Since the shock-wave phenomena in the present study are highly transient and their topological structures are over the whole flow field, it is usually not sufficient to compare numerical simulations with a limited set of point measurements from experiments. Only a comparison with a whole flow field measurement by some non-intrusive techniques can give confidence in numerical results. Since the experimental results were shadowgraphs, the strategy of creating numerical shadowgraphs for direct comparison with experiments was chosen. From the position of flow features like shock waves, the accuracy of numerical simulations can be estimated.

An initial shock wave propagating with a Mach number of 1.6 past a pipe gap width of 40mm was simulated as the first case to compare with experimental results. Numerical shadowgraphs constructed from the numerical solutions are shown together with the experimental shadowgraphs in Figure 7.1. Figure 7.2 compares the experimental shadowgraphs with density contours. The experimental shadowgraphs are shown in the upper symmetrical half of each frame whilst the numerical shadowgraphs and contours in the lower symmetrical half.

Figure 7.1and Figure 7.2 shows the shock wave flow development after the precursor planar shock wave is discharged from the pipe end into the pipe gap.

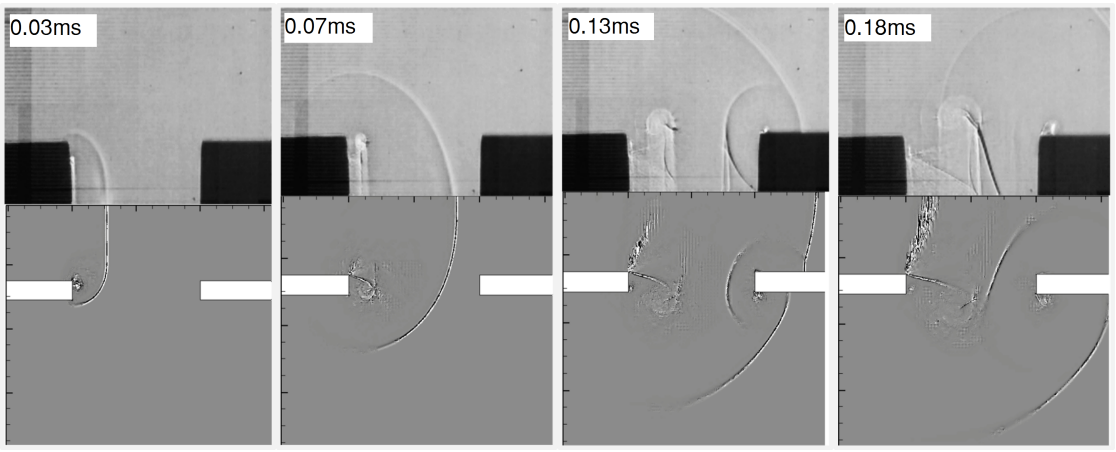


Figure 7.1: Comparison of experimental shadowgraphs(upper half) and numerical shadowgraphs(lower half) for 40mm gap Mach 1.6.

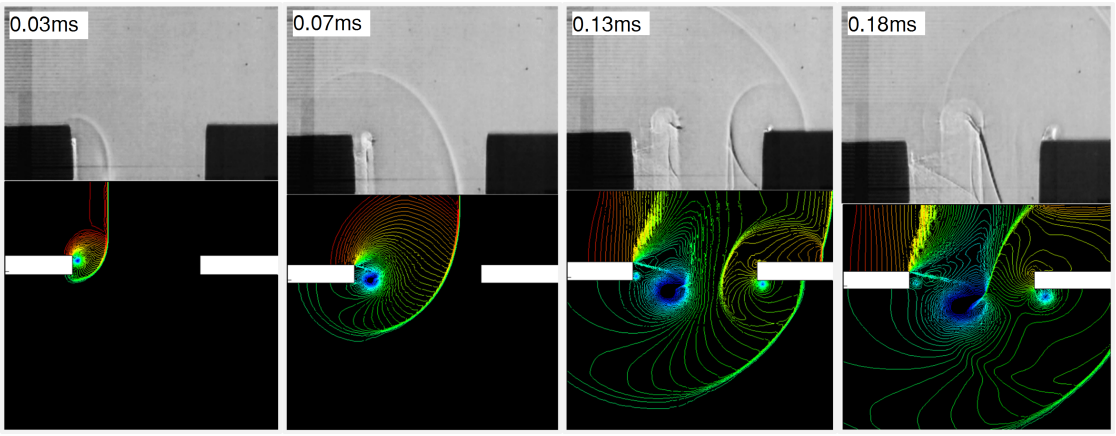


Figure 7.2: Comparison of experimental shadowgraphy(upper half) and numerical density contours(lower half) results for 40mm gap Mach 1.6.

By looking at both sets of comparison, it is shown that agreement between CFD and experiment is good. This is so because the position of the shocks and other flow features is well overlapped and in the same positions with minor exceptions. The minor exceptions in the positions of the flow features in the two symmetrical halves are around about half a millimetre. Considering difficulty in timing numerical results to match exactly with experiments, this level of verification is perfectly acceptable to validate that the numerical simulations representing the pipe gap flow.

For further verification, the experimental and numerical shadowgraphs of a pipe gap for 80mm at Mach 1.6 are shown in Figure 7.3.

Again agreement between CFD and experiment is shown to be generally good.

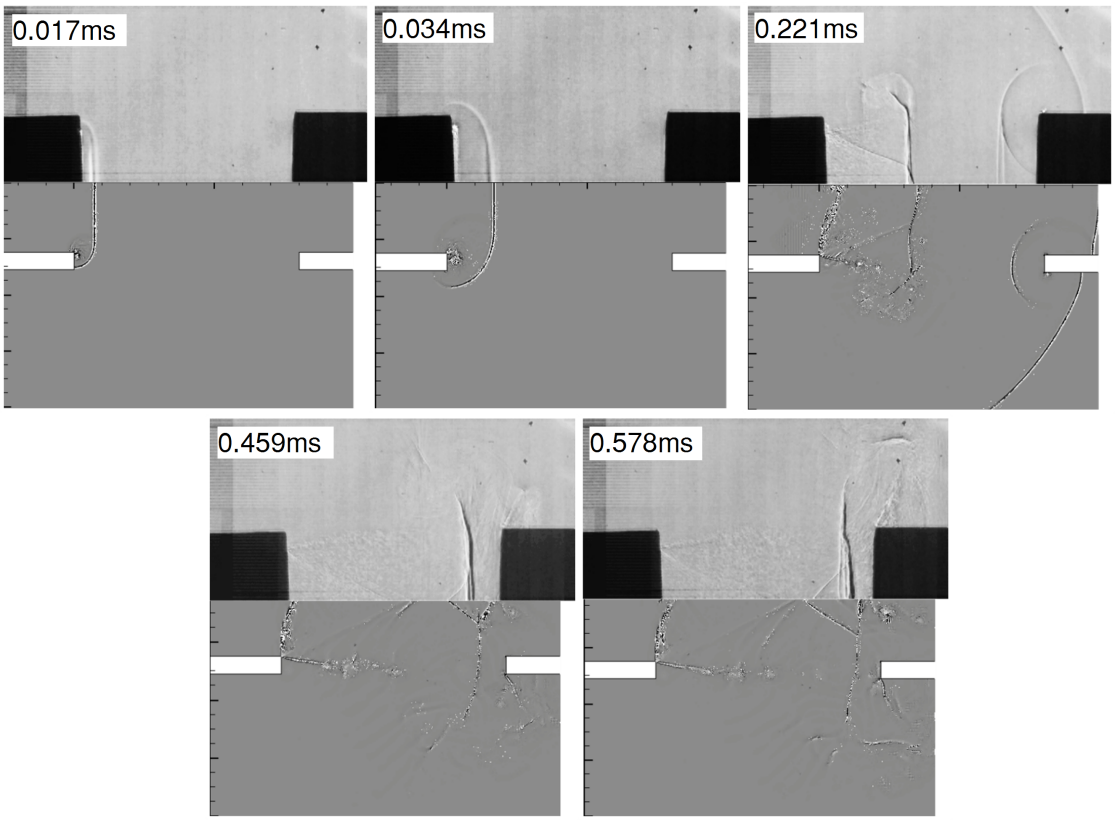


Figure 7.3: Comparison of experimental shadowgraphs(upper half) and numerical shadowgraphs(lower half) for 80mm gap Mach 1.6.

7.3 Diaphragm calibration

The shock Mach numbers produced for the different natural diaphragms burst were analysed. Figure 7.4 shows the variation of the diaphragm thickness with the shock Mach number produced. The scatter plot shows that for the same diaphragm thickness and combination, the variation in the Mach number was minimal over the three tests.

The degree of variation in the Mach number is further shown in Table 7.1. For each diaphragm thickness and combination, the standard deviation for the three shock Mach numbers was calculated. From this, the coefficient of variation was derived to measure the dispersion. For all the diaphragm thicknesses, the percentage variation over the three tests was less the 2%. Standard practise entails the shock Mach numbers produced over three tests to be within 2% of each other. This shows the present natural diaphragm bursts is capable of good repeatability of the test conditions.

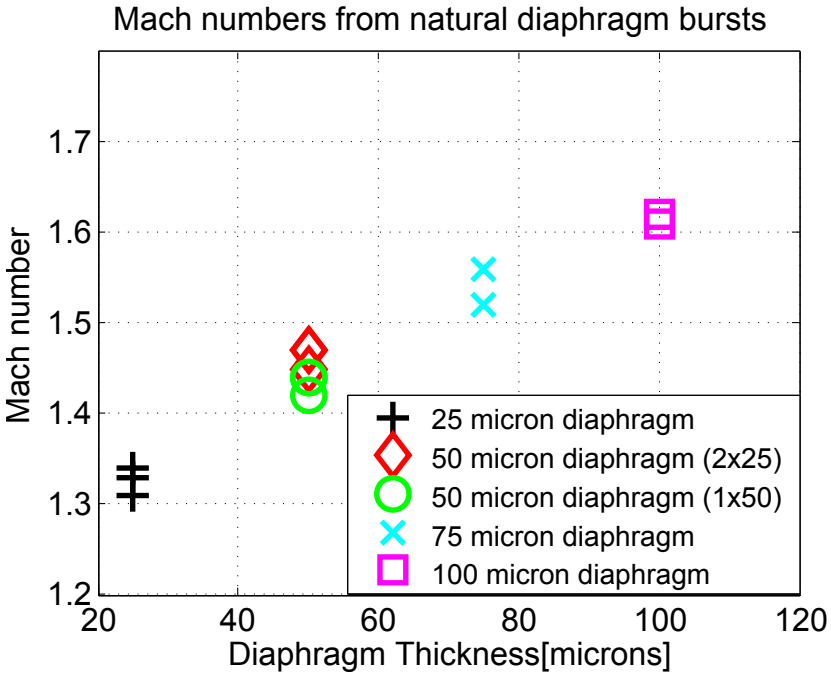


Figure 7.4: Diaphragm calibration.

Table 7.1: Variation of Mach number for different diaphragm bursts

Thickness	**Diaphragm combination**	**Standard deviation**	**Variation(%)**
25micron	$1 \times 25microns$	0.0153	1.15
50micron	$2 \times 25microns$	0.0115	0.79
	$1 \times 50microns$	0.0115	0.81
75micron	$3 \times 25microns$	0.0231	1.49
100micron	$2 \times 50microns$	0.0058	0.36

7.4 Transient flow in the upstream and downstream pipe

The transient flow in the upstream and downstream pipe is best shown by the experimental pressure-time profiles. The profiles show the wave propagation and subsequent wave interactions in both pipes with the passage of the shock wave past the gap. Supplementary results for the experimental pressure time profiles are shown in Appendix C

7.4.1 Upstream pipe flow

Such a pressure-time profile is shown in Figure 7.5 for the transient flow for a pipe gap of 60mm at Mach 1.45. The test time is approximately 8ms measured from the time the incident shock passes the 150mm upstream pressure transducer. The distances of the individual pressure transducers is measured from the pipe gap.

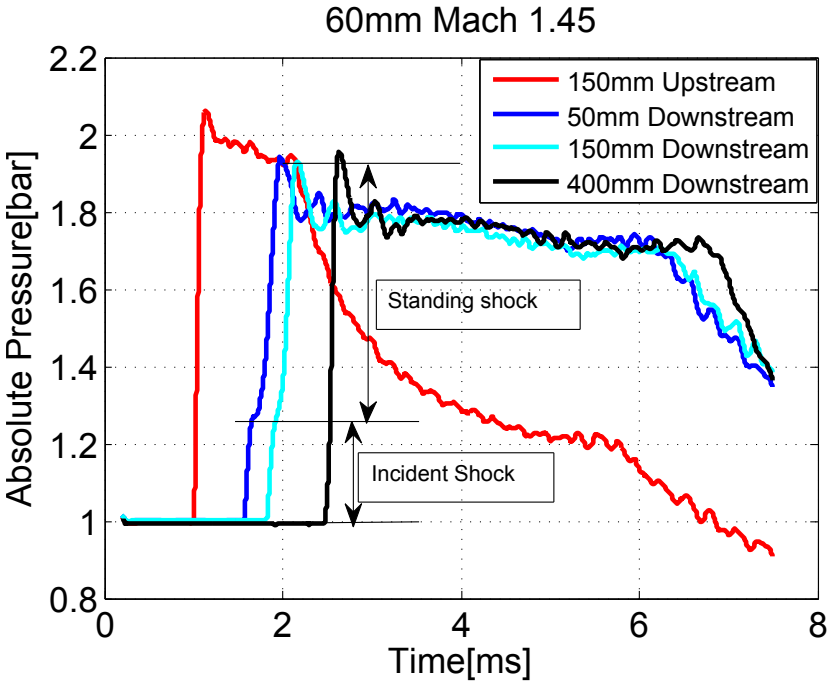


Figure 7.5: Pressure time profiles for a pipe gap of 60mm Mach 1.45.

The 150mm upstream transducer placed in the upstream pipe shows the initial pressure spike due to the arrival of the incident shock. The flow briefly attains steady-state for about 1ms. This is then followed by an expansion shown by the significant drop in pressure in the initial incident shock post-shock flow. The drop in pressure is caused by the propagation of a strong expansion wave into the flow in the upstream pipe. This expansion wave results from the outflow of the gas from the upstream pipe. As the shock-accelerated gas exits the upstream pipe, an initially curved expansion wave is generated at the lip of the pipe and propagates back in the high-subsonic upstream flow.

With the passage of the expansion wave past the upstream pipe transducer the flow tends to become steady state. The steady-state phase lasts for about 2ms and is then followed by another expansion which further reduces the pressure to below atmospheric pressure. As this further pressure reduction occurs at much later times, its likely to be caused by the arrival of the expansion waves reflected from the end wall of the driver section.

7.4.2 Downstream pipe flow

The transient flow in the downstream pipe was monitored by three pressure transducers placed at 50mm, 150mm and 400mm from the gap respectively. For all the three transducers, two distinct pressure spikes are noticeable. As shown for the annotated 50mm transducer, the initial pressure spike is due to the arrival of the incident shock. The initial spike shows that

the incident shock propagates in the downstream pipe at a much reduced strength compared to its initial strength in the upstream pipe. Thus the pipe gap has the effect of attenuating the strength of the incident shock wave. The magnitude of the initial pressure spike is shown to gradually decrease from the 50mm to the 150mm transducer. This shows that as the incident shock propagates in the downstream pipe, it continues to gradually lose its strength.

A phase which is very short in time follows the initial pressure spike. The pressure is fairly constant for the short phase. The development of the boundary layer was suggested as the possible cause for the existence of the short constant pressure phase. The short constant pressure phase is followed by a second pressure spike. The second pressure spike which is comparable in magnitude to the incident shock pressure rise in the upstream pipe is due to the development of a standing shock wave at the downstream pipe entrance. The occurrence of the second pressure spike with the formation of the standing shock is explained by CFD pressure contours in Figure 7.6 for the same test conditions.

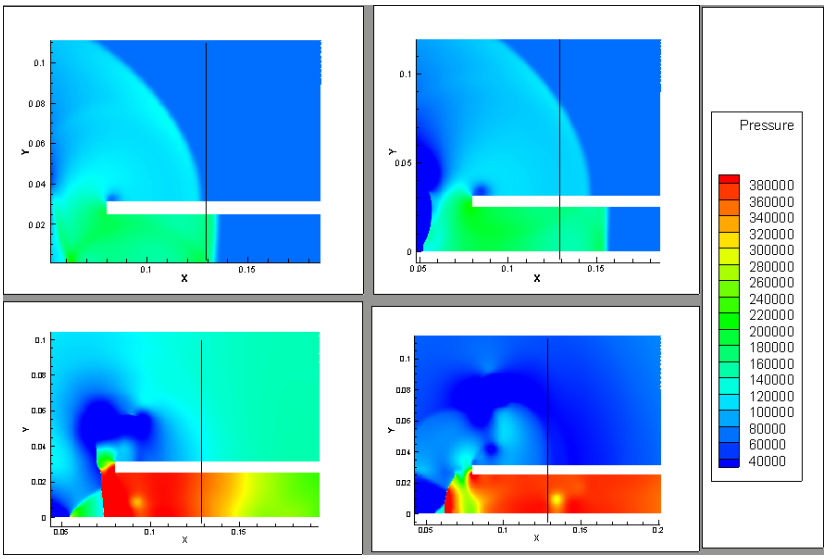


Figure 7.6: CFD pressure plots for 60mm pipe gap at Mach 1.45.

To compare with the experimental pressure profile for the 50mm pressure transducer, a black solid line is drawn in the CFD pressure contour at the 50mm point from the gap. It shows that after the passage of the incident shock wave, there is an initial pressure rise as shown in the first two frames of Figure 7.6. After a short duration of constant pressure, a standing shock wave develops at the inlet to the downstream pipe as shown in the third frame. This results in the second pressure spike.

Following the development of the standing shock, both the experimental pressure time profiles and CFD plots shows that the downstream pipe flow tends to become more uniform. This shows the downstream pipe flow development is mainly controlled by the blockage caused by the standing shock wave at the downstream pipe inlet.

At much later times, the experimental pressure profiles show a gradual pressure decrease for all the transducers following the uniform phase. This is explained by reflections of the incident shock off the pipe end. The reflections propagate back in the downstream pipe as expansion waves.

7.4.3 Effect of gap width and shock Mach number

The observations from the oscilloscope data was fairly similar for the higher Mach number of 1.6. The notable observation being that the post-incident shock pressure reduction in the upstream pipe was very gradual. This is due to the expansion wave barely propagating back in the relatively stronger flow. This is shown in Figure 7.7 for the pressure time trace for a 60mm pipe gap at Mach 1.6.

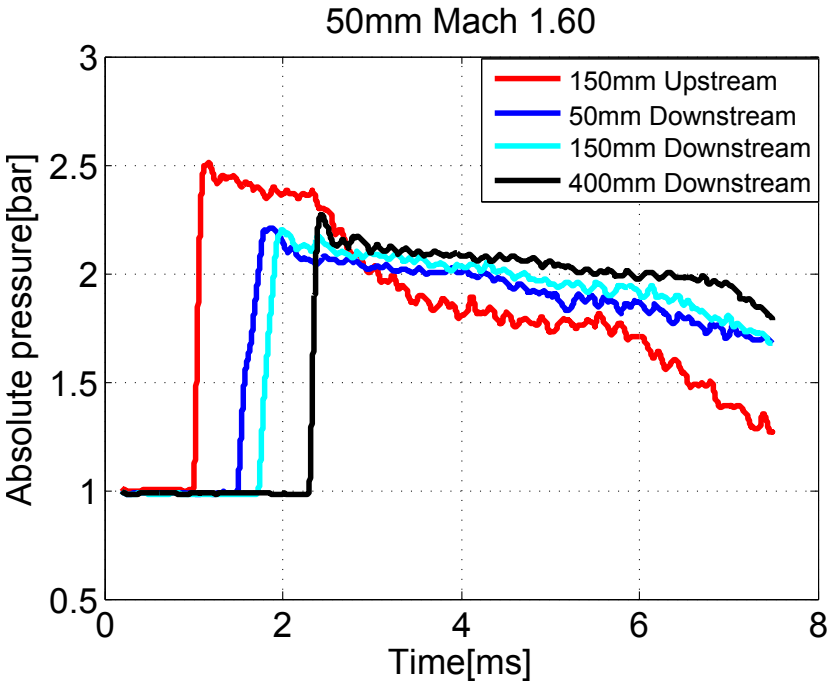


Figure 7.7: Pressure time profiles for 60mm pipe gap at Mach 1.6.

The effect of a lower Mach number is shown for 60mm Mach 1.3 in Figure 7.8. Two effects are noticeable for the relatively low Mach number. Firstly, the pressure reduction in the upstream pipe due to the expansion wave was more steep as compared to the reduction for Mach 1.45. This shows the expansion wave for Mach 1.3 readily propagates back in the relatively slow subsonic flow issuing from the upstream pipe. Secondly, the initial pressure spike due to the incident shock in the downstream pipe was significantly less as compared to that for Mach 1.45. This is explained by the relatively weak incident shock of Mach 1.3.

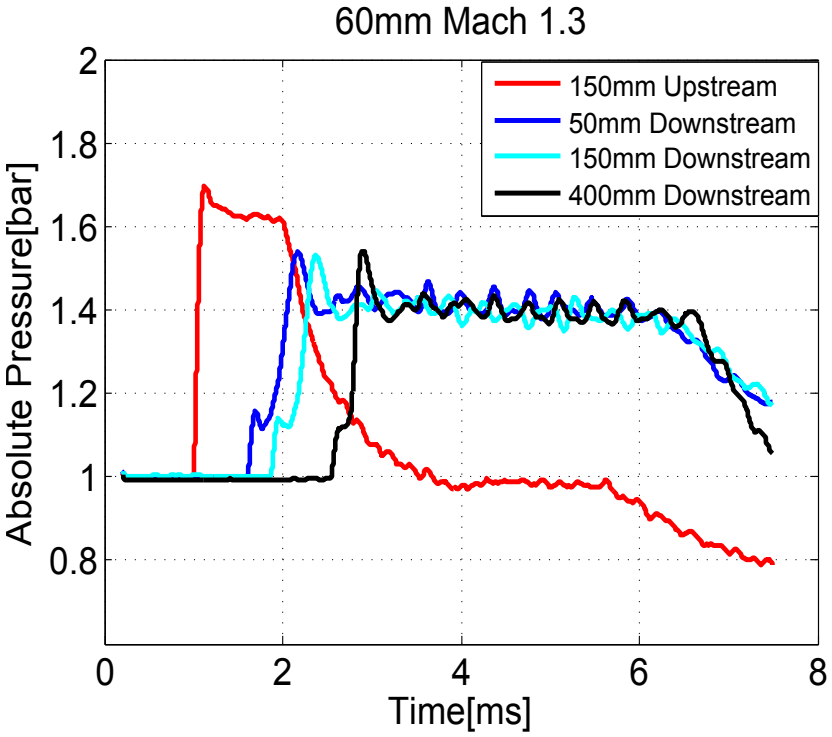


Figure 7.8: 60mm pipe gap at Mach 1.3 pressure-time profiles.

The effect of gap width is shown in Figure 7.9 for a relatively large gap of 180mm. The strength of the incident shock in the downstream pipe is significantly reduced for this gap width. At all the downstream measurement points, after the arrival of the incident shock, there is relatively a longer constant pressure phase before the second pressure spike. This indicates the standing shock takes a relatively longer time to form in comparison with the smaller gap width.

Incident shock overpressures in the downstream pipe were used to ascertain the influence the shock Mach number and gap width have on the propagation conditions downstream. The overpressures were measured at the 50mm downstream transducer for gaps of 40mm to 310mm and Mach numbers of 1.45 and 1.34. The results are shown in Figure 7.10 as a scatter plot. For a given Mach number, the magnitude of the overpressure monotonically decreases with an increase in gapwidth. This is to be expected as the incident shock and hence the overpressure gets much weaker with an increase in gap width. For the larger gap widths, the overpressures tend to become fairly constant as the gap width increases.

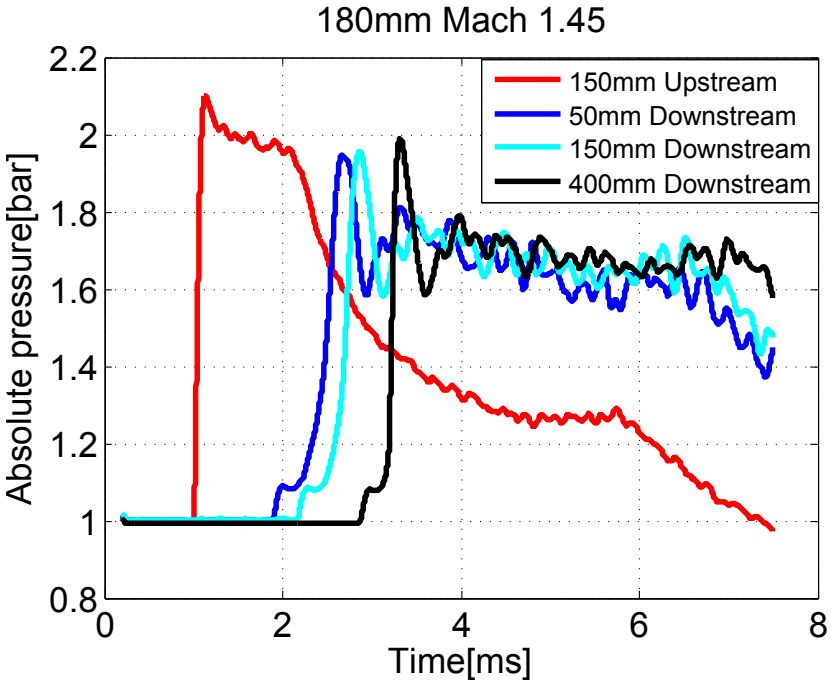


Figure 7.9: Pressure time profiles for 180mm pipe gap at Mach 1.45.

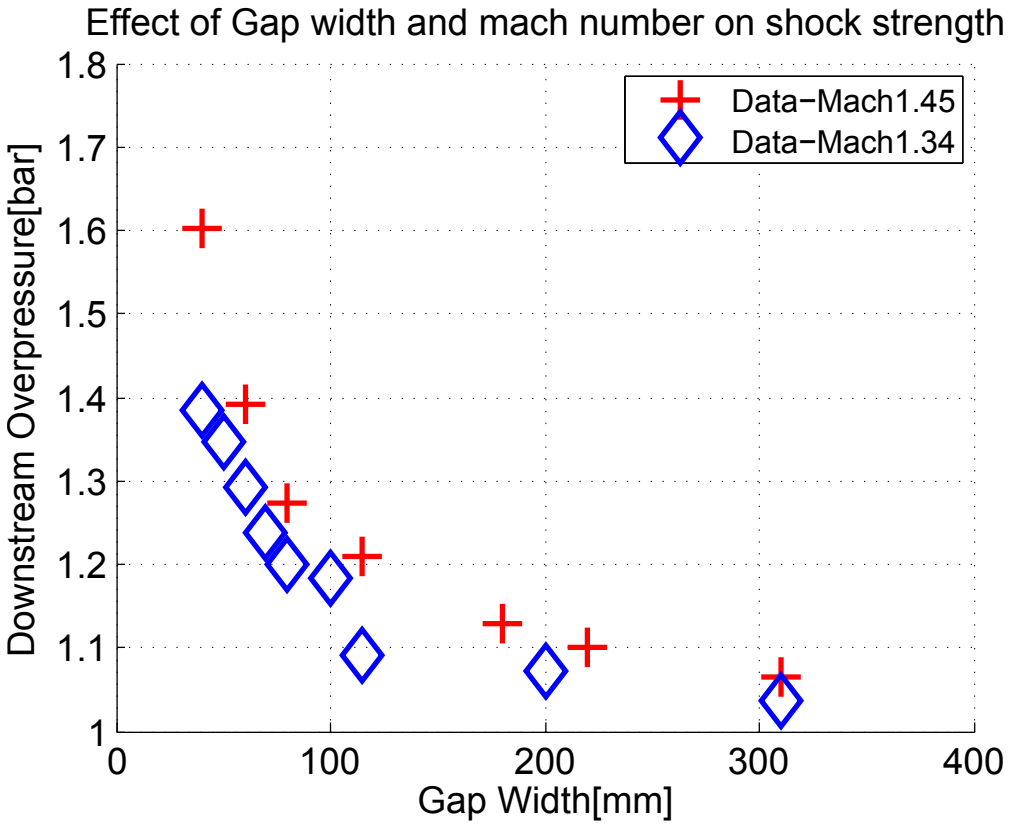


Figure 7.10: Effect of shock Mach number and gap width on downstream pipe flow.

7.5 Experimental flow visualisation

7.5.1 Pipe gap

Early stages of flow development for a pipe gap of 40mm and Mach 1.45 are shown in Figure 7.11. In the first frame, the incident shock diffracts around the exit of the upstream pipe and a toroidal vortex is shed. At 0.16ms in the second frame, the incident shock strikes the entry to the second pipe and reflects off it and the incident shock continues down the downstream pipe. The structure of the reflected shock suggests a portion reflects off the thickness of the pipe and the other off the pipe interior. For the portion that reflects off the pipe interior, its two curved portions approach the axis and will evidently focus at the axis at later times. In the third frame the second shock forms within the plane of the primary vortex ring as a result of the outflow in the pipe gap attaining supersonic speeds. A barrel shock issues from the lip of the upstream pipe below the shear layer. The barrel shock reflects from the axis, and the reflected component's one end interacts with the primary vortex ring. At the same time, the flow at the downstream pipe results in a second vortex ring due to flow separation. The frames at 0.42ms and 0.48ms show the early stages of the interaction of the primary and secondary vortex ring. At 0.42ms, the primary and secondary vortex ring are joined by a shock embedded between their centres. A separation line attaches the secondary vortex ring to the downstream pipe. At 0.48ms, vortex leapfrogging starts. The second vortex ring starts to move to the left and over the primary vortex ring. At the same time the vortex leapfrogging produces a shock that moves upstream.

The later stages of flow development are shown in Figure 7.12. In the first frame, a stationary standing shock develops at the entrance of the downstream pipe as the outward flow develops. In the second frame, the flow becomes increasingly turbulent and, unlike the earlier stages, rather than moving to the right moves to the left due to the velocity field induced by the presence of adjacent surfaces. In the last frame, the stationary standing shock oscillates in its position and an unsteady shock structure appears at the inlet to the downstream pipe.

7.5.2 Flange Gap

Flow development for a 50mm flanged gap at a Mach number of 1.45 is shown in Figure 7.13. In the first frame of Figure 7.13 the incident shock emerges from the upstream pipe it diffracts along the surface of the upstream face of the flange as the flow is confined for longer in between the flanges. In the second frame, a portion of the incident shock reflects off the surface of the downstream face of the flange and the other portion off interior of the pipe. The reflected shock then interacts with the vortex ring in a typical axisymmetric shock-vortex interaction

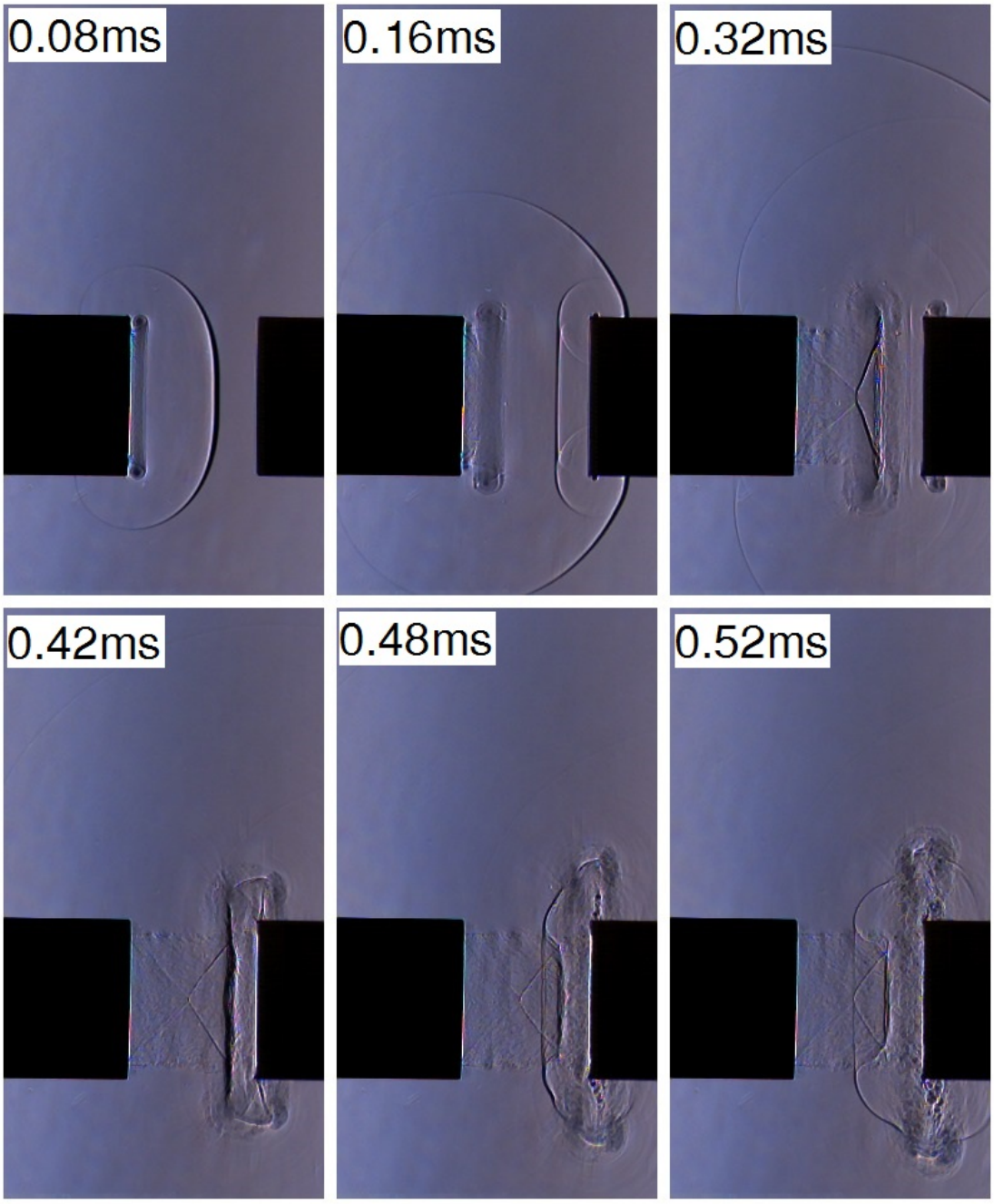


Figure 7.11: Early stages of propagation of a shock wave through a 40mm pipe gap at Mach 1.45

in the third frame at 0.24ms. The portion reflected from the flange surface is accelerated and moves upstream whilst the portion reflected off the pipe interior decelerates and moves downstream with the primary vortex ring. At the same time the incident shock diffracts around the bolt holes at the downstream flange. At 0.38ms, the reflected shock wave re-reflects off the upstream face of the flange, catches up with the primary vortex ring and interacts with it in a second shock-vortex interaction. The re-reflected shock appears to be bent as it emerges from the interaction. The diffracted shocks from the bolt holes also

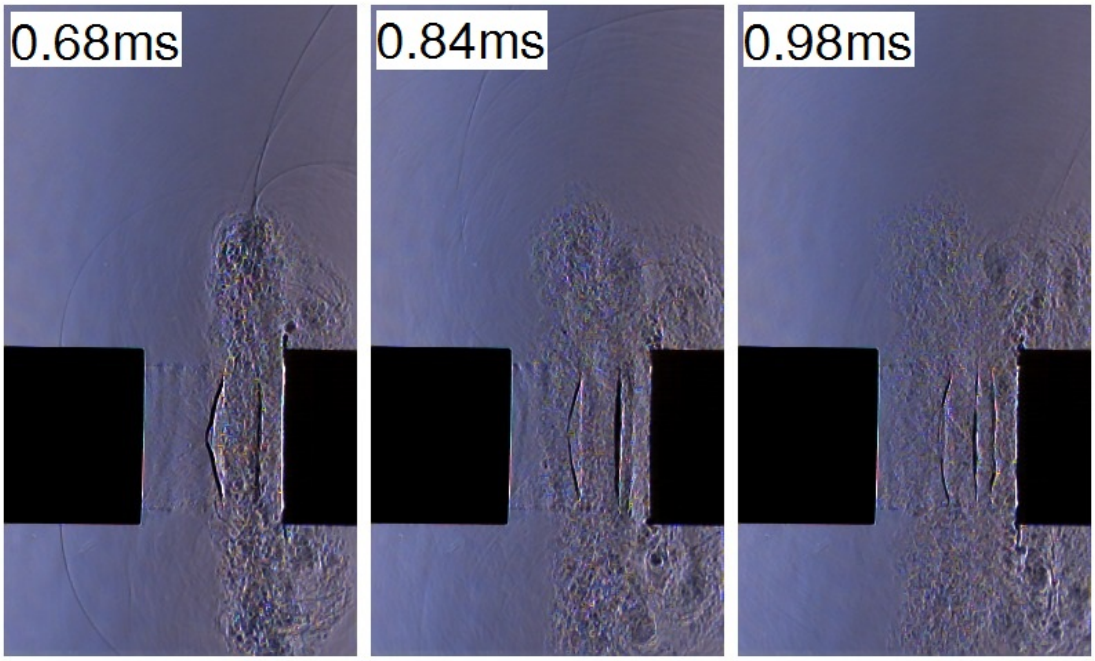


Figure 7.12: Later stages of propagation of a shock wave through a pipe gap of 40mm at Mach1.45

produce small vortex rings issuing out from the bolt holes. The flow separation at the outer radius of the flanges also produce two small vortex rings at the same time.

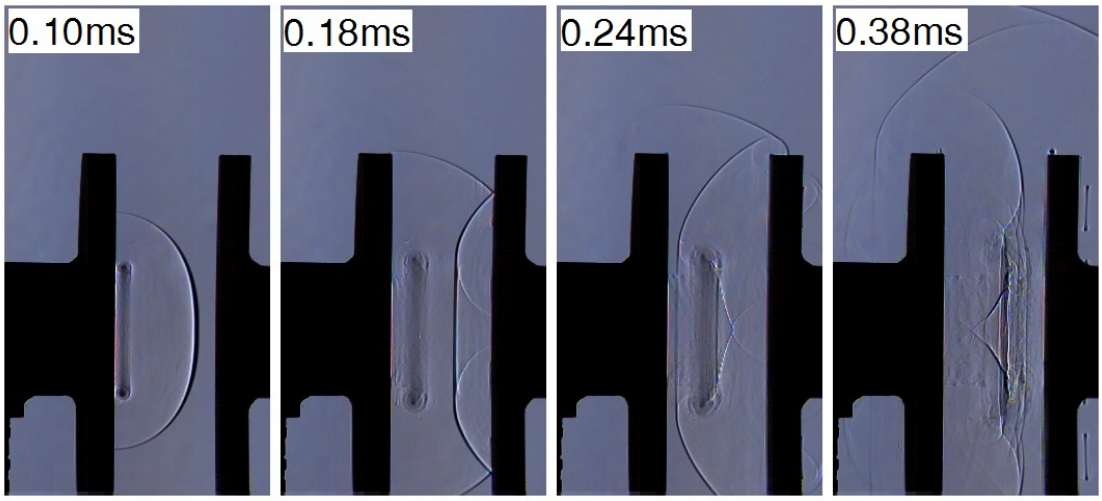


Figure 7.13: Early stages of propagation of a shock wave through a 50mm flanged gap at Mach 1.45

Figure 7.14 show later stages of flow development. The first three frames show flow development at the downstream flange surface. In the first frame, the primary vortex impinges on the downstream face flange. In the second frame, the primary vortex ring grows in its diameter and moves radially outwards along the downstream flange surface. At the same

time, a second vortex ring appears at the downstream flange surface due to the flow separating along the flange surface. In the third frame, the primary vortex ring starts moving to the left and interacts with the second vortex ring. The exact interaction of the primary and second vortex ring cannot be assessed. At 0.68ms the vortex rings breakdown and the flow in the gap becomes more turbulent. The turbulent plume exits from the gap with acoustic waves continually being emitted from the gap. The last two frames show the development of a complex standing shock system at the inlet to the downstream pipe as the jet within the flange gap goes to supersonic velocity. The standing shock oscillates in its position as the flow emerging from the upstream pipe is perturbed and continually oscillates as well.

7.6 CFD Results

7.6.1 Pipe gap

The CFD simulation results are shown in Figure 7.15 as pressure contours for a pipe gap of 80mm at Mach 1.6. At 0.085ms, the shock exits the pipe and diffracts around it. The flow expands into the gap and a vortex ring is shed as separation occurs at the pipe exit. At 0.221ms, an expansion wave propagates back into the upstream pipe. A strong Prandtl-Meyer expansion fan develops near the pipe exit as the gas upon exiting the upstream pipe goes to supersonic velocity. The supersonic outflow velocity results in a barrel shock with its one end attached to the pipe lip. The barrel shock has its other end attached to the shock formed in the plane of the vortex ring. The interaction evidently results in the distortion of the shape of the vortex plane shock. In the downstream pipe, the incident shock reflects off the interior of the pipe. The frame at this instance suggests a Mach reflection pattern.

At later times as shown at 0.425ms, the expansion wave moves further in the upstream pipe decreasing the post-shock pressure. Multiple vortices in the shear layer from the upstream pipe suggests the initiation of shear-layer instabilities. A second vortex ring at the downstream pipe starts to interact with the primary vortex ring. The incident shock in the downstream is shown to propagate with a reduced strength as compared to the post-shock pressure in the upstream pipe. The frame at 0.578ms shows the development of the standing shock. As the standing shock develops, its presence at the downstream pipe inlet clearly controls the pressure in the downstream pipe. The pressure increases to a value comparable to the post-shock pressure of the upstream pipe. As the standing shock develops, an unsteady flow in the downstream pipe near the inlet is evident. A small vortex forms as shown by the small low pressure region.

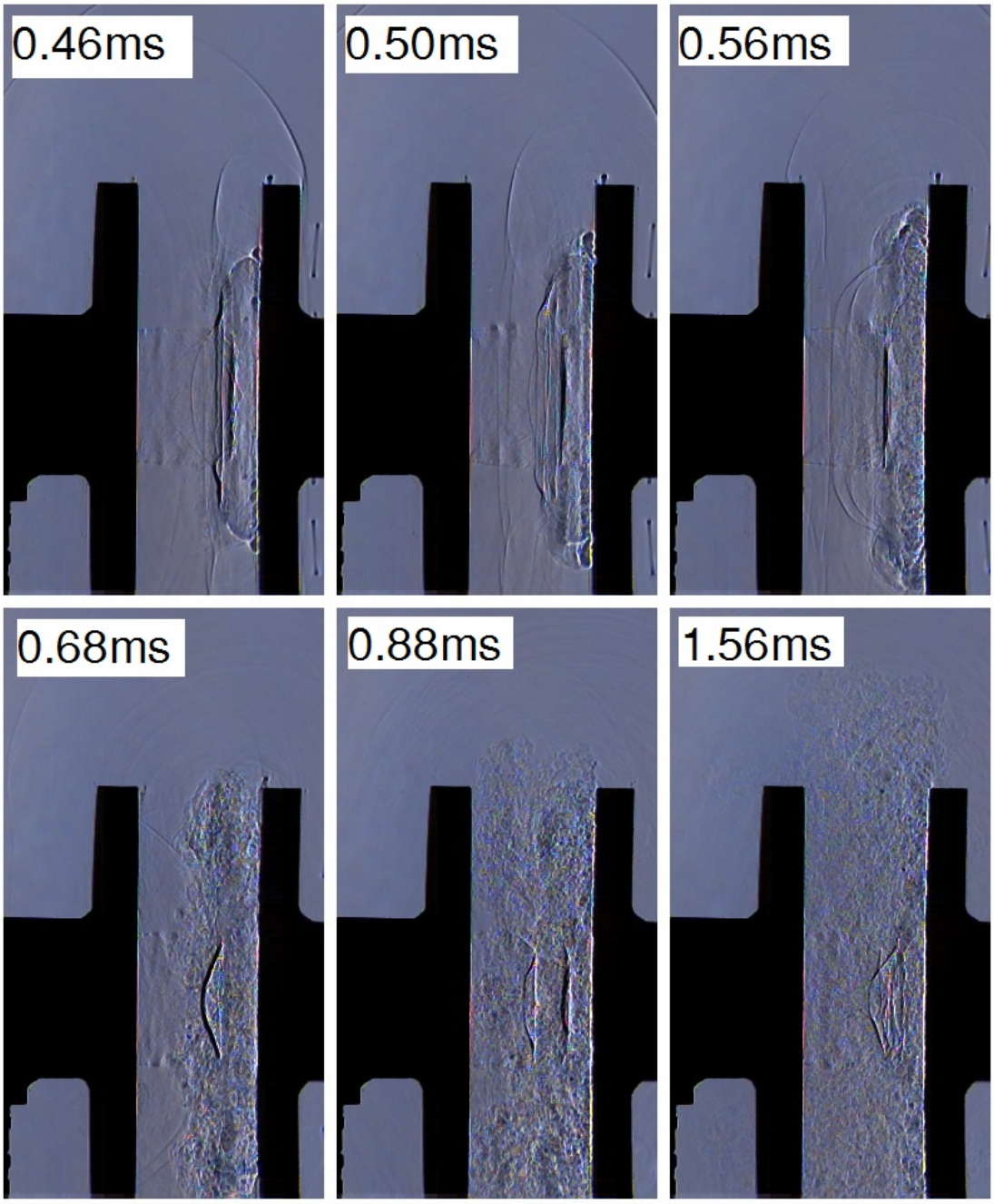


Figure 7.14: Later stages of propagation of a shock wave through a 50mm flanged gap at Mach1.45

7.6.2 Flange gap

The CFD development for a flange gap is shown in Figure 7.16. The streamtraces which are coloured by velocity show the formation of the vortices and their subsequent interaction with the flange surfaces. In addition to the main vortex ring, the radial outflow between the flanges causes two vortex rings to be shed at the outer radius. The second and third frame show the

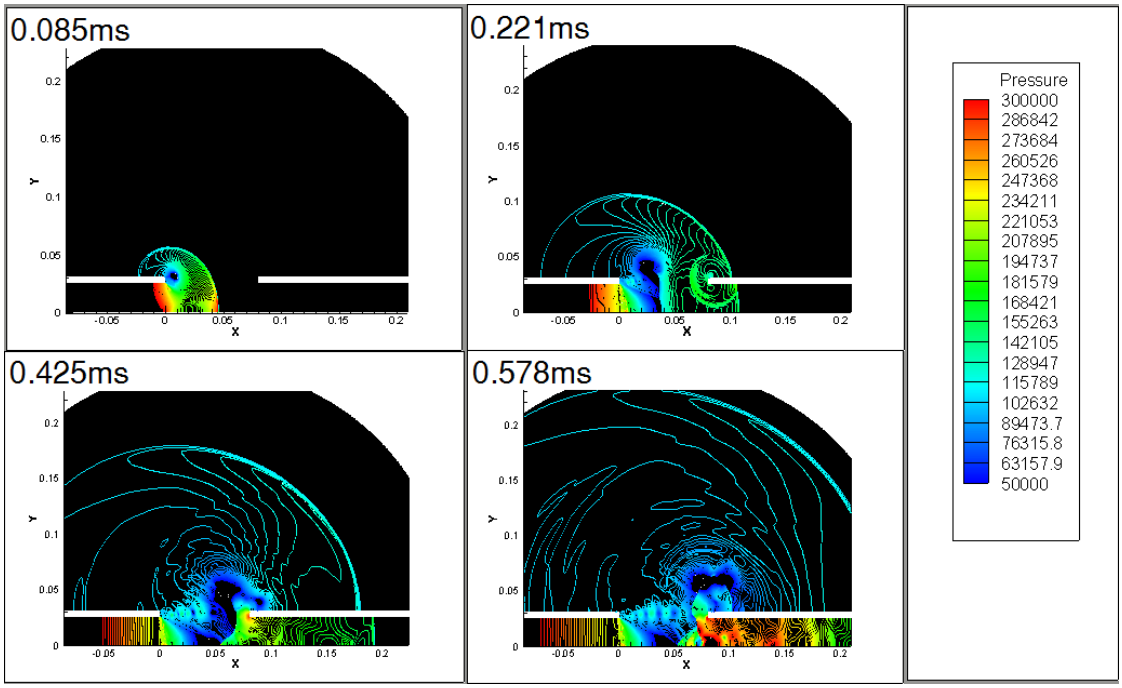


Figure 7.15: CFD pressure plots for a 80mm pipe gap at Mach 1.60

interaction of the main vortex ring with the downstream flange surface. High velocities are attained along the flange surface and becomes locally supersonic in some regions. The last frame shows the interaction of the main vortex ring and one of the outer radius vortex rings. The outer vortex rings is shown to leapfrog over the main vortex ring.

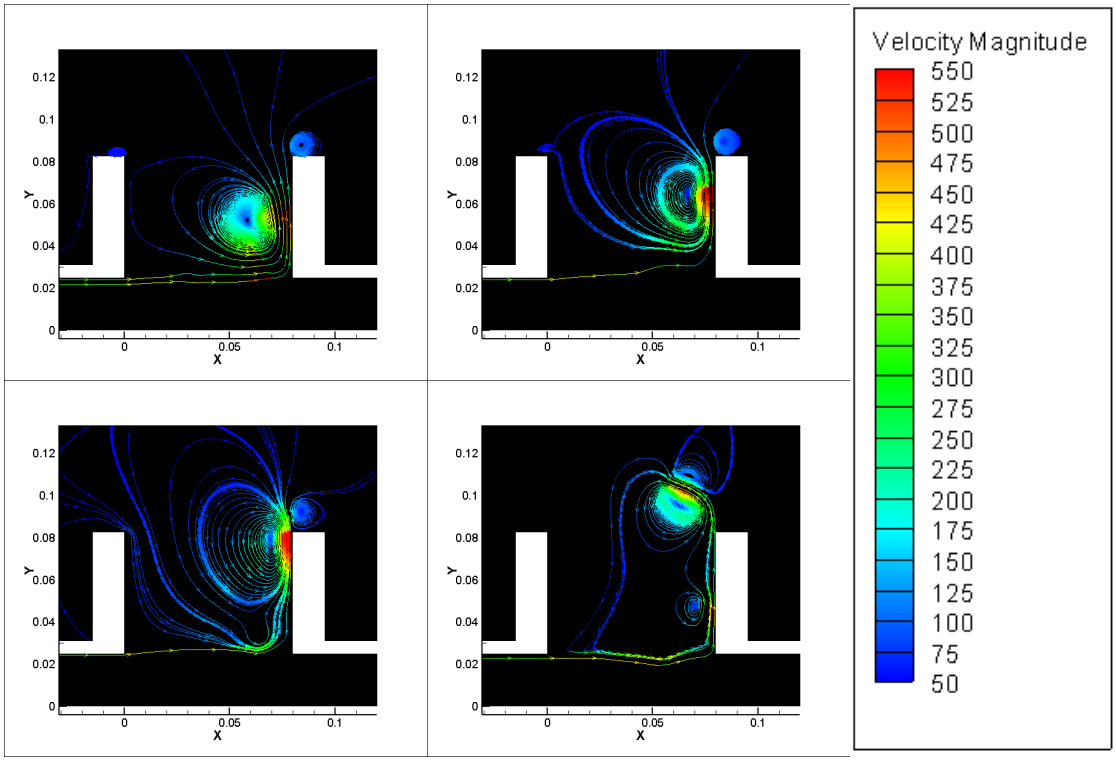


Figure 7.16: CFD velocity plots for a flanged gap of 80mm at Mach 1.45. Images at 0.15ms apart.

8 Discussion

8.1 Pipe gap

8.1.1 Effect of Mach number

The results for a 40mm pipe gap at Mach 1.45 will now be compared with results at the same gap width but at different Mach numbers of 2.2, 1.6 and 1.3.

As the high Mach number of Mach 2.2 could not be tested experimentally, CFD was used to simulate the flow. The flow evolution is shown in Figure 8.1 for a pipe gap of 40mm. As the incident shock enters the gap, the first frame shows that no expansion wave propagates back in the upstream pipe. In addition, there is no reflection off the downstream pipe face of the incident shock wave. Both noticeable behaviours are peculiar to the Mach 2.2 case. For Mach 2.2 the flow exits the upstream pipe at a supersonic speed and hence no waves propagate back in the much stronger flow. The second and third frame show the third peculiar feature for Mach 2.2. The shock system at the downstream pipe, instead of having a normal shock at the inlet to the pipe, the standing shock forms inside the pipe. The standing shock reflects off the axis in the form of a Mach reflection. The fourth frame shows the successive reflections of the standing shock off the downstream pipe wall and the axis.

In addition, Figure 8.2 shows that the jet boundary labelled by *SL* exits the upstream pipe at a relatively larger angle compared with the Mach 1.45 flow. This implies a much larger diameter for the jet. This is as a result of a relatively larger pressure for the supersonic flow at the exit plane of the upstream pipe. One other notable feature from Figure 8.2 is that one end of the developing standing shock is sucked by the primary vortex ring at the at the early stages of flow development.

At Mach 1.6, Figure 8.3 shows the stages of flow development. In the first frame at any early stage of flow evolution, the primary difference from that at Mach 1.45 is that a much stronger jet exits the upstream pipe. As such, the angle of the jet boundary measured clockwise is

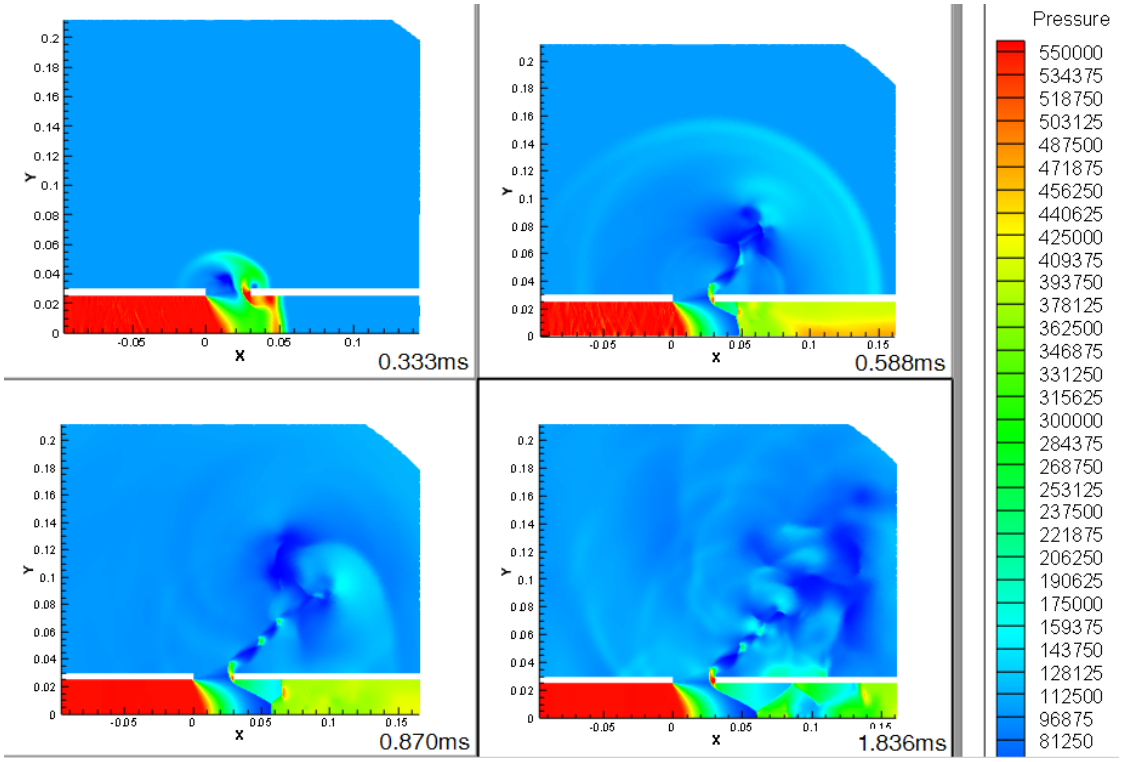


Figure 8.1: Flow development for a pipe gap of 40mm at Mach 2.2

less. The much stronger shock-induced flow at Mach 1.6 results in a jet of larger diameter as the flow expands into the gap, hence the relatively smaller jet angle. The first frame also shows slightly different characteristics of the shocks formed as the jet flow develops. Both the barrel shock and the shock in the plane of the vortex are slightly of greater strength and develop at earlier flow times than for Mach 1.45. This suggests a difference in the nature of the expansion of the high subsonic flow from the upstream pipe. For Mach 1.6, the flow expands to supersonic speeds earlier and much near to the upstream pipe than for Mach 1.45. The barrel shock wave angle is less for Mach 1.6, which again suggests a difference in the nature of the flow expansion in the gap. The angle of the barrel shock is of importance in the development of the jet flow as it determines the nature of reflection of the barrel shock at the axis of the jet. As such the shock system in the jet at steady-state will differ for the two Mach numbers.

The last two frames of Figure 8.3 shows how the flow develops at a much later stage. Precisely they show the development of the standing shock at the inlet to the inlet to the downstream pipe. As the flow approaches steady-state at 0.71ms, a single standing shock forms and controls the downstream pipe flow. In contrast, at Mach 1.45 as the flow approaches steady-state there are multiple shocks at the entrance to the downstream pipe. This can be explained by the fact that, for Mach 1.6 the shocks in the jet upstream of the developing standing shock are much closer to the inlet of the downstream pipe. The shocks within the gap being nearer

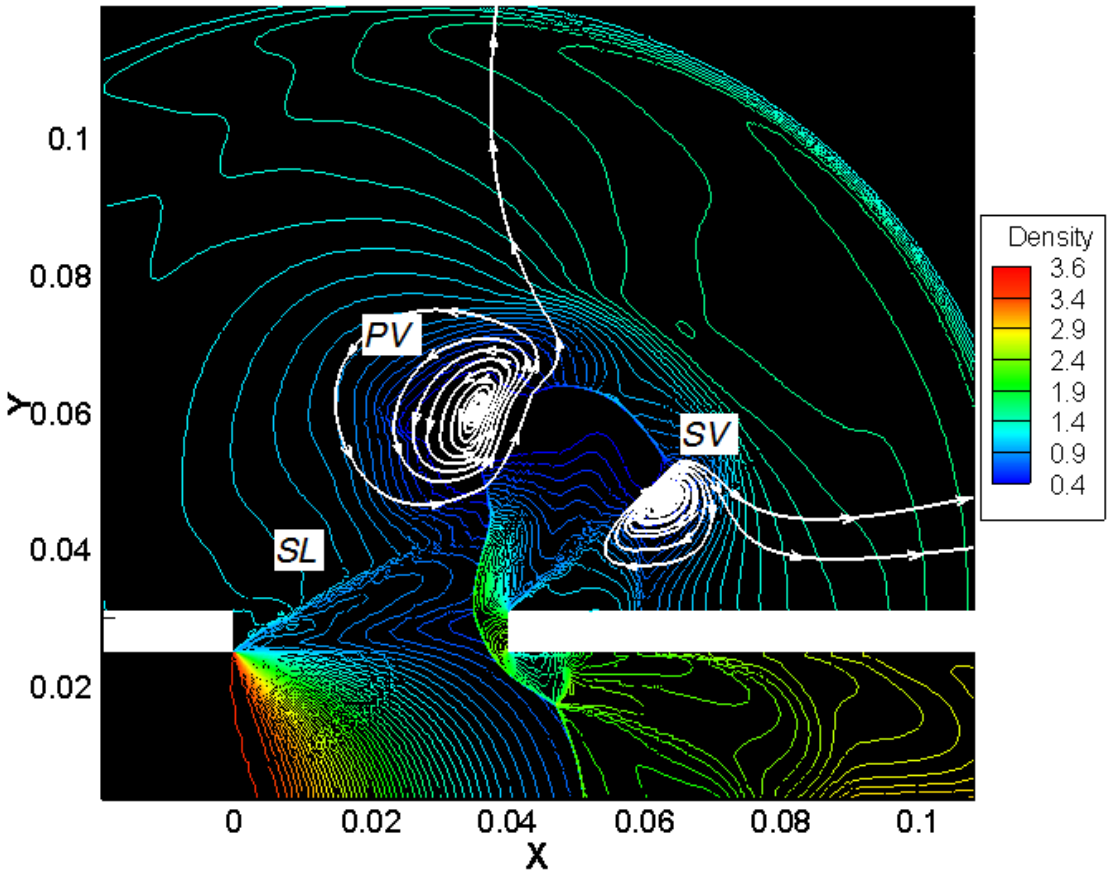


Figure 8.2: 40mm pipe gap at Mach 2.2 flow at early stages. *SL*-Jet boundary, *PV*-Primary vortex ring, *SV*-Second vortex ring.

the downstream pipe will interact with the developing standing shock and form a single standing shock. At Mach 1.45 however, the shocks within the upstream jet are relatively far from the downstream pipe. Therefore as the standing shock develops, there is no interaction between the two sets of shocks into a single shock.

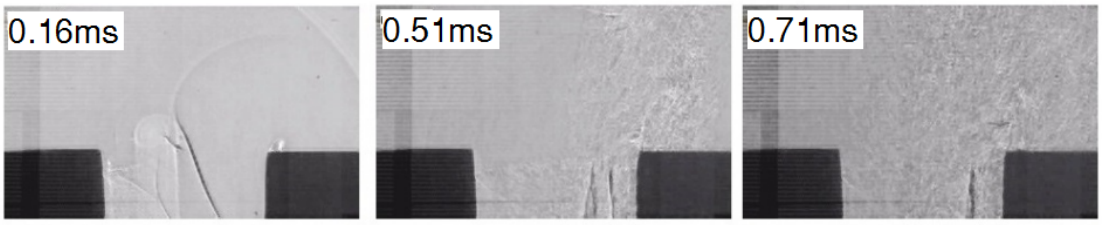


Figure 8.3: Flow development for a pipe gap of 40mm at Mach 1.60

At Mach 1.3 there is marked difference in the development of the flow. Figure 8.4 and Figure 8.5 show noticeable effects for the lower Mach number. The first frame of of Figure 8.4 shows the shock-vortex interaction. Unlike for Mach 1.45 and 1.6, upon interaction with the vortex ring, both portions of the reflected shock are not swept downstream by the vortex ring.

Rather they continue moving upstream. This suggests a relatively weaker shock-induced flow from the upstream pipe. The second frame of Figure 8.4 shows how the flow develops at later times. Instead of a standing shock forming at the inlet to the downstream pipe, weak shocks move upstream into the relatively slowly moving gas to warn it for the presence of the downstream pipe and the adverse pressure gradient. In the flow in the gap, there are no steep density gradients visible. This shows the jet for Mach 1.30 upon exiting the upstream pipe does not attain a supersonic speed.

The behaviour and interaction of the two vortex rings was slightly different for Mach 1.3. For Mach 1.3, the vortex rings are more defined than for higher Mach numbers due to the relatively low particle velocity in the vortex cores. Figure 8.5 shows that the two vortices move adjacently for some time before they leap frogg. Therefore as shown the diameter of the primary vortex ring grows more than for Mach 1.45 before leapfrogging is initiated.

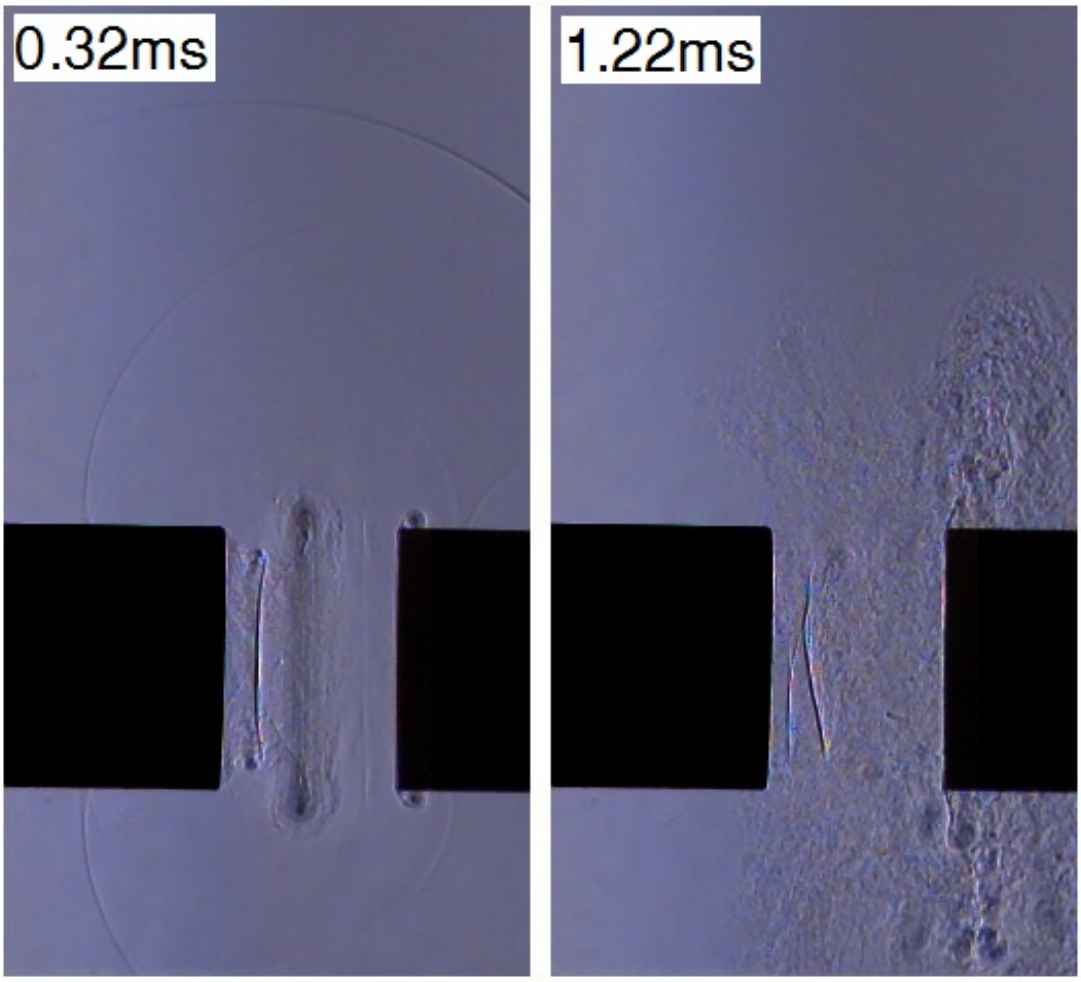


Figure 8.4: Flow development of a 40mm pipe gap at Mach 1.30.

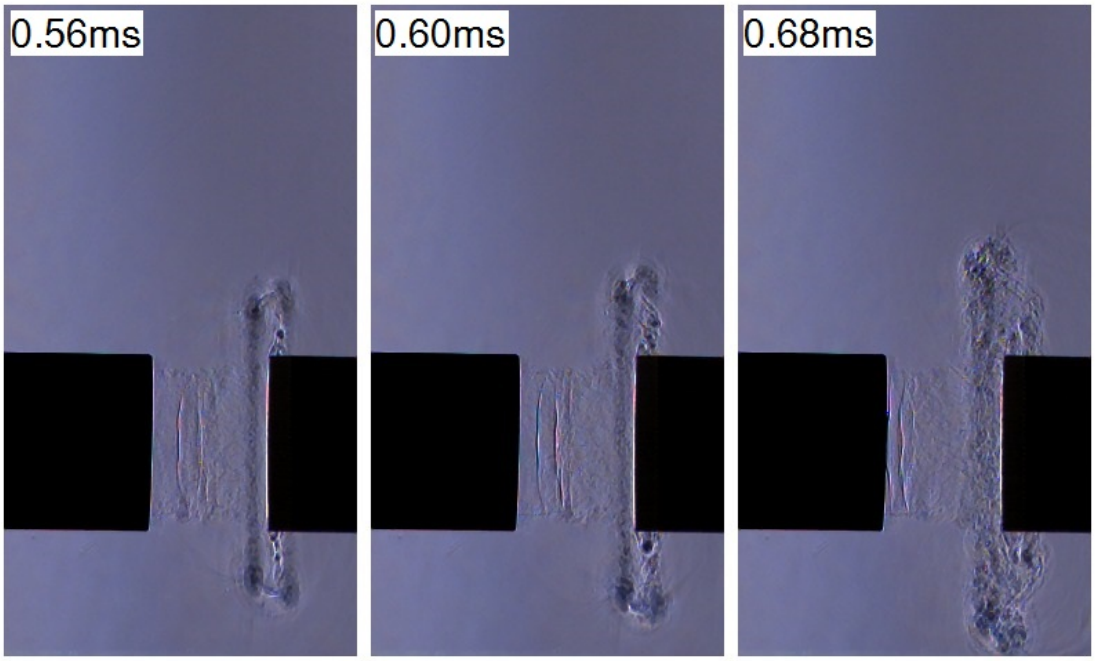


Figure 8.5: Vortex ring interaction for a 40mm pipe gap at Mach 1.3.

8.1.2 Effect of gap width

The effect of increasing the gap width from 40mm to 60mm at Mach 1.6 is shown in Figure 8.6. At small gap widths of 40mm and 50mm in the first and second frame respectively, the standing shock at the inlet to the downstream pipe oscillates in its position. The shock cell and the standing shock merge into a single standing shock. At 60mm, the flow at steady state is slightly different. The distance between the shock cell and the standing shock is relatively large. Though the standing shock oscillate in its position, they do not merge into a single standing shock. The third frame of Figure 8.6 shows this. The effect of gap width at relatively large gap widths of 80mm and 115mm is shown in Figure 8.7. The development of the flow at 80mm is shown for the first two frames whilst for 115mm is shown for the last two frames. The reflected barrel shock off the axis interacts with the developing standing shock at the downstream pipe both for 80mm and 115mm. The flow for 80mm on approaching steady state is similar to the one for 60mm although there is a relatively large gap between the shock cell and the standing shock. At 115mm, the barrel shock reflection off the axis extends outside the gap. Its one end interacts with the core of the primary vortex ring. At a later time step, the distance between the first shock cell and the standing shock for 115mm is much larger than for the smaller gap widths.

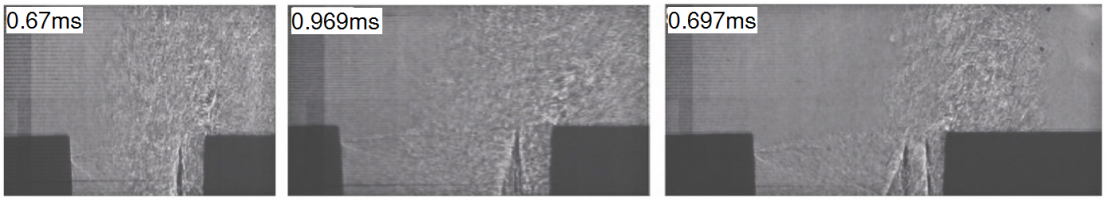


Figure 8.6: Effect of gap width at Mach 1.6. From left to right 40mm, 50mm and 60mm.

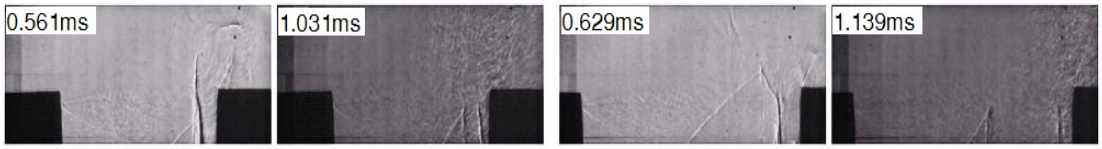


Figure 8.7: Effect of gap width at Mach 1.6. 80mm for the first two frames and 115mm for the last two frames.

8.2 Flange gap

8.2.1 Effect of Mach number

The Mach number effect on the development of flow for a flanged gap is shown in Figure 8.8 and Figure 8.9 for a gap of 50mm. Figure 8.8 shows the development of the flow at the downstream flange surface. The first two frames show the flow at Mach 1.45 and the last two at Mach 1.3. For both Mach 1.3 and Mach 1.45 a primary vortex ring forms due to flow separation at the upstream pipe and a second vortex ring due to flow separation at the downstream flange surface. The behaviour and interaction of the two vortex rings was slightly different for Mach 1.3. The two vortices move adjacently for some time along the flange surface before they leap frog. Therefore as shown the diameter of the primary vortex ring grows more than for Mach 1.45 before the interaction of the vortices is initiated. For Mach 1.45 the interaction of the vortices at the downstream flange surface produces a shock which moves moves upstream. For Mach 1.3 this shock is absent.

Also notable from Figure 8.8 is the absence of a developing standing shock at the inlet to the downstream pipe for Mach 1.3 which is evident for Mach 1.45.

8.2.2 Effect of gap width

The effect of the gap width on the flanged gap flow development is shown in Figure 8.10 for a gap of 50mm and 80mm. The three frames in the first row are for a gap of 50mm and the three in second row are for 80mm. For 50mm there appears to be only two vortex

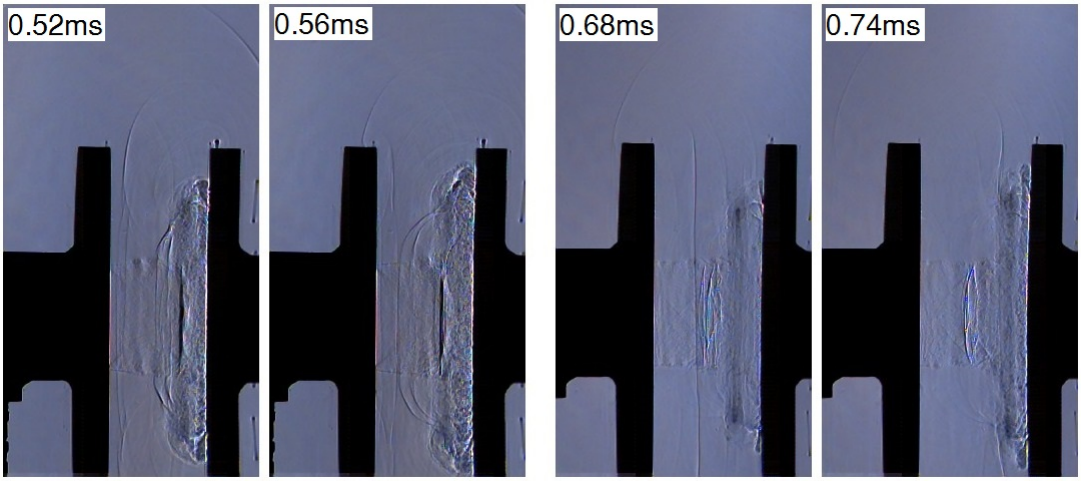


Figure 8.8: Effect of Mach number for a 50mm flanged gap. Mach 1.45 for two images on the left and Mach 1.3 for the latter two.

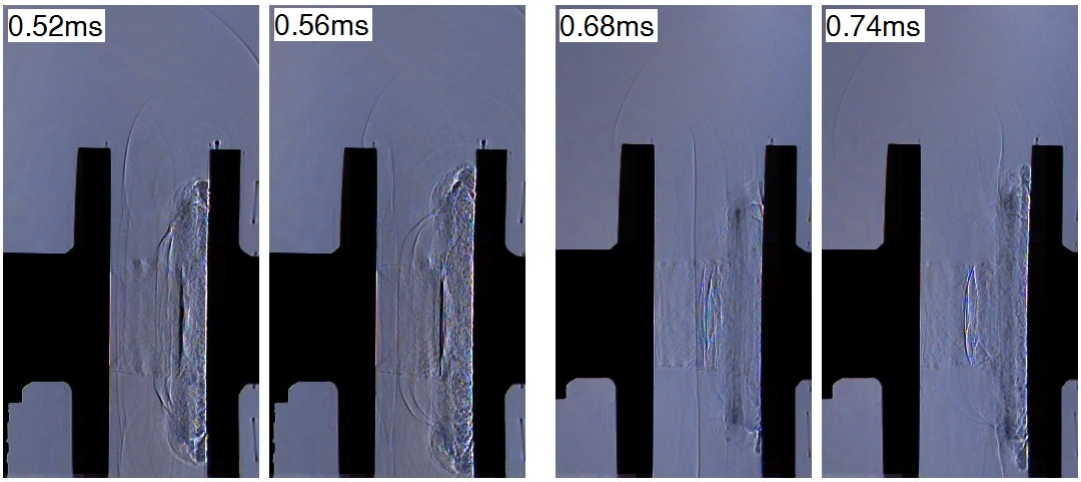


Figure 8.9: Effect of Mach number on shock-vortex interaction for a 50mm flanged gap. Mach 1.45 for the first two images on the left and Mach 1.3 for the last two.

rings that interact along the downstream flange surface. For the 80mm flange gap width, there appears to be three vortex rings that interact along the downstream flange surface. At 80mm, at the downstream flange, in addition to the vortex ring due to flow separation along the flange surface, there is a third additional vortex ring that forms just ahead of the developing standing shock. The forming third vortex ring is best shown for the 0.70ms flow time.

There appears to be more back and forth reflections within the gap for 50mm than for 80mm. As a consequence of the multiple back and forth reflections, Figure 8.11 shows that the flow transitions to turbulence earlier for 50mm than for 80mm.

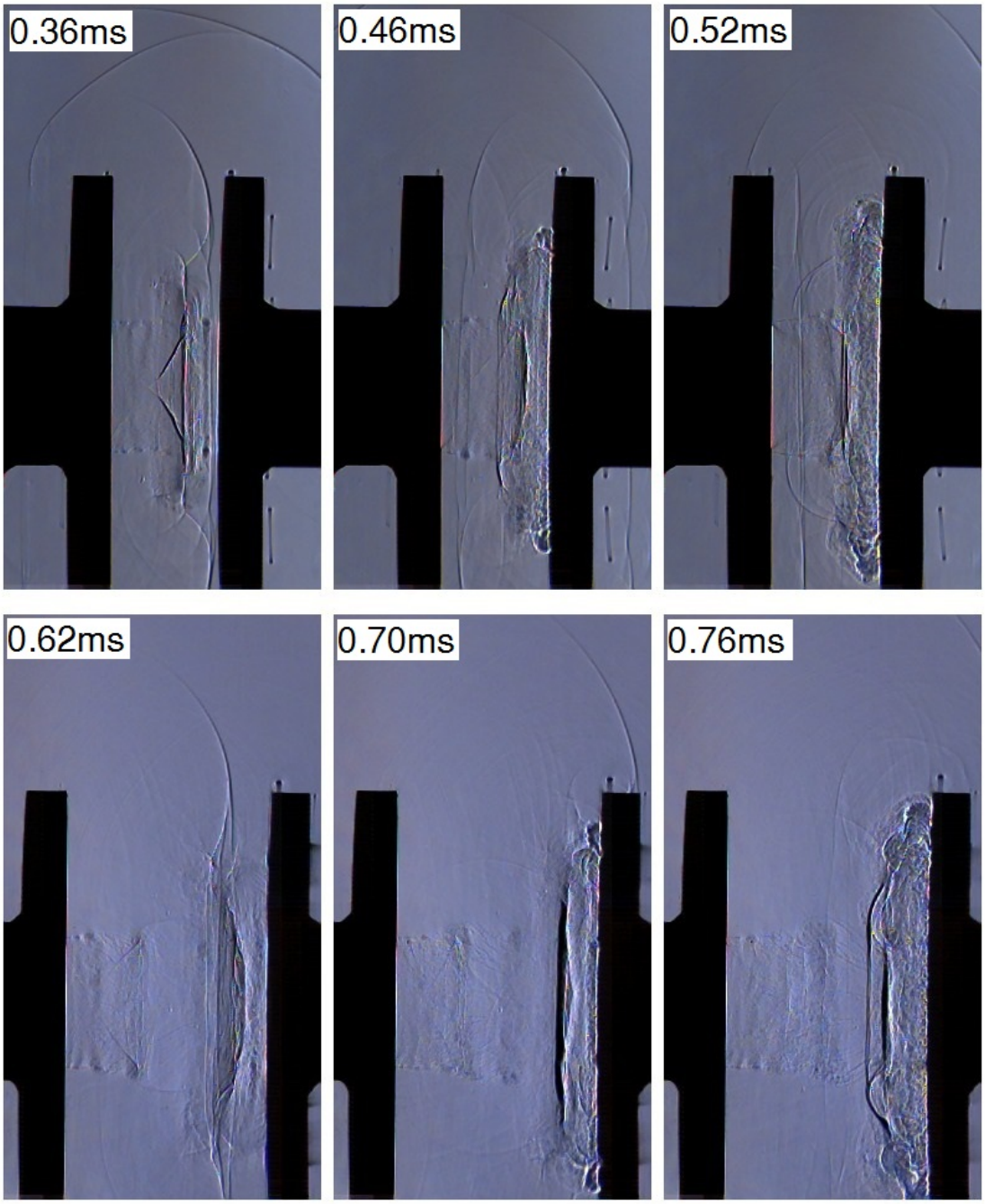


Figure 8.10: Effect of flange gap width. 50mm for images in the first row and 80mm for the images in the second row.

8.3 Comparison of flange gap and pipe gap flow

The general flow for a pipe gap and a flanged gap having been described, the effect of gap geometry is now summarised in this section. The primary difference between the pipe gap flow and the flange gap flow is that the flow is confined for much longer in the latter case.

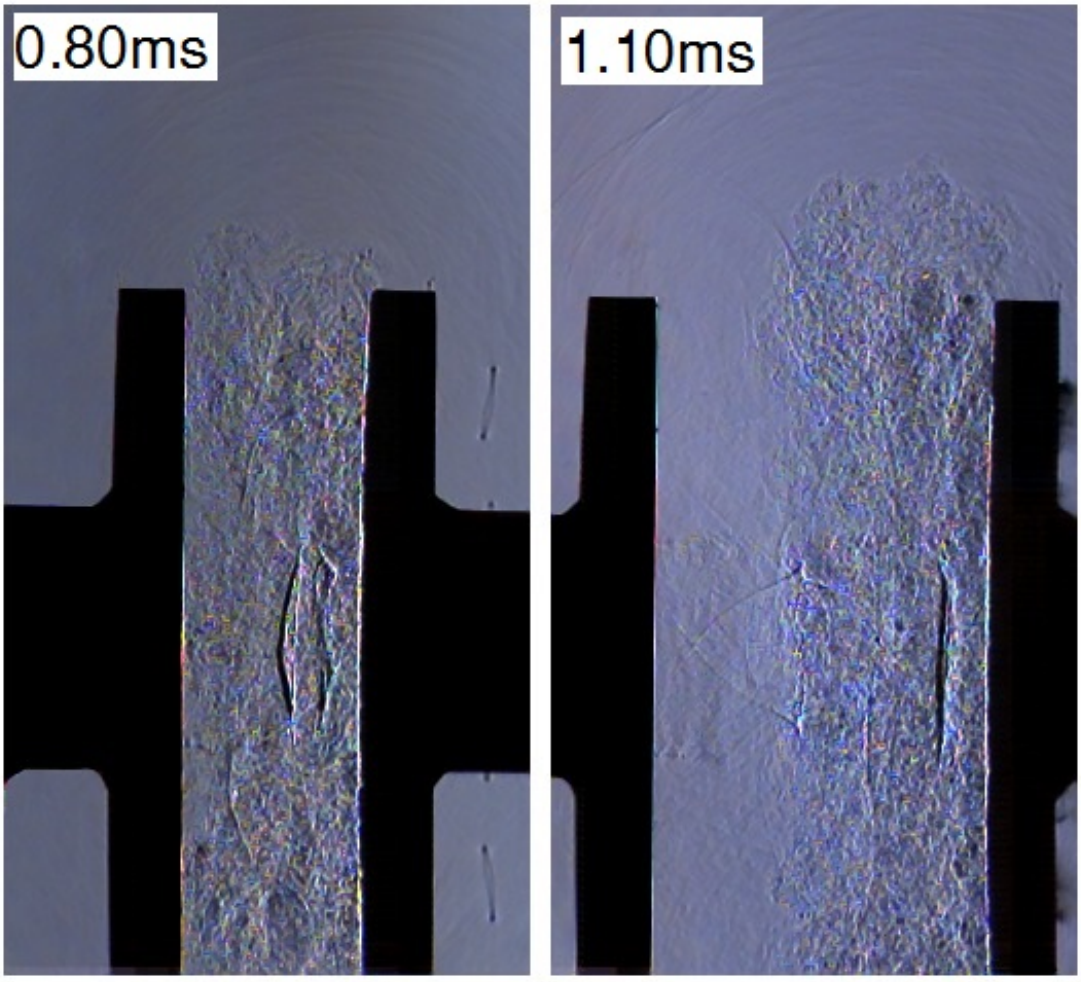


Figure 8.11: Effect of flange gap width on transition to turbulence. 50mm for the image on the left and 80mm for the image on the right. Both cases at Mach 1.45.

Thus, the the flow within the flange gap had a marked difference in flow feature behaviour from the pipe gap case.

8.3.1 Effect on the vortex ring behaviour

Due to the confinement of the flange gap flow, the development of the vortices is mainly influenced by its interaction with the flange surface. The interaction of the vortices takes place along the flange wall and the vortices breakdown as the outward flow propagates along the flange surface. On the contrary the vortex ring development and interaction for a pipe gap occur in the external flow field. The nature of the interaction of the vortices is mainly influenced by the velocity field in the external flow emerging from the gap. One consequence of the difference in the vortex ring behaviour is that the flow transitions to turbulence earlier in the flanged gap case than for the pipe gap case.

The nature of the shock-vortex interaction is also slightly different for the flanged gap. The re-reflected shock from the upstream flange face catches up and interacts with the primary vortex ring. In this case both the shock and the primary vortex ring are propagating downstream. Unlike for the shock-vortex interaction dominant for the pipe gap, this type of flange gap shock-vortex interaction is unique. The two forms are shown in Figure 8.12 for a 80mm flanged gap and 80mm pipe gap respectively. For the flange gap case, a certain portion of the shock is curved with its one end sucked in the vortex core after the interaction.

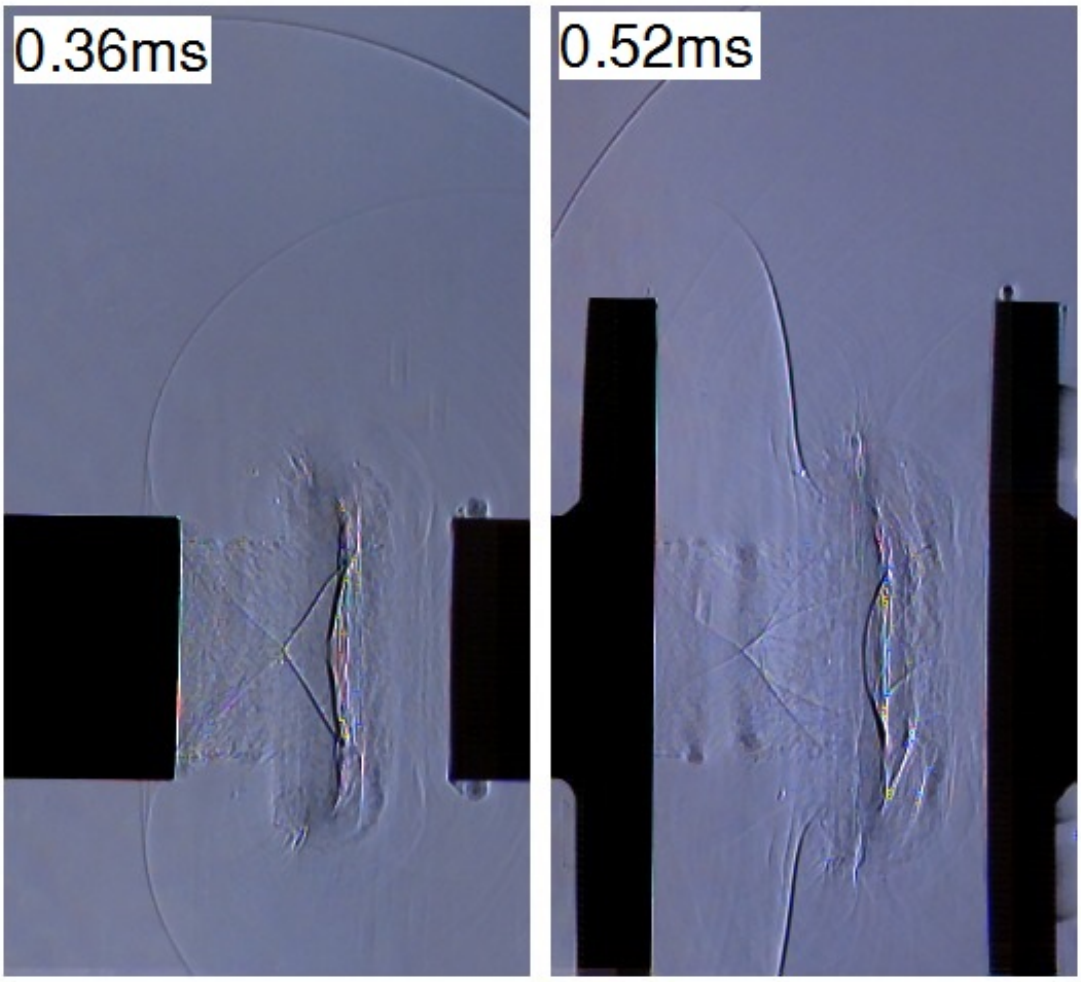


Figure 8.12: Effect of gap geometry on shock-vortex interaction. 80mm pipe-gap on the left and 80mm flanged gap on the right. Both cases at Mach 1.45.

8.3.2 Effect on the jet structure

The jet structure in the vicinity of the downstream flange approaches that of a supersonic jet impinging on a flat plat. The jet interacts with the walls of the downstream flange. The flow field in the vicinity of the downstream flange is highly unsteady. The standing shock system is complex. Although oscillations in the standing shock were noticed for the pipe gap

case, it appears that for the flange gap the oscillations are greater. Figure 8.13 compares the standing shock system for the flange gap and pipe gap. The strong oscillations in the standing shock for the flanged case indicate a very strong acoustic field.

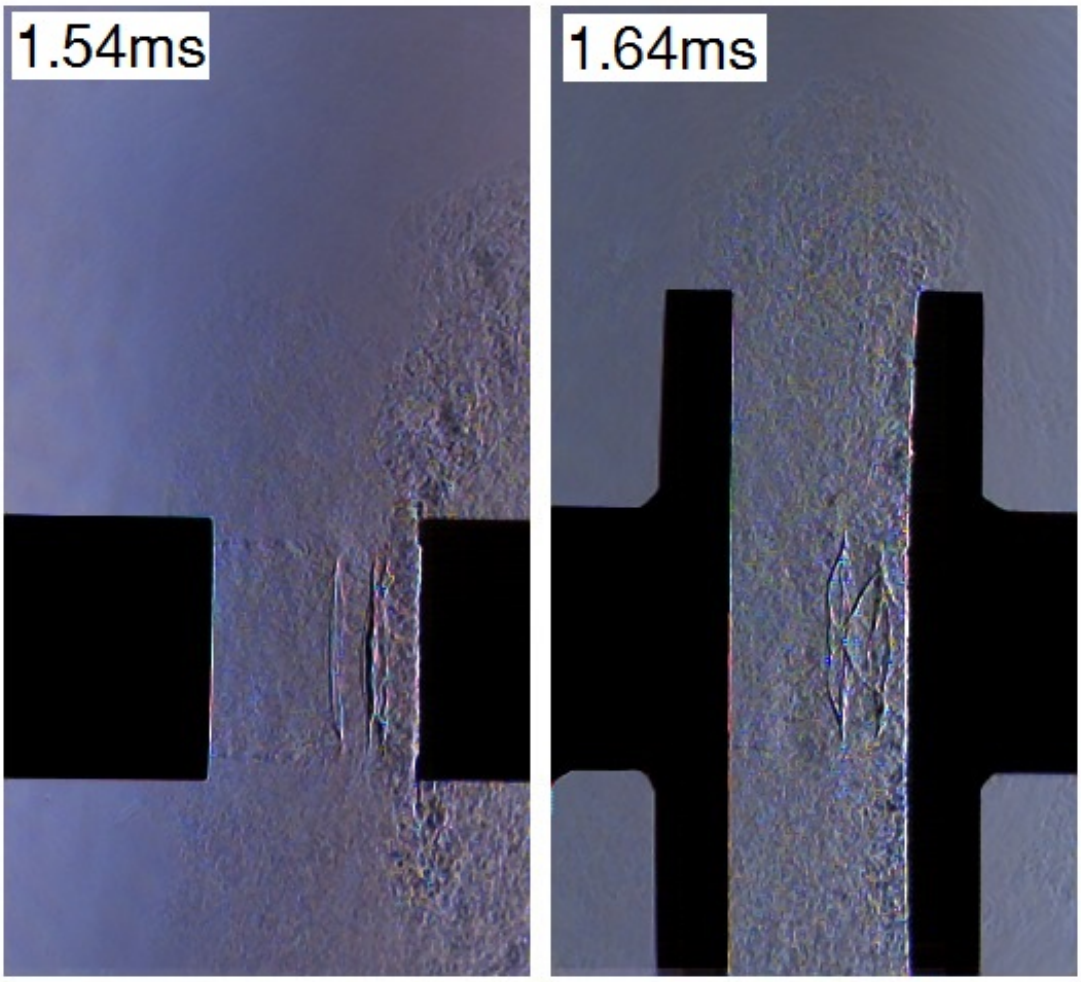


Figure 8.13: Effect of gap geometry on standing shock structure. 40mm pipe-gap on the left and 40mm flanged gap on the right. Both cases at Mach 1.45.

For the flange gap, multiple vortex rings are present in the jet emerging from the upstream pipe. This indicates a highly perturbed shear layer from the upstream pipe. The multiple reflections and re-reflections is a possible source of perturbations in the jet as it emerges from the upstream pipe.

Comparing with the pipe gap case, the jet boundary in the flanged gap was highly irregular. This indicates the multiple reflections and re-reflections lead to stronger and sustained shock-shear layer interaction. This leads to the jet shear layer instability and the eventual break-up.

8.4 Gap Flow Features

The general behaviour of the shock induced flow in the pipe gap having been established, detailed analysis of behaviour of the flow features will now be given. These are the features present in the pertubed region behind the incident shock entering the gap.

8.4.1 Standing Shock

Once developed, the standing shock was observed to oscillate in its position for Mach 1.45. For the lower Mach of 1.3, multiple shocks moved upstream to warn the flow of the presence of the downstream pipe. From section 7.4 it was noted that after the development of the standing shock, there were pressure oscillations in the downstream pipe. It was suggested that the behaviour of the standing shock and the multiple shocks was related to the downstream pressure oscillations. In essence the pressure oscillations were a response to the shock oscillations within the gap. To validate the suggestion, downstream experimental pressure profiles for Mach 1.45 and Mach 1.3 are shown on the left frame of Figure 8.14 and their corresponding shadowgraphs are shown in on the right frame of Figure 8.14. The shadowgraphy for Mach 1.45 shows the positions of the oscillating standing shock at different times by the dashed red lines. For Mach 1.45, the shadowgraphy shows that the shock oscillations are slight and the shock fairly stays in one position and hence a fairly constant downstream pressure in the corresponding pressure time profile. For Mach 1.3 however, shocks are continually formed and these move upstream perturbing the flow entering the downstream pipe, and hence the more pronounced pressure oscillations in the corresponding pressure time profile.

This shows that the downstream pipe flow is hugely influenced by the existence and behaviour of the shock wave system within the gap.

8.4.2 Second Shock

As the incident shock diffracted around the upstream pipe, a shock was observed to form in the plane of the ensuing primary vortex ring. This will be termed the second shock. The threshold incident shock wave Mach number at which the second shock formed was found to be 1.45. For the lower Mach number of 1.3, the perturbation created by the diffracting incident shock is so weak that a vortex pair without an embedded second shock is seen at the exit. Takayama and Sun[14] explained the existence of the second shock due to the existence of a locally supersonic flow behind the diffracting shock wave. Behind the diffracting incident shock, simple expansion waves travelling upstream accelerated the high subsonic flow

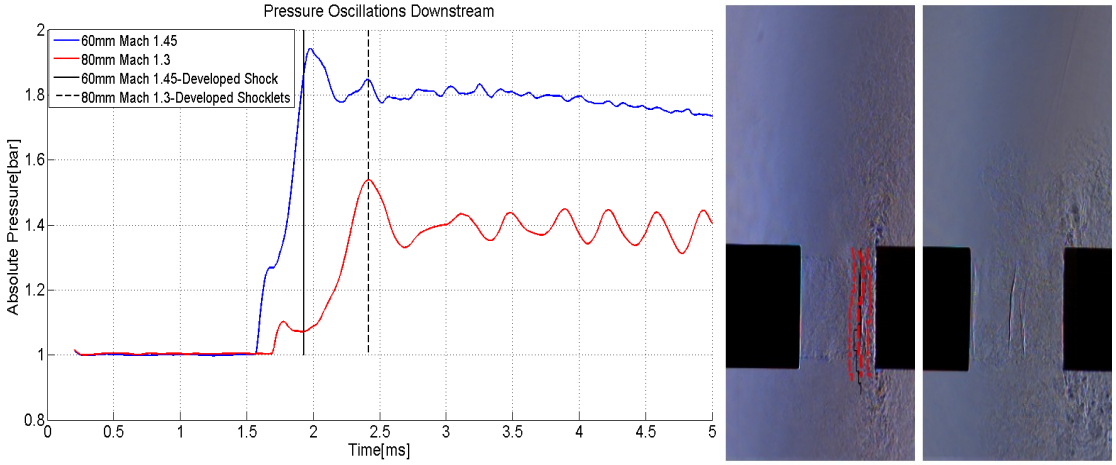


Figure 8.14: Downstream pressure profiles on the left. Shadowgraphs on the right for 40mm pipe gap at Mach1.45 and Mach 1.30 respectively.

which eventually became locally supersonic. If the second shock wave pattern is induced by the primary vortex ring, it was found more reasonable to analyse the second shock as a recompression shock in the primary vortex ring frame of reference. Due to the presence of the vortex ring the supersonic flow faces an adverse pressure gradient forming the second shock. Figure 8.15 shows a CFD velocity plot and shadowgraphy for a 40mm gap width at Mach 1.6. It shows the locally developed supersonic flow in the gap and the second shock formed in the plane of the primary vortex ring.

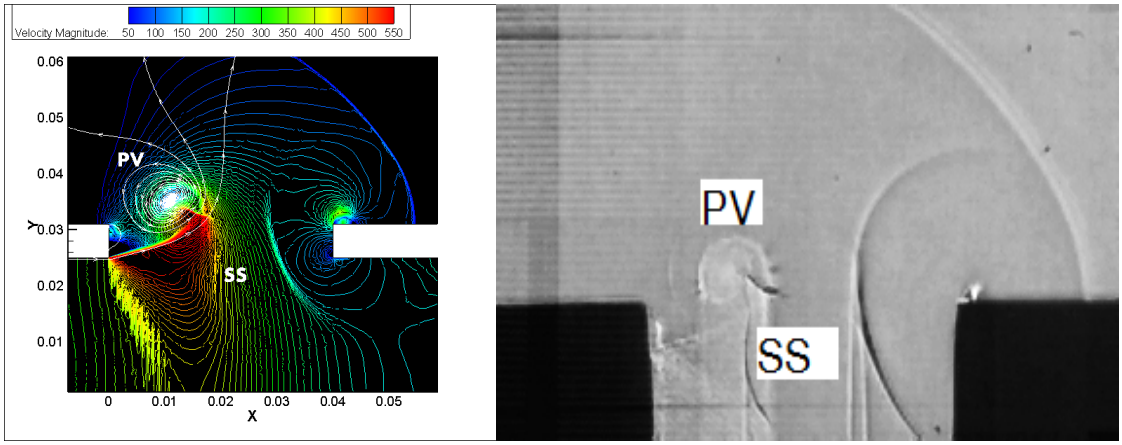


Figure 8.15: Formation of a second shock for 40mm Mach 1.6. CFD velocity plot on the left and shadowgraph on the right. PV-primary vortex ring, SS-second shock.

8.4.3 Barrel Shock

The possible reasons for the formation of barrel shocks were outlined in subsubsection 2.5.1.1. A barrel shock had to form downstream of the Mach lines of the expansion fan issuing out

from the lip of the upstream pipe. The intercepting shock was formed for Mach 1.45 and Mach 1.6. The existence of the Mach lines of the expansion fan and the barrel shock are best shown by the CFD density plot in Figure 8.16 for 80mm gap at Mach 1.6.

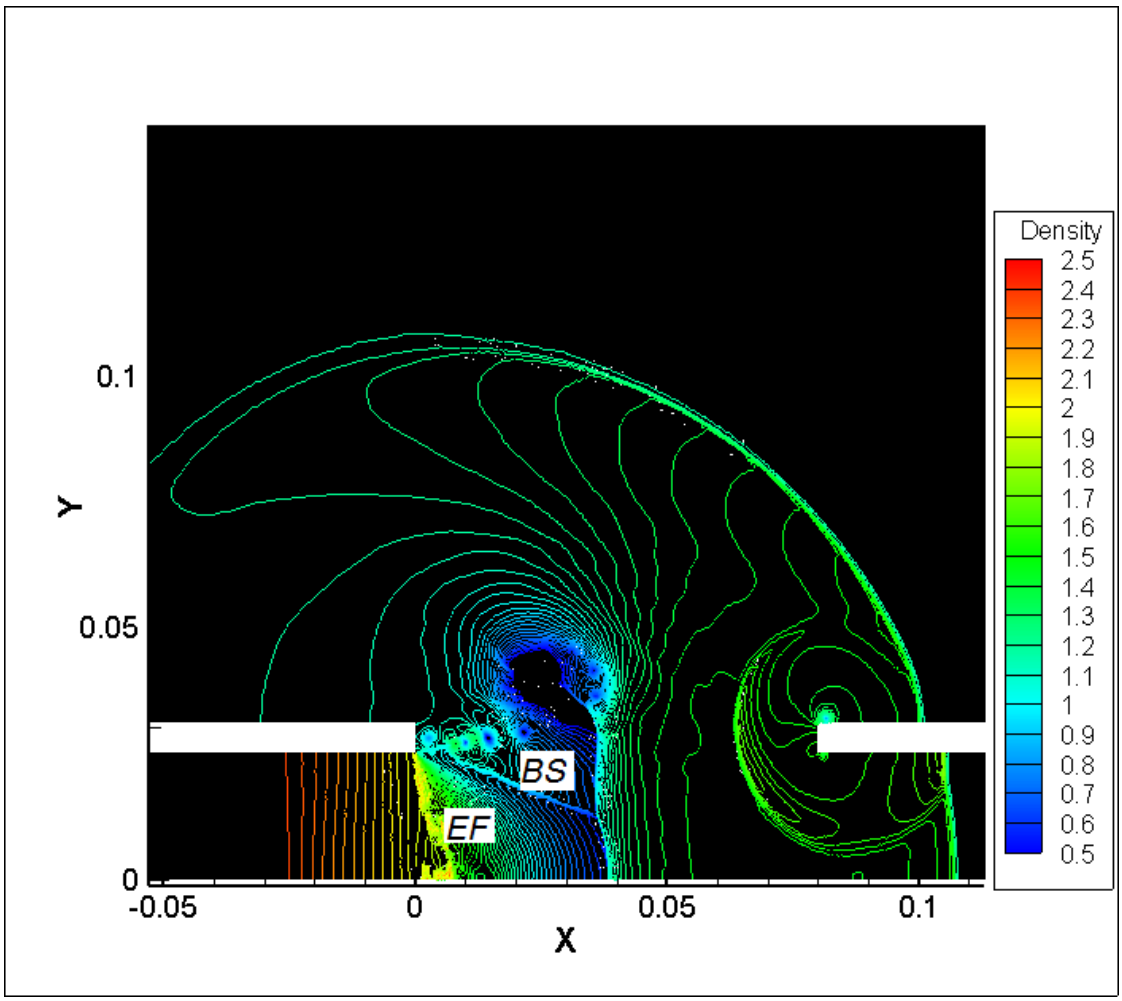


Figure 8.16: CFD density plot showing formation of a barrel shock for 80mm Mach 1.6. *BS*-Barrel shock, *EF*-Expansion fan.

One end of the barrel shock interacts with the second shock. The second shock is clearly bent from this interaction.

The effect of the Mach number on the nature of the barrel shock was investigated. The angle the barrel shock makes with the flow axis was investigated with change in the Mach number. As shown in Figure 8.17, on decreasing the Mach number from 1.6 to 1.45 the angle at which the barrel shock makes increases. The different angles of the incident barrel shock will result in different angles of its reflected component off the flow axis.

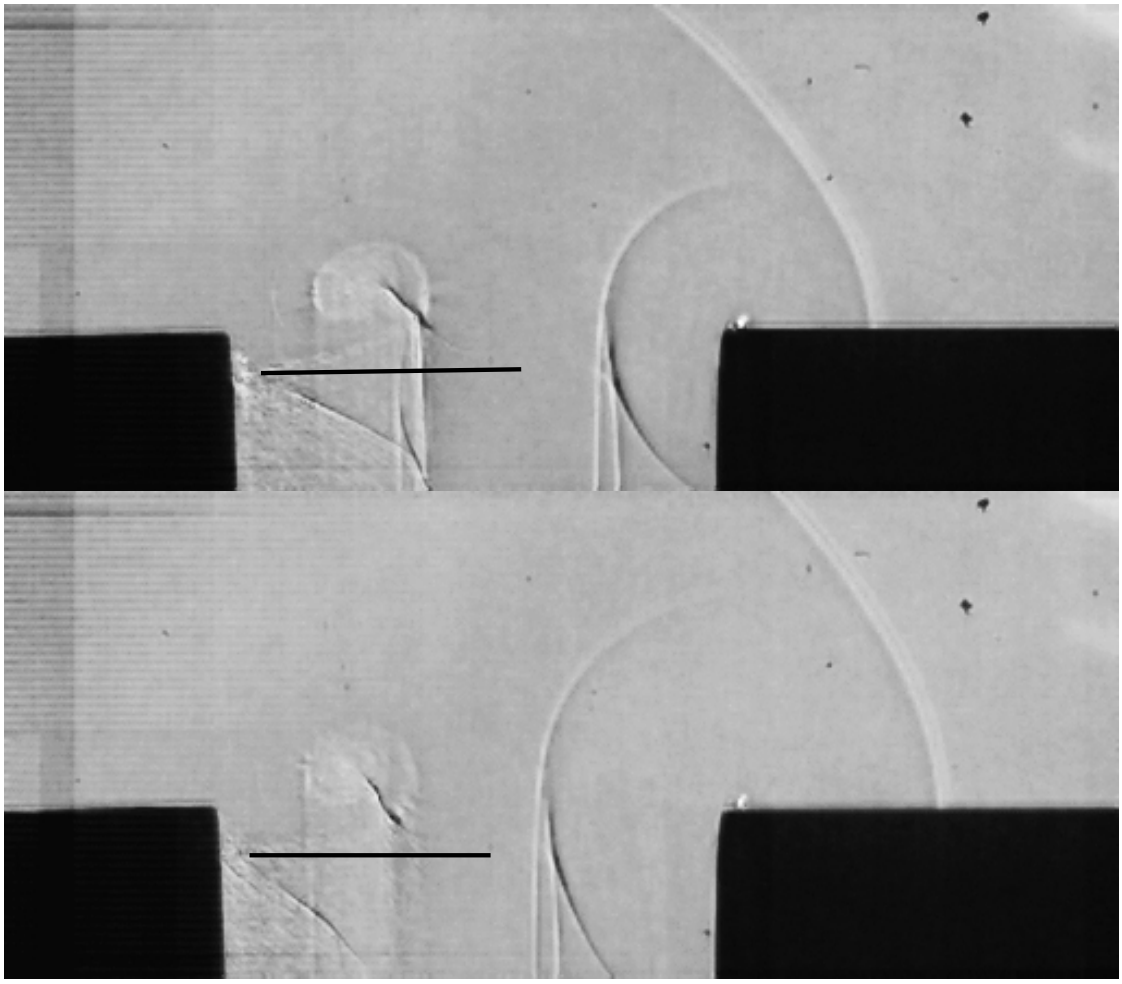


Figure 8.17: Variation of Barrel shock angle with Mach number. Image for 60mm Mach 1.6 on top and 60mm Mach 1.45 on the bottom.

8.5 Flow feature Interactions

8.5.1 Shock-vortex interactions

The returning reflected shock from the downstream pipe strikes and interacts with the vortex ring. The reflected shock front is distorted by the interaction. This was noticed to be influenced by the flow shock Mach number. At Mach 1.6, the upper and lower portions of the returning reflected shock distort differently. The upper part of the shock front diffracts around the vortex and accelerates in the upstream direction. The lower part of the shock is swept downstream due to the strong flow in the downstream direction through the inner portion of the ring. In addition the lower portion interacts with the second shock and the two merge into a single shock wave and propagate downstream.

At lower Mach number of 1.3, both the upper and lower portions of the reflected shock continue in the upstream direction after the interaction with the vortex. The upper portion still diffracts and is bent as it passes the vortex. The propagation back upstream is due to relatively slow speed of the jet behind the initial incident shock wave.

8.5.2 Vortex ring leapfrogging

It has already been outlined that for all gap widths and shock Mach numbers, the primary and second vortex rings interact by leapfrogging over each other. The vortex leapfrog is shown in Figure 8.18 by CFD velocity plots with streamlines for a 80mm pipe gap at Mach 1.6. The streamlines are coloured by velocity magnitude. The second weaker vortex ring is shown to roll over the relatively stronger primary vortex ring. Flow discontinuities that develop as the primary and second vortex ring interact are shown in Figure 8.19. Firstly, the CFD velocity plots show that there exists an embedded shock between the vortex centres as they propagate adjacently. There is evidence of the flow in between the vortex centres reaching supersonic speeds. The second discontinuity is the separation line attached to the second vortex ring. As shown in the plot, the separation line attaches the second vortex ring to the point where the flow separates from the downstream pipe.

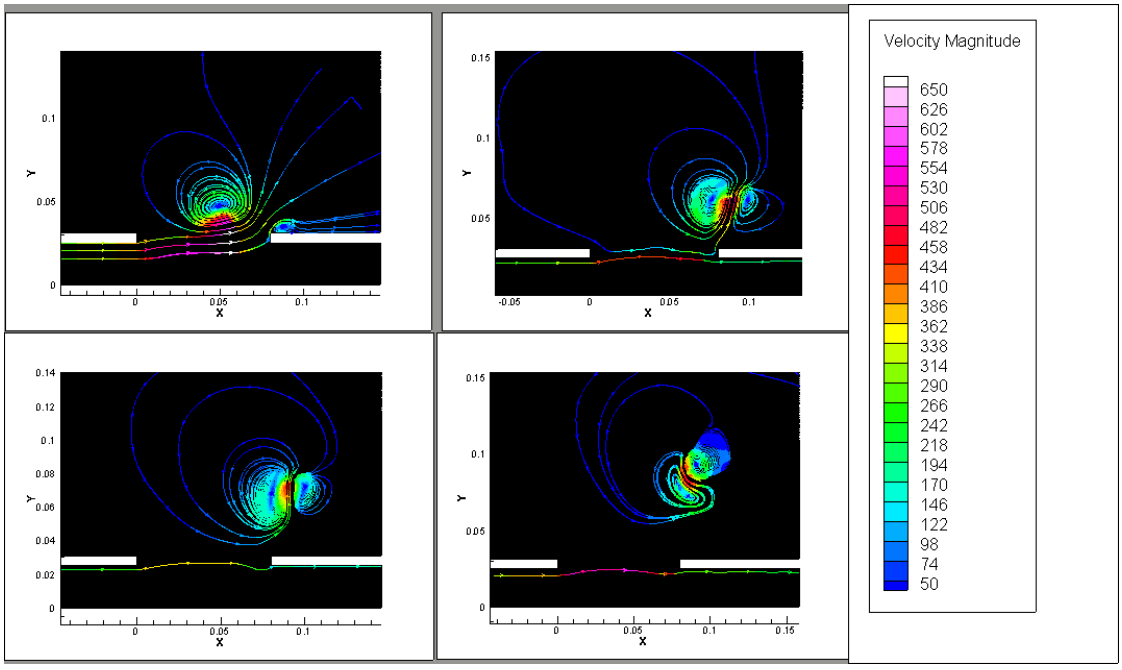


Figure 8.18: CFD velocity plots for 80mm pipe gap Mach 1.6 showing vortex ring leapfrogging process.

The another noticeable feature in the interaction of the vortices is shown by the shadowgraphs in Figure 8.20. As the vortex leapfrogging is initiated in the first frame, a toroidal shock is

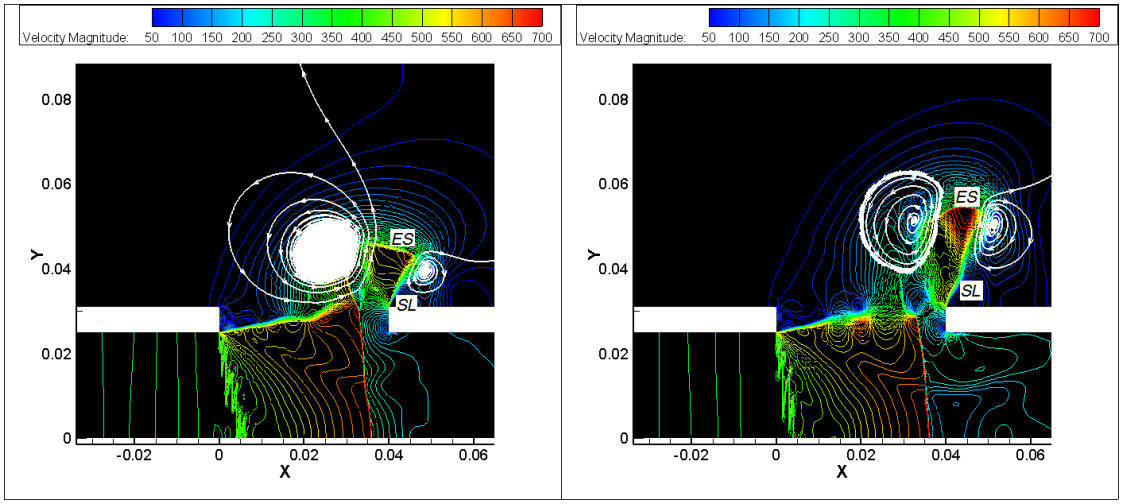


Figure 8.19: CFD velocity plots for 40mm pipe gap Mach 1.6. *SL*-Separation line, *ES*-Embedded shock. Images at 0.07ms apart

produced. The toroidal shock origin was suggested to be the high pressure region produced from the leapfrog. The second frame shows the toroidal shock propagating in the upstream direction. In doing so it then produces another flow-feature interaction. The toroidal shock then interacts with the shear layer of the jet issuing from the upstream pipe. The disturbance induced by the toroidal shock causes instability of the shear layer. Although the exact interaction is not clear, the shear layer is clearly distorted.

A corresponding three-dimensional simulation was done to investigate how exactly the vortex rings evolve as the flow develops. To visualise the vortex ring evolution, six sequential three-dimensional displays of iso-vorticity surfaces for both rings are shown in Figure 8.21. As both the primary and second vortex rings develop, the diameter of the iso-vorticity surfaces increases. The diameter increases axisymmetrically which suggests uniform flow expansion from the circular pipe. At later stages, the phenomena of vortex leapfrogging is clearly shown in these three-dimensional vorticity iso-surfaces.

8.6 Extended geometry simulation

As has been outlined before, pipe separation following an explosive event can occur at any weak point in the piping structure. In addition to failure at gap geometries discussed in this chapter, separation can occur at bolted, welded and screwed joints. In practice, a pipe separation at a pipe gap can also take the form of a curved geometry simulating a 'pipe burst'. This chapter will therefore extend the study to these additional gap geometries that can result from pipe separation at different points in the pipeline.

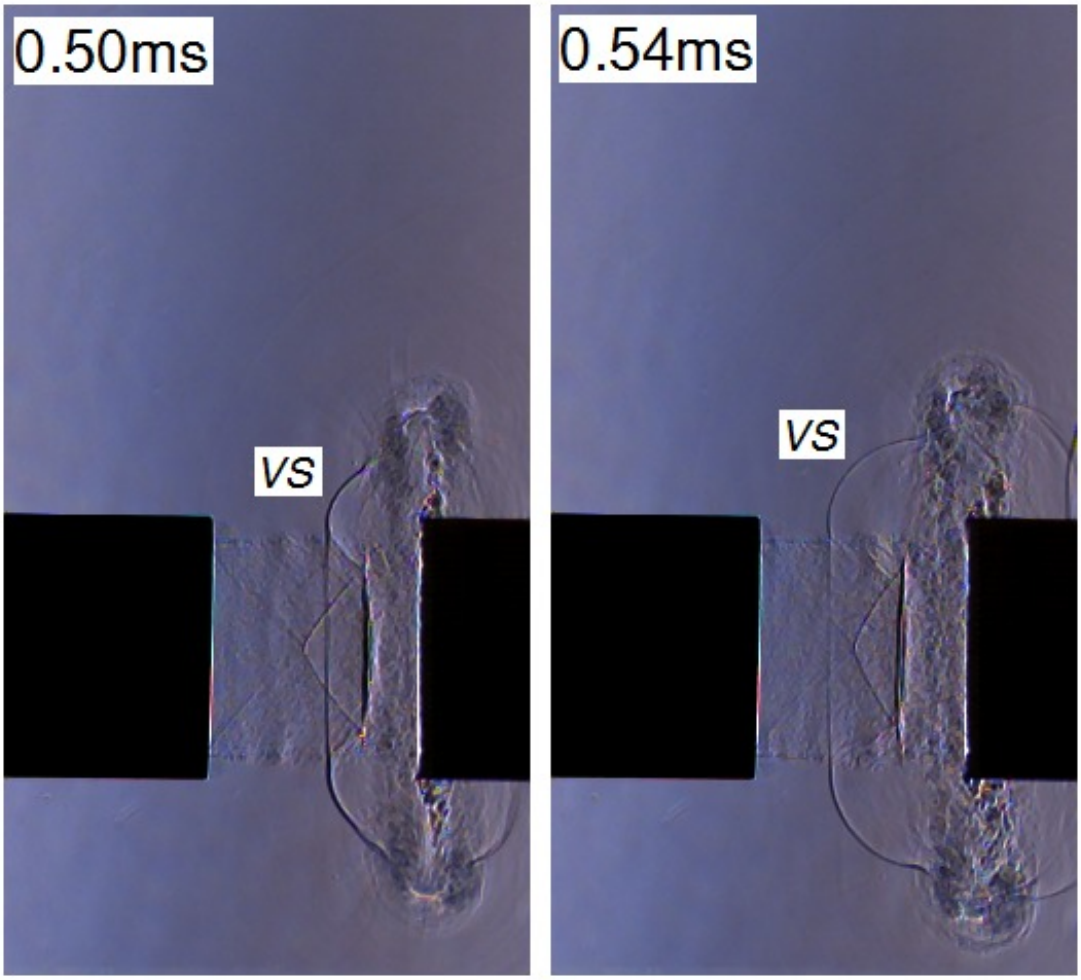


Figure 8.20: Shadowgraphs for 40mm pipe gap at Mach 1.45. *VS*-Toroidal shock.

As the flow through these geometries were difficult to simulate experimentally, the validated CFD methodology was used.

8.6.1 Burst Pipe Simulation

8.6.1.1 Development of the flow

The development of the flow for a burst pipe is shown in Figure 8.22 for a 30mm gap at Mach 1.6. In the first frame, the incident shock diffracts around the upstream burst pipe. On striking the downstream pipe, the incident shock reflects off the curved portion of the burst downstream pipe in the second frame. At the same time, an expansion fan forms at the lip of the non-curved portion of the upstream pipe. Downstream of the expansion fan, the flow expands and accelerates into the curved portion of the upstream pipe. Early stages of development of a shock in the plane passing through the middle of the gap is shown in the

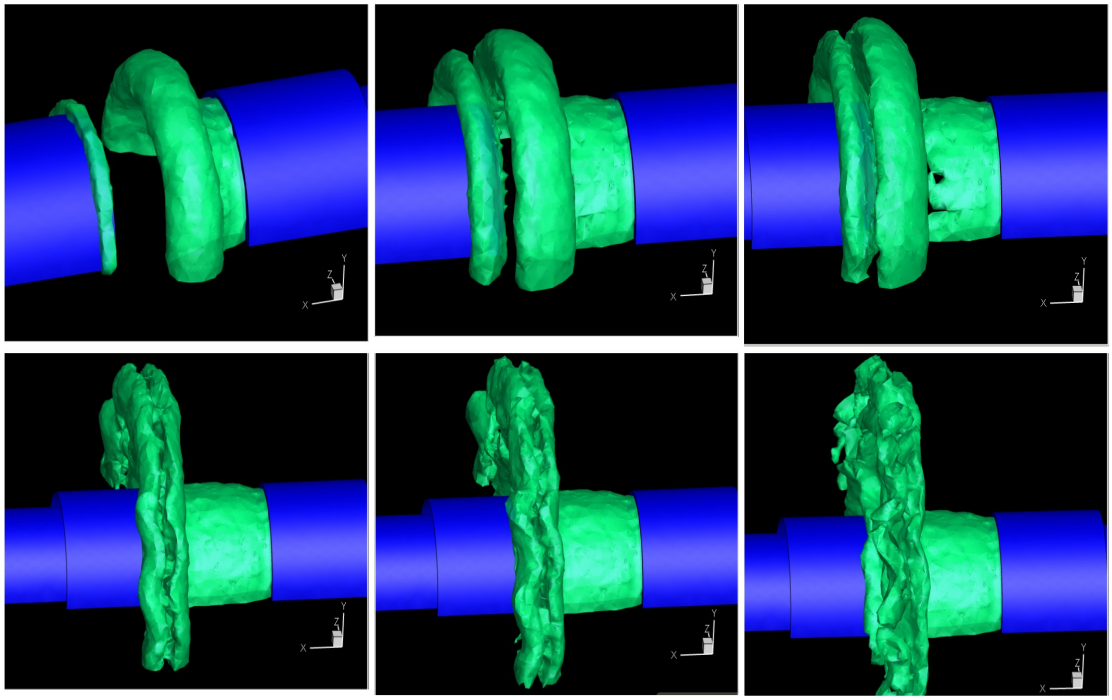


Figure 8.21: Iso-vorticity surfaces for primary and secondary vortex ring. Images taken at 0.20ms apart.

fourth frame. In the downstream pipe, the reflection of the incident shock transitions from a regular to a Mach reflection. The two portions of the reflected shocks from the upper and lower wall approach the flow axis. In the fifth frame, the expanded flow separates at the walls of the upstream pipe. Shock focusing of the reflected components occurs at the flow axis. In the last frame, vortices emanate from the separation points at the wall. Shocks reflected from downstream pipe and shocks from shock-focusing all interact with the flow emerging from the upstream pipe.

The developed shocks in the burst pipe gap are now shown in Figure 8.23. A lamba configuration is noted. One branch of the shock is oblique and originates at the point of separation in the upstream pipe. The other branch is the shock in the core of the jet and lies in the plane that passes through the middle of the gap.

8.6.1.2 Shock structure

The occurence of the lambda configuration of the shock system will now be briefly outlined. Figure 8.24 shows the velocity plot at the lip of the upstream pipe. The two branches of the lambda configuration already outlined in subsubsection 8.6.1.1 are shown by *L1* and *L2*. The *L1* branch originates at a certain point along the curved portion of the upstream pipe. The overexpanded supersonic jet remains attached to the wall up to this point and then separates.

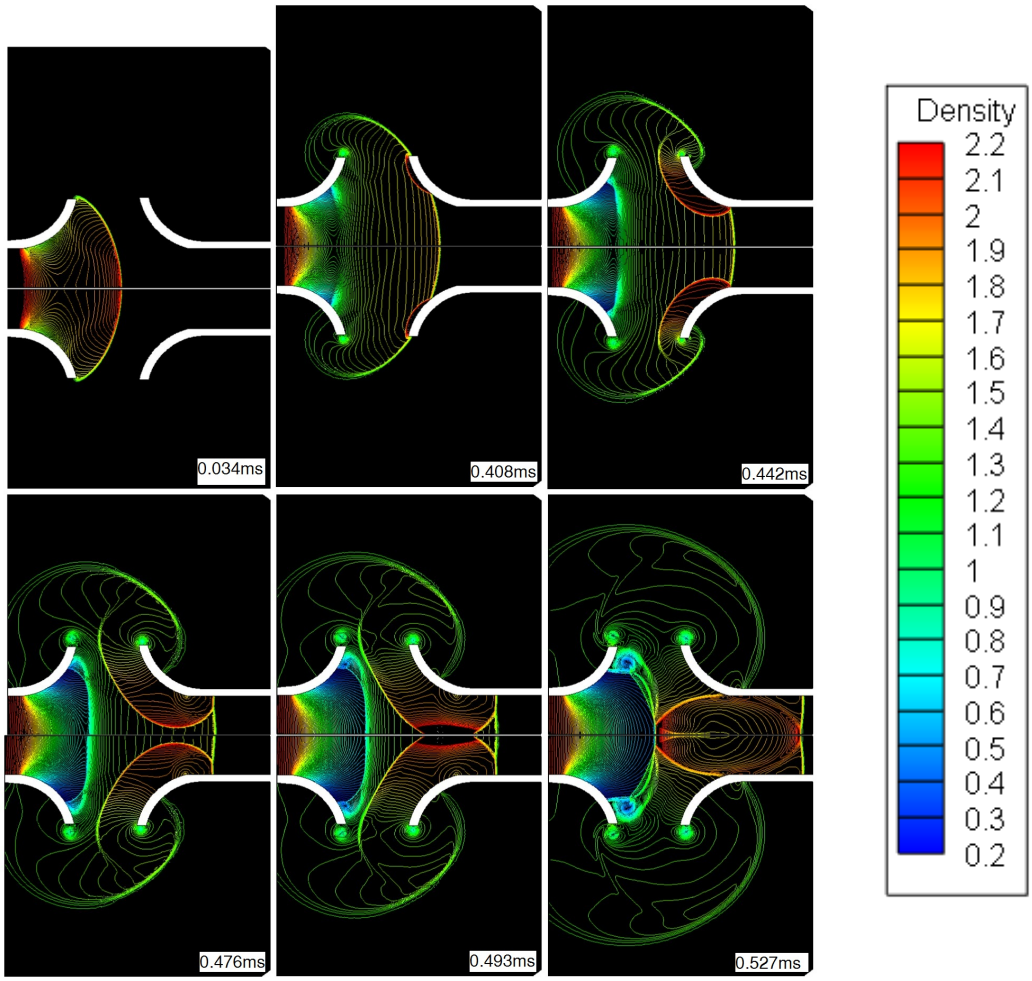


Figure 8.22: CFD density plot showing flow development for a 30mm gap burst pipe at Mach 1.6

The streamlines show the separation and the recirculation region(PV) after the separation point. A slipstream separates the separated flow and the almost stagnant gas above the slipstream.

The point of separation appears to the oncoming supersonic flow as a concave corner and hence the shock *L1* forms. The supersonic overexpanded jet passing through the core faces an adverse pressure gradient due to the presence of the downstream pipe, and therefore the *L2* branch forms roughly in the middle of the gap.

In addition to the two branches there appears to be another shock labelled *L3*. The additional shock merges with the *L1* and *L2* shocks to form a triple point. A slip line originates from the triple point.

The structure of the shock for the burst pipe gap shows noticeable differences with the ordinary pipe gap. As the flow emerges from the burst pipe, it expands into an overexpanded

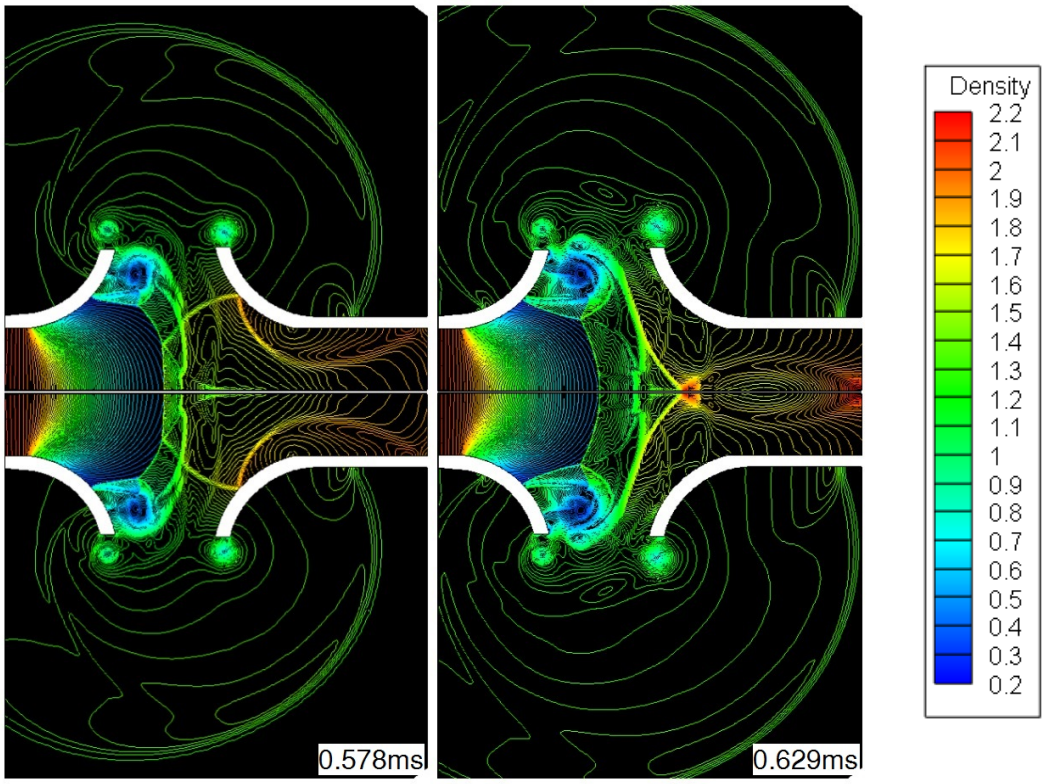


Figure 8.23: Developed shock system at later times for a 30mm burst pipe gap at Mach 1.6.

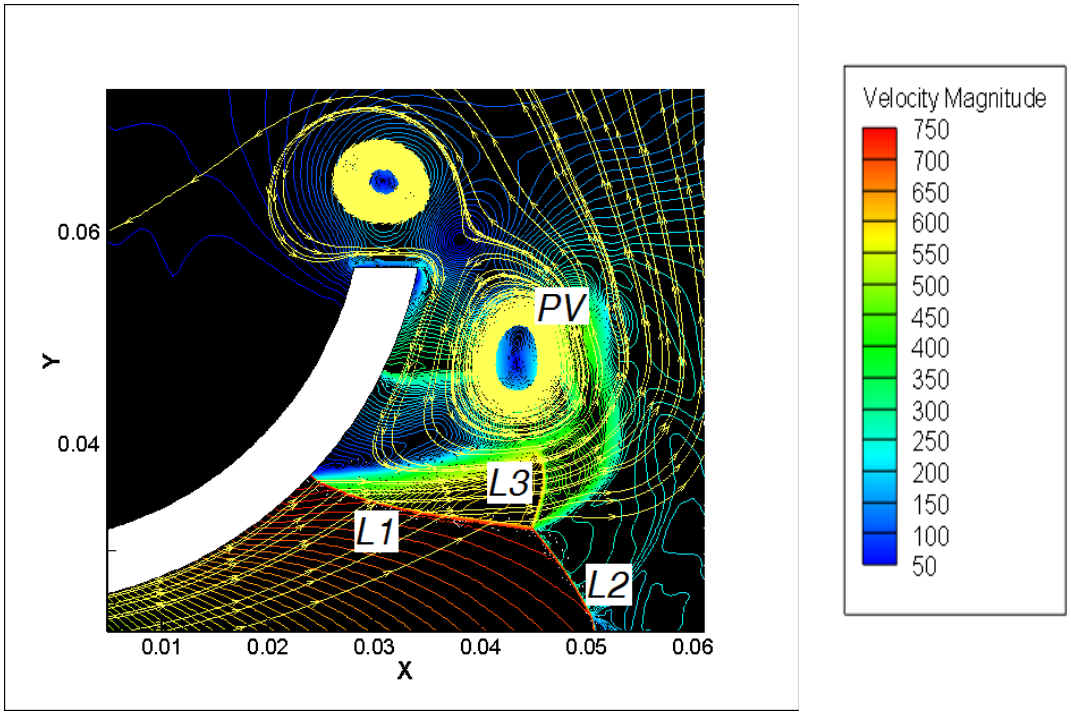


Figure 8.24: CFD velocity plot showing the shock structure in the 30mm burst pipe gap at Mach 1.6

jet at the exit plane as opposed to the ordinary pipe gap in which the flow at the exit plane of the pipe is an underexpanded jet. As a consequence the flow within the different gaps develops differently. The lambda configuration shock for the burst pipe develops relatively further upstream in the gap in comparison to the standing normal shock for the ordinary pipe gap.

8.6.2 Different pipe diameter simulation

Shock-induced flow through different pipe diameters can occurr when the pipe separation occurrs at a pipe expander or contractor. This can result in the shock wave propagating from a smaller to a larger diameter pipe.

8.6.2.1 Development of the flow

CFD density plots for are shown in Figure 8.25 for the propagation of the incident shock of Mach 1.6 from a 50mm diameter pipe into a larger 150mm diameter pipe. As the incident shock wave discharges into the 150mm pipe, it diffracts into a spherical shape as the curved expansion fan behind the shock wave approaches the axis of symmetry. A toroidal primary vortex ring is shed due to flow separation at the upstream pipe. In the second frame, the incident shock strikes the inner wall of the larger pipe and reflects back. At the same time, following the coalescing of the curved expansion fan at the axis, an expansion fan has developed at the lip of the upstream pipe. In the next frame the reflected shock wave interacts with the primary vortex ring. Upon interaction, the shock wave is split into two components. One of the components, which will be referred as shock 1, is a ring-shaped shock wave around the primary vortex ring. The second component, referred as the shock 2, has its one end sucked into the core of the primary vortex ring and the other end connected with the incident shock wave. The third frame also shows the formation of a shock wave that forms in the plane of the primary vortex ring. In the fourth frame, shock 1 converges on the axis of symmetry so that shock wave focusing on the centreline of the larger diameter pipe is generated. The fifth frame shows the second shock wave focusing due to shock 2, propagating and converging at the axis of the pipe. From the second frame to the fourth frame, it is observed that the shock wave reflection of the incident shock resulting from the shock wave focusing transited from a regular to a Mach reflection. The last frame shows the flow field at a later stage when the shear layer is broken up into a series of small vortices that move towards the primary vortex ring.

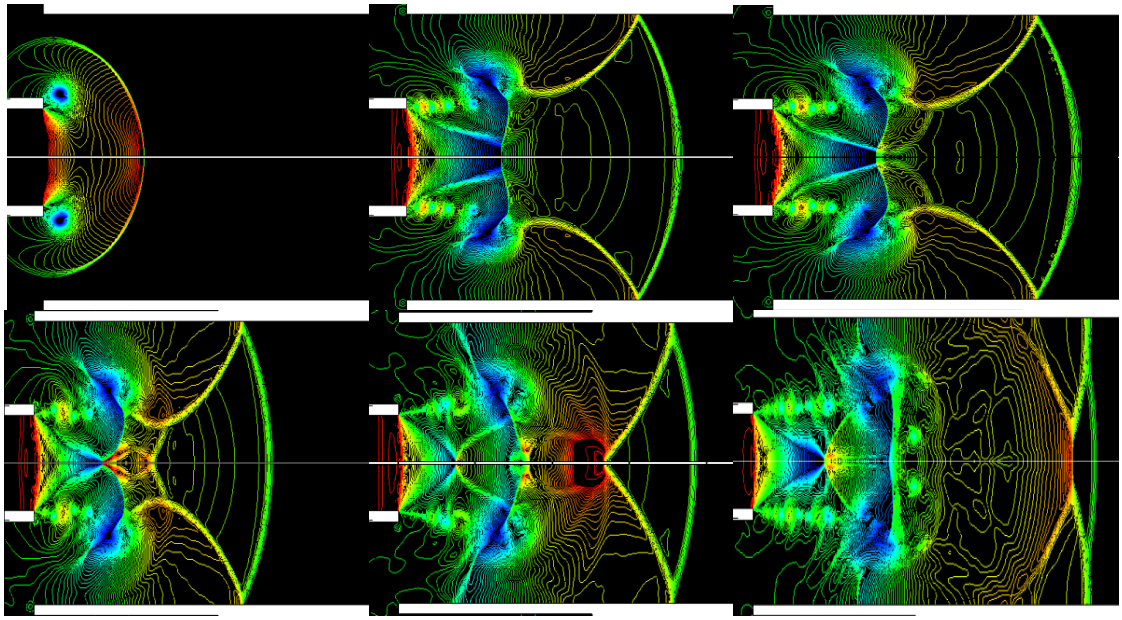


Figure 8.25: CFD density plot for Mach 1.6 shock expanding from a 50mm diameter pipe into a 150mm diameter pipe. Images at 0.2ms apart

8.6.2.2 Shock-vortex interaction

The shock-vortex interaction for the flow emerging from a smaller pipe to a larger pipe is slightly unique. The reflecting surface being at an elevated height relative to the lip of the upstream pipe, the shock-vortex interaction takes a slightly different form from the pipe gap geometry. The reflected shock is more curved and upon interaction with the vortex, the reflected shock appears to easily develop into a split two-shock wave pattern because the two ends of the curved shock wave move in different directions. For the pipe gap at a similar flow Mach number of 1.6, the reflected shock was noticed to only bend but not being split as it appeared from the shock-vortex interaction.

8.6.2.3 Shock focusing

Two instances of shock wave focusing occur for the present case. The two components of the reflected shock focus at the axis at different instances. The toroidal shock wave focusing will induce accumulation of more energy and lead to generation of a stronger jet. The jet will largely influence the flow development behind and ahead of the focal point. The reason is that the high pressure generated at the focal point will drive a spherical shock wave that affects the development of the jet.

8.6.3 Shock propagation into a 90 degree bend

Industrial gas pipe elbows and bends are usually joined together by welds. A weld is a weak point following structural loading from an explosive event. Therefore pipe separation at bends and the resulting shock-induced flow will be explored in this section.

8.6.3.1 Development of the flow

The development of a Mach 1.6 shock-induced flow past a 30mm gap and into a 90-degree bend is shown in Figure 8.26. In the first two frames, the incident shock reflects from both the inner and outer radii of the 90-degree bend. A primary vortex ring and a second vortex ring are shed at the upstream pipe and downstream pipe lip respectively. In the third frame the two vortex rings interact as they propagate radially outwards. The reflected shocks from the inner walls of the bend coalesce at the axis at the inlet to the bend. At the same time the flow in the bend develops. At the outer radius of the bend, the Mach reflection persists. Compression waves propagate upstream and towards the axis to warn the incoming flow of the convex nature of the outer radius of the bend. At the inner radius the flow develops differently. The Mach reflection of the incident shock does not persist. Instead expansion waves are reflected back into the upstream flow and towards the axis. In the fourth and fifth frame, a standing shock develops at the inlet to the bend. The compression waves and expansion waves interact in the region towards the axis of the bend. The last frame shows the shock-induced flow emerging from the bend into the vertical portion of the downstream pipe. A vortex sheds at the lip of the bend at the inner radius. The incident shock continues in the pipe with a Mach reflection persisting on the right wall of the vertical pipe.

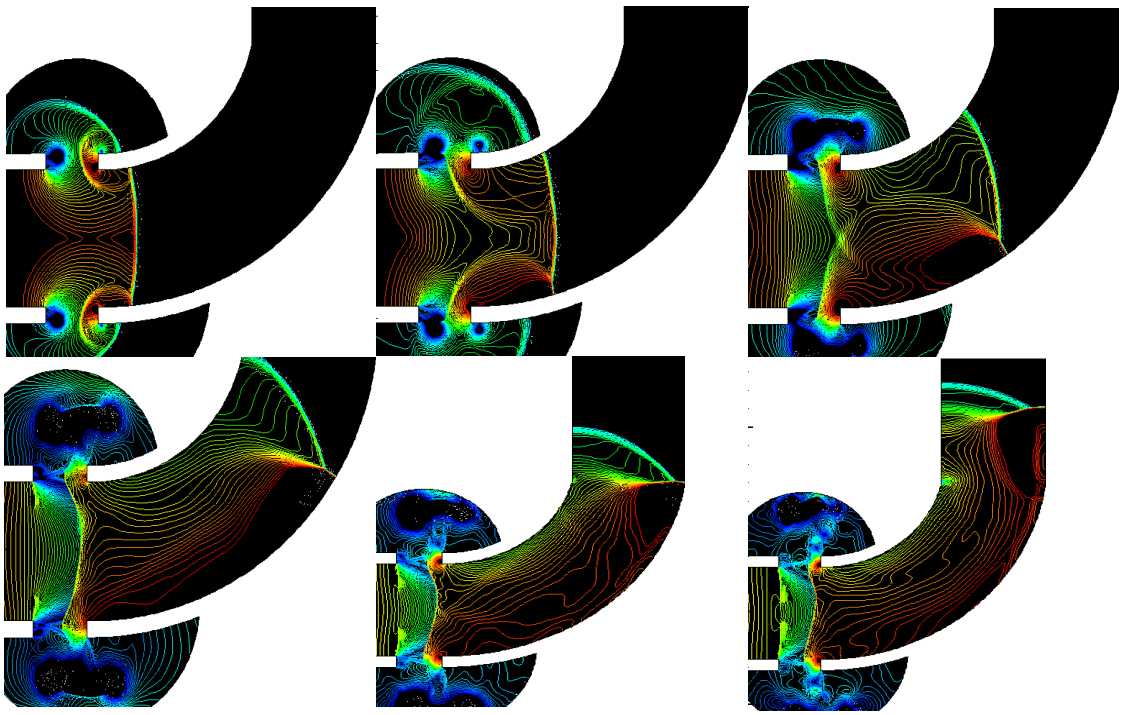


Figure 8.26: CFD density plot for shock-induced flow past a 30mm gap into a pipe bend. Images at 0.2ms apart

9 Conclusions

In addressing the objectives of the study stated in chapter 3 the following conclusions have been drawn from the analysis of experimental and numerical results.

- The passage of a shock wave through a pipe gap induced a characteristic supersonic jet from the upstream pipe for Mach 1.45 and Mach 1.6. The supersonic jet developed into shock cells of alternating shocks and expansion waves. In addition to the shock cells within the supersonic jet, one notable feature was the development of a standing normal shock at the inlet to the downstream pipe.
- For the higher Mach number of 2.2, the flow at the exit plane of the upstream pipe was supersonic. The standing shock was pushed further back into the downstream pipe.
- For the lower Mach number of 1.3, the flow did not attain a supersonic speed, as such upstream moving shocks were observed and no standing shock developed at the downstream pipe.
- For all the boundary conditions tested, they were complex interactions between the shocks waves, vortex rings and shear layers within the gap. The interactions influenced the flow evolution and the eventual transition to turbulence.
- The gap width had an effect on the nature and structure of the shock cells within the gap.
- Both the gap width and the Mach number had an effect on the propagation conditions in both pipes. Except for higher Mach number of Mach 2.2, an expansion wave reduced the post-shock pressure in the upstream pipe and the flow tends to steady state at later times. The incident shock propagated into the downstream pipe at a much reduced strength. The behaviour of the standing shock and shocks within the gap essentially controlled propagation conditions in the downstream pipe.

- The gap with flanges had the effect of confining the flow for longer and intense interactions of the different flow features leading to an earlier transition to turbulence. A

highly unsteady shock system develops in the gap. More back and forth reflections of the shock results in multiple shock-vortex interactions.

- The Numerical results also showed a different evolution of the flow for a burst pipe gap. Flow separation in the upstream pipe characterised the burst pipe simulation and the standing shock moved closer to the upstream pipe.

- For a gap with a larger diameter pipe in the downstream section it was shown that the complex morphological transformations of shock wave interaction are mainly influenced by shockwave/vortex interaction. The occurence of two reflected shocks components after the shock-vortex interaction influenced the flow in the downstream pipe. A jet generated by focusing of reflected toroidal shock waves on the axis of symmetry is found to be much stronger than that in two-dimensional cases and influences flow patterns in the central area of the expansion tube.

- Propagation of the shock into the downstream 90-degree bend pipe produced a standing shock to the inlet to the downstream pipe. On the inner concave radius expansion waves were generated whilst on the outer convex corner compression waves emanated. There was evidence of them coalescing at the centreline.

10 Recommendations

The following areas have been identified by the author to be pursued for further explorations.

1. For the numerical simulations, the use of a fluid-structure coupled solver. This can enable the simulation of the initial failure from stress waves after the explosion. The point of pipe failure and its nature are predicted by the finite element portion of the code and the subsequent shock-induced flow by the CFD solver portion. After the explosion, the behaviour of the piping material from the shock wave loading can also be predicted from the fluid-structure coupled solver.

2. For the numerical simulations, higher-order discretisation methods should be used to further refine the rich flow feature interactions within the gap flow.

3. To exactly match the pressure responses in the downstream pipe with the position of the standing shock within the gap, a synchronised measurement of the shock position and the response pressure. Multi-exposure shadowgraphy to be used to measure the shock position.

4. For the design of the shock tube, a diaphragmless shock tube should replace the diaphragm rupturing system. This will ensure operation of the shock tube with a high degree of repeatability.

5. Experimental three dimensional results should be obtained by use of a laser sheet. This will enable the visualisation of three-dimensional effects.

References

[1] Abe, A and Takayama, K (1990) "Numerical simulation and density measurement of a shock wave discharged from the open end of a shock tube." Japan Soc Mech Eng Int Journal vol. 33, p. 216.

[2] Butcher, A (1991) "The Effect of A Flange Gap on Shock Tube Performance." Masters thesis, University of the Witwatersrand .

[3] Courant, R and Friedriches, K (1967) Supersonic flow and Shock waves. New York, USA: Interscience Publishers Inc.

[4] Endo, M and Iwamoto, J (2005) "A study on shock wave formed in unsteady jet through vortex ring." Japan Soc Mech Eng Int Journal vol. 71, pp. 2928–2933.

[5] Ishii, R, Fujimoto, N, Hatta, N, and Umeda, Y (1999) "Experimental and numerical analysis of circular pulse jets." Journal of Fluid Mechanics vol. 392, pp. 129–153.

[6] Jiang, Z, Takayama, K, Babinsky, H, and Meguro, T (1997) "Transient shock wave flows in tubes with a sudden change in cross section." Shock Waves vol. 7, pp. 151–162.

[7] Kim, H, Kweon, Y, Setoguchi, T, and Aoki, T (2003) "Weak shock reflection from an open end of a tube with a baffle plate." Journal of Mechanical Science and Technology vol. 17, pp. 718–725. doi: 10.1243/095440603321919572.

[8] Klinkov, KV (2005) "Unsteady gas flows and particle dynamics in the shock layer formed by the impingement of a supersonic two-phase jet onto a plate." Phd Thesis, University of Gottingen .

[9] Love, AE (1893) "On the motion of paired vortices with a common axis." Proceedings London Mathematical Society pp. 185–194. doi: 10.1112/plms/s1-25.1.185.

[10] Panda, J (1998) "Shock oscillation in underexpanded screeching jets." Journal of Fluid Mechanics vol. 363, pp. 173–198.

[11] Simerics, ITbD (2012) "Leapfrogging Vortex Rings." Online Resource URL `http://www.simerics.com/gallery_leapfrog`.

[12] Skews, B, Platt, D, and Paton, R (2014) "Compressible flow through a ruptured pipe." 16th International Symposium on Flow Visualization vol. 7, pp. 151–162.

[13] Strutt, J and Rayleigh, Y (1878) "On the stability of jets." Proceedings of the London Mathematical society,London, 1878 vol. 10, pp. 4–13. doi: 10.1112/plms/s1-10.1.4.

[14] Sun, M and Takayama, K (1997) "The formation of a secondary shock wave behind a shock wave diffracting at a convex corner." Shock waves vol. 7, pp. 287–295.

[15] Weiss, A and Olivier, H (2014) "Shock boundary layer interaction under the influence of a normal suction slot." Shock Waves vol. 24, pp. 11–19.

[16] Zhang, S, Zhang, Y, and Chi-Wang, S (2005) "Multistage interaction of a shock wave and a strong vortex." Physics of fluids vol. 17. URL http://dx.doi.org/10.1063/1.2084233.

Appendix A Digital Appendix

The following lists shows the folders and subfolders contained on the attached CD:

- Experimental Results
  - Diaphragm calibration
  - Flow Visualisation
  - Pressure Time profiles
- CFD Simulation files
- Guide to Setup-Schliren Optical System

Appendix B Technical specifications

Table B.1: Specifications for Pressure transducers

Manufacture	**Model**	**Serial No.**	**Sensitivity [mV/psi]**	**Operating range[psi]**
PCB Piezotronics	113A21	7345	28.53	0-100
	113A21	8287	28.53	0-100
	113A21	8288	28.53	0-100
	113A21	7345	28.53	0-100

Table B.2: Specifications for Oscilloscope

Specification	**Value**
Manufacture	Hantek Electronics
Model	DSO 3064
Serial Number	5777
Software	DSO-xxxxUSB
Maximum sampling rate	200MSa/s
Trigger level	188mV
Trigger mode	Edge
Trigger sweep	Single
Trigger slope	Positive

Table B.3: Specifications for transducer signal conditioners

Manufacturer	**Model**	**Serial number**
PCB Piezotronics	F482A	4756
	F482	790

Table B.4: Specifications for the high-speed camera

Specification	**Value**
Manufacturer	Photron Fas Cam
Model number	SA5 775K-C1
Serial number	362429074
Maximum frame rate[fps]	750000
Maximum shutter speed[s]	1/1000000
Maximum resolution[pixels]	320×264

Table B.5: Specifications for the light sources

Light source	**Model**	**Pulse duration**	**Intensity[Lumens]**
Megaray high density source	Megaray	Continuous	4375
Canon camera flash	Speedlite 430EX II	1.2ms	130

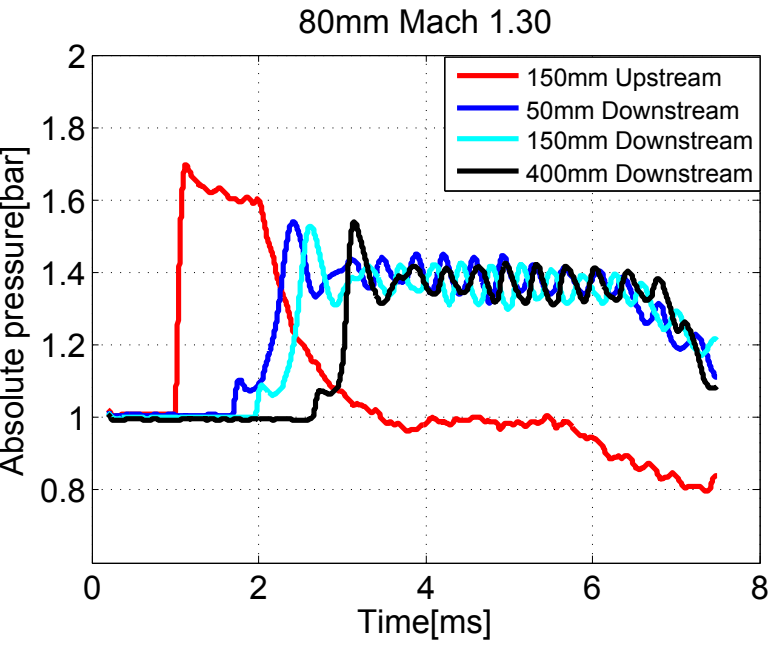
Table B.6: Specifications for the optical mirrors

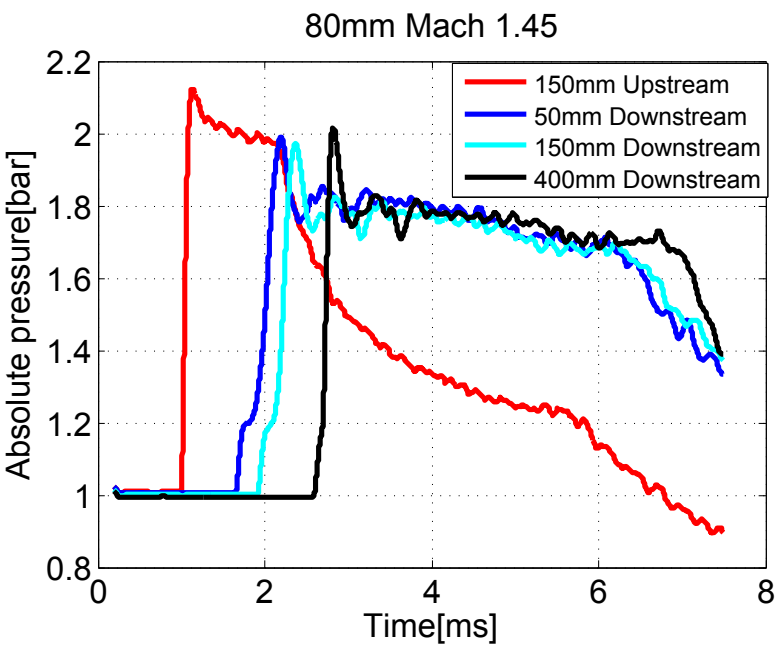
Specification	**Value**
Type	Meade Paraboloid
Diameter[inch]	16
F-ratio	4.5
Focal length[inch]	72.3
OC	3.7/5 PM

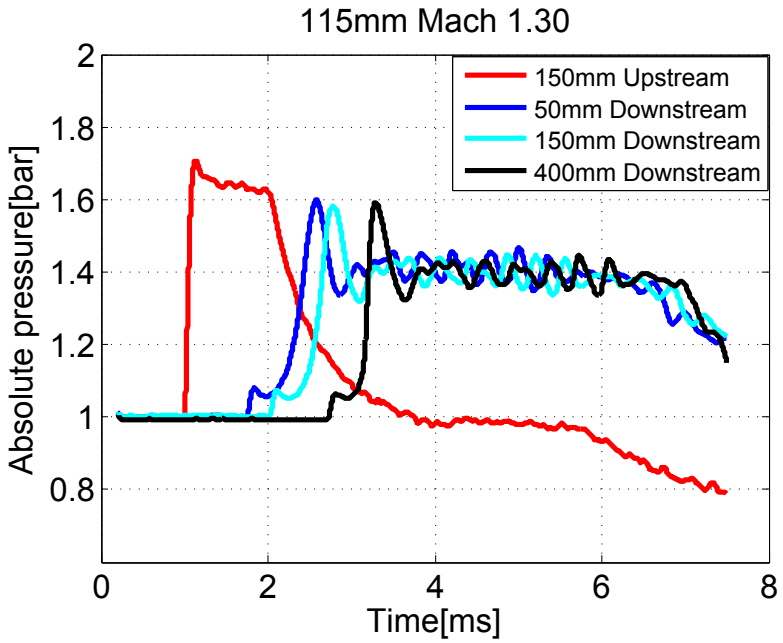
Table B.7: Specifications for the electro-delay box

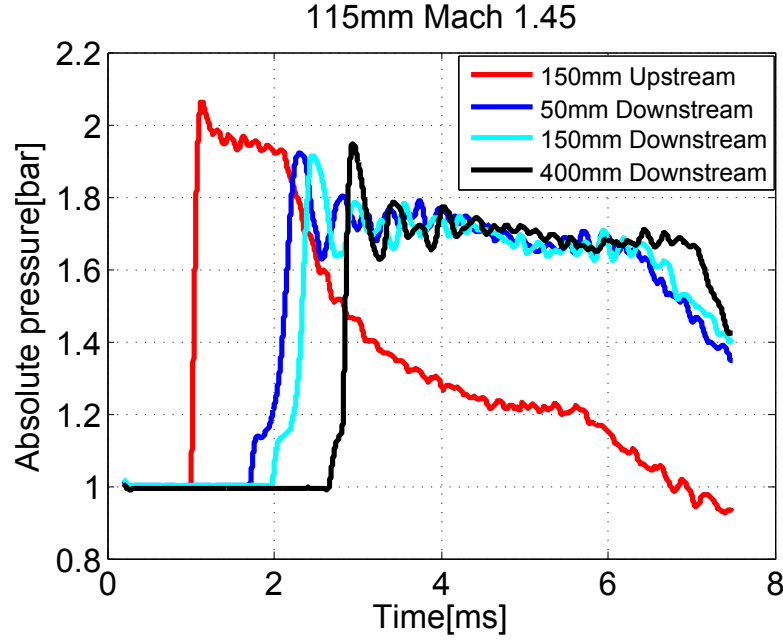
Specification	**Value**
Manufacture	Electro DI
Time delay range[μs]	50-99 998
Trigger Level range[V]	0-1
Resolution[μs]	2
Input signal	Falling Edge
Output signal	Rising Edge

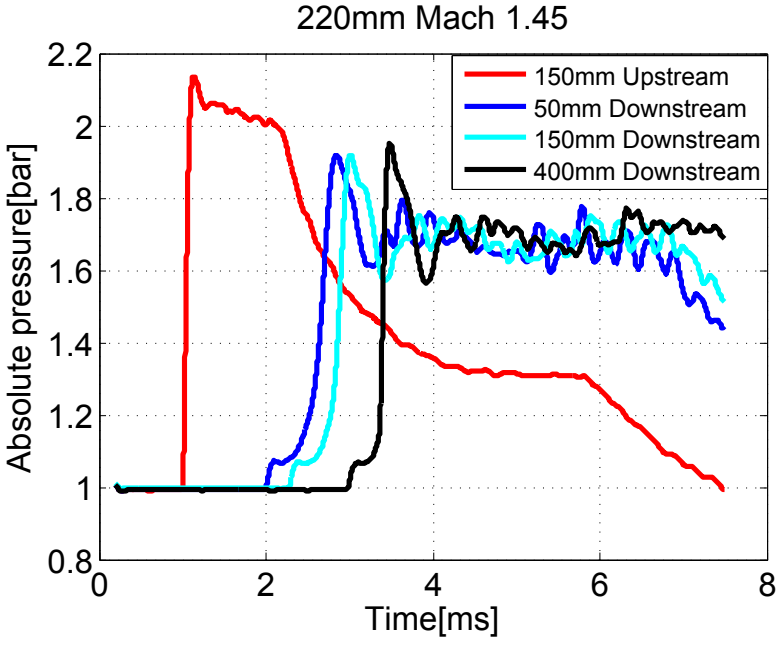
Appendix C Supplementary experimental pressure-time profiles


80mm Mach 1.30
150mm Upstream
50mm Downstream
150mm Downstream
400mm Downstream
Absolute pressure[bar]
Time[ms]


80mm Mach 1.45
150mm Upstream
50mm Downstream
150mm Downstream
400mm Downstream
Absolute pressure[bar]
Time[ms]


115mm Mach 1.30
150mm Upstream
50mm Downstream
150mm Downstream
400mm Downstream
Absolute pressure[bar]
Time[ms]


115mm Mach 1.45
150mm Upstream
50mm Downstream
150mm Downstream
400mm Downstream
Absolute pressure[bar]
Time[ms]


220mm Mach 1.45
150mm Upstream
50mm Downstream
150mm Downstream
400mm Downstream
Absolute pressure[bar]
Time[ms]

Appendix D Diaphragm calibration

Table D.1: Diaphragm calibration

Room Temp [°C]	**Number of diaphragms**	**Diaphragm thickness [microns]**	**Natural burst pressure[bar]**	**Sound speed [m/s]**	**Time between spikes[s]**	**Shock speed [m/s]**	**Shock Mach No**
22.8	1	50	5	344.9	1.18	497.45	1.44
22.8	1	50	4.8	344.9	1.20	498.17	1.42
22.8	1	50	4.8	344.9	1.18	497.45	1.44
21.8	2	25	4.8	344.32	1.16	506.03	1.47
20.2	2	25	5.0	343.38	1.18	497.46	1.45
20.4	2	25	5.2	343.50	1.16	506.03	1.47
21.2	1	25	2.8	343.97	1.27	462.2	1.34
21.4	1	25	2.6	344.08	1.30	451.54	1.31
21.6	1	25	2.8	344.20	1.28	458.59	1.33
22.2	2	50	8.8	344.55	1.07	548.60	1.59
22.2	2	50	9.4	344.55	1.05	559.05	1.62
22.6	2	50	9.0	344.79	1.06	553.77	1.61
22.6	2	50	8.8	344.79	1.06	553.77	1.61
21.6	3	25	7.2	344.20	1.09	538.53	1.56
21.8	3	25	7.6	344.32	1.09	538.53	1.56
21.8	3	25	7.0	344.32	1.12	524.11	1.52

Appendix E Mach number uncertainity

Equation(E.1) expresses the Mach number, M_s in terms of the transducer separation distance, x, the time,t between the pressure spikes as the shock passes the respective pressure transducers and T is the absolute temperature.

$$M_s = \frac{x}{t\sqrt{\gamma RT}} \tag{E.1}$$

The uncertainties for the relevant quantities measured are shown in Table E.1

Table E.1: Individual uncertainties for Mach number calculation

Measurement	**Symbol**	**Uncertainity**
Temperature[K]	$\triangle T$	$\pm$ 0.1
Transducer separation[mm]	$\triangle x$	$\pm$ 0.5
Time between spikes[ms]	$\triangle t$	$\pm$ 0.01

The uncertainty calculation for M_s is derived from the method of Holman and is shown by equation(E.2) .

$$\frac{\triangle M_s}{M_s} = \sqrt{(\frac{\triangle x}{x})^2 + (\frac{-1\triangle t}{t})^2) + (\frac{-0.5\triangle T}{T})^2} \tag{E.2}$$

Using the values obtained from the first calibration test as shown in Table D.1 and substituting in equation (E.2) :

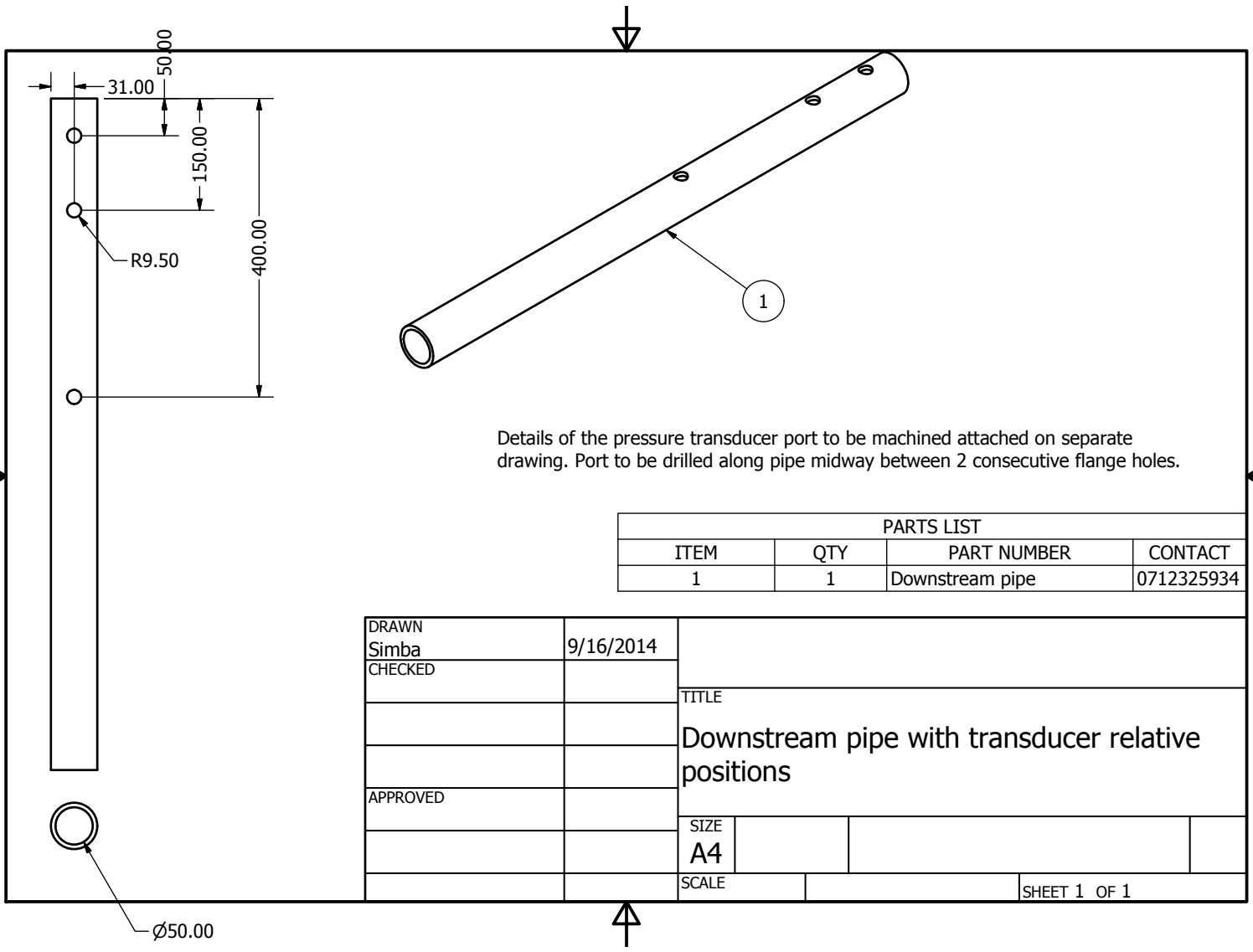
$$\frac{\triangle M_s}{M_s} = 0.0116 \tag{E.3}$$

Therefore, $\triangle M_s = \pm 0.0151$.

Appendix F Engineering drawings

Engineering drawings are presented on the pressure transducer positions, details for the transducer installation ports and the shock tube supports. All the manufacturing was conducted by the staff within the Mechanical Engineering Laboratory at the University of the Witwatersrand. The drawings are presented in the following order:

1. Pressure transducers positions- page 106
2. Pressure transducer installation port(the flush mounting)- page 107
3. Shock tube supports- page 108
    - Flange bracket- page 109
    - Resting rod- page 110
    - Slotted bottom plate- page 111
    - Leg support for the shock tube support- page 112



Details of the pressure transducer port to be machined attached on separate drawing. Port to be drilled along pipe midway between 2 consecutive flange holes.

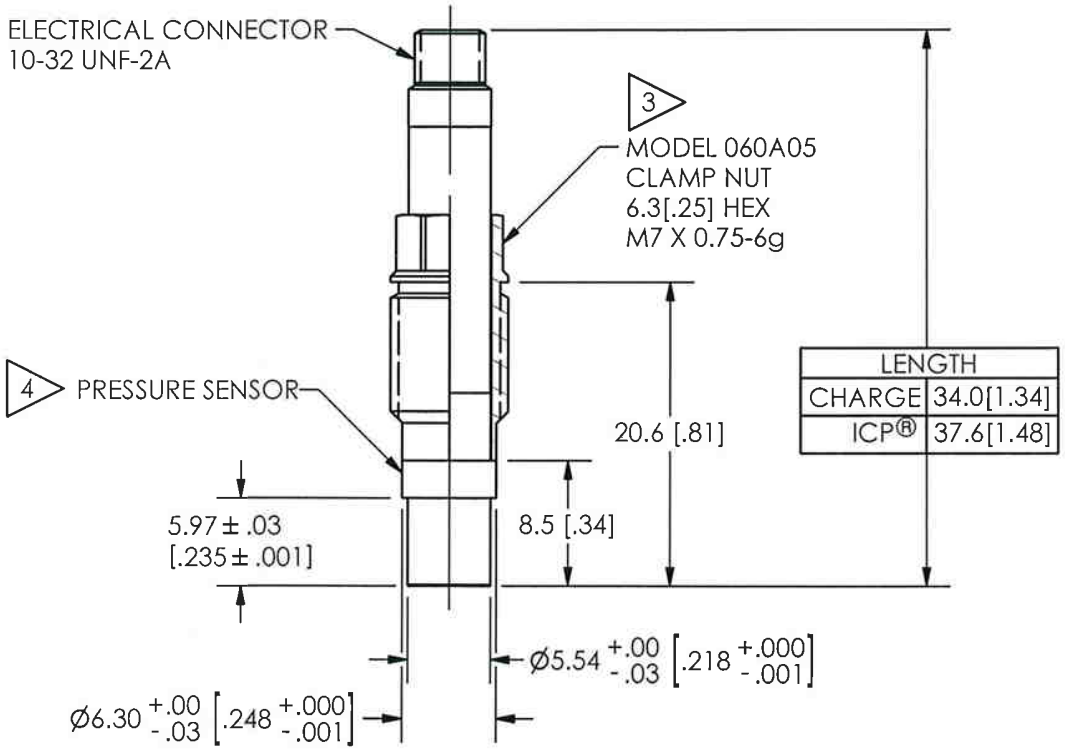
PARTS LIST			
ITEM	QTY	PART NUMBER	CONTACT
1	1	Downstream pipe	0712325934

DRAWN Simba	9/16/2014	
CHECKED		TITLE: Downstream pipe with transducer relative positions
APPROVED		SIZE A4
		SCALE
		SHEET 1 OF 1

PCB Piezotronics Inc. claims proprietary rights in the information disclosed hereon. Neither it nor any reproduction thereof will be disclosed to others without the written consent of PCB Piezotronics Inc.

40623

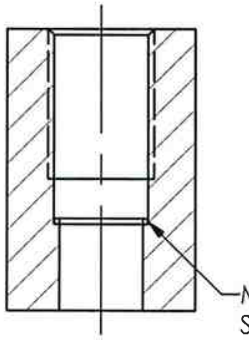
REVISIONS			
REV	DESCRIPTION	ECN	APP'D
	- SEE SHEET ONE -		mDF 8/6/08



MOUNTING HOLE PREPARATION

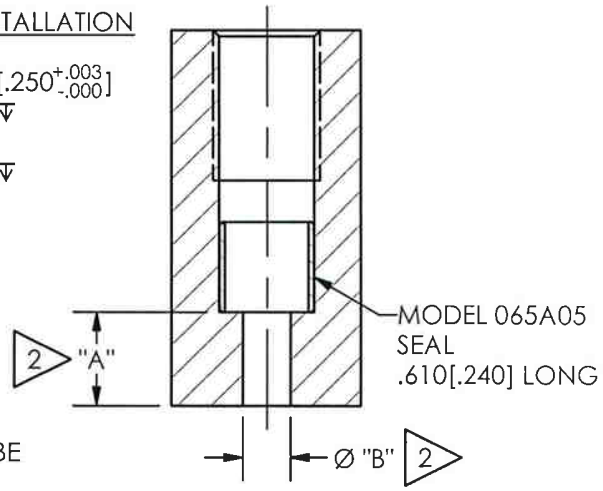
1 FLUSH INSTALLATION

Ø5.61± .05[.221±.002]
THRU
⌴Ø6.35 +.08 -.00 [.250 +.003 -.000]
X 13.20[.520] ↧
M7 X 0.75-6H
X 10.16[.400] ↧



RECESSED INSTALLATION

⌴Ø.635 +.08 -.00 [.250 +.003 -.000]
X 19.05[.750] ↧
M7 X 0.75-6H
X 10.16[.400] ↧



4 IC AMP AND SENSOR ARE SEALED ASSEMBLIES AND SHOULD BE RETURNED TO THE FACTORY FOR SERVICE AND/OR REPAIR.

3 RECOMMENDED TORQUE ON 6.3[.25] HEX: 2.8-3.9 Nm[25-35 IN. LBS.].

2 DIMENSIONS "A" AND "B" TO SUIT USER REQUIREMENTS.

1 THESE DIMENSIONS FOR 19.05[.750] THICK WALL. COUNTERBORE FOR THICKER WALLS.

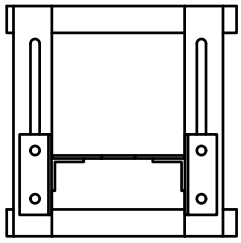
UNLESS OTHERWISE SPECIFIED TOLERANCES ARE:	
DIMENSIONS IN INCHES [IN BRACKETS]	DIMENSIONS IN MILLIMETERS
DECIMALS XX ± .01	DECIMALS X ± 0.3
XXX ± .005	XX ± 0.13
ANGLES ± 2 DEGREES	ANGLES ± 2 DEGREES
FILLETS AND RADII .003 - .005	FILLETS AND RADII [0.07 - 0.13]

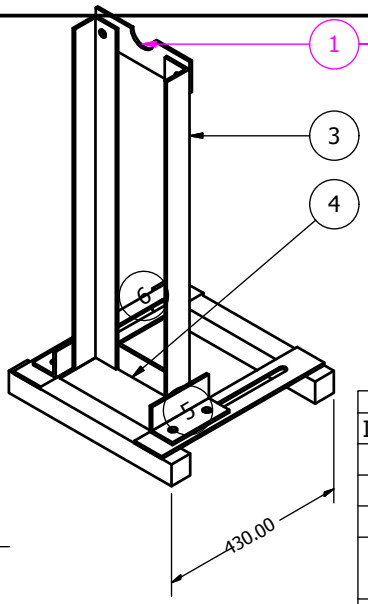
DRAWN	mDF	8/6/08	MFG	P.R.R	8-7-08
CHK'D	mDF	8/6/08	ENGR	RF	8/8/08
APP'D	[illegible]		SALES	KW	08/08/08

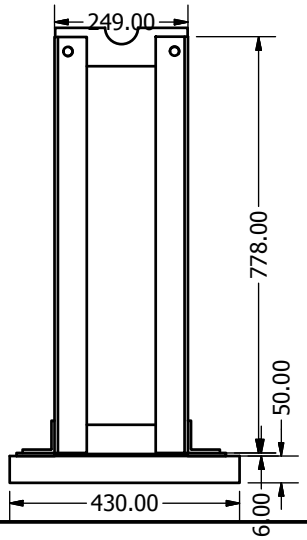
TITLE: INSTALLATION DRAWING
METRIC MOUNT
MODELS 113B SERIES
PRESSURE SENSOR

PCB PIEZOTRONICS INC
3425 WALDEN AVE. DEPEW, NY 14043
(716) 684-0001 E-MAIL: sales@pcb.com

CODE IDENT. NO.	DWG. NO.	
52681	40623	
SCALE: 2 X	SHEET 2 OF 2	



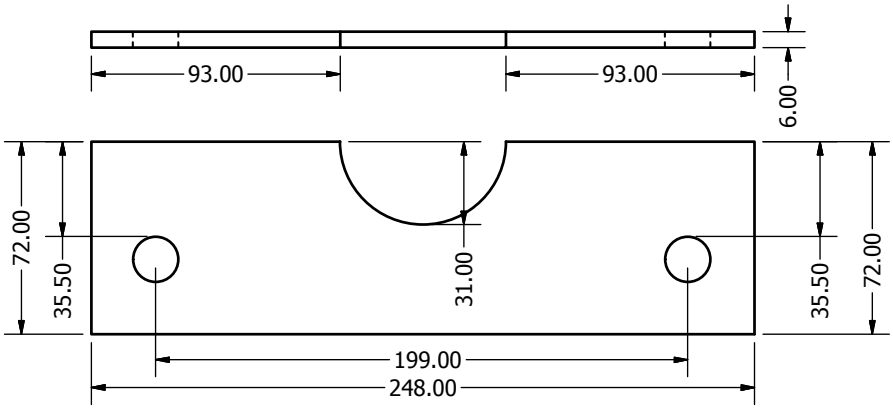


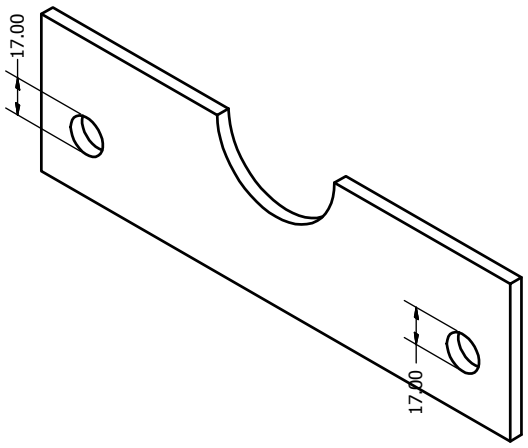


PARTS LIST			
ITEM	QTY	PART NUMBER	DESCRIPTION
1	1	Flange_Bracket_Shocktube	
2	1	Pipe_Leg_Shocktube	
3	1	PipeLeg2_ShockTube	
4	1	BottomCrossMember_Shocktube	
5	2	restingrods3	
6	2	Slotted_Bottom	
7	2	FixedBottomRods	

DRAWN Simba	9/12/2014		
CHECKED		TITLE	
QA		Pipe Support_Shock Tube	
MFG			
APPROVED			
		SIZE A4	DWG NO Pipe_Support_Assembly
		SCALE	SHEET 1 OF 1

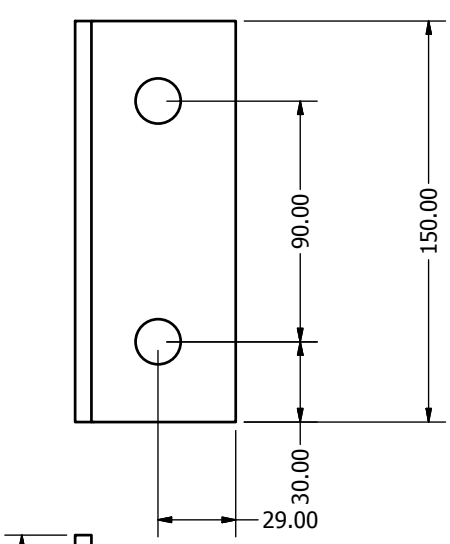
PARTS LIST			
QTY	MATERIAL	SCALE	CONTACT
2	MILDSTEEL	1:2	0712325934

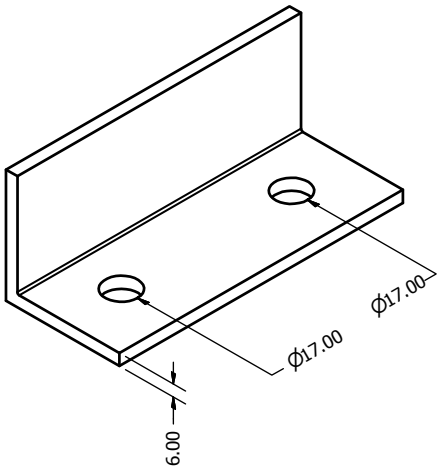


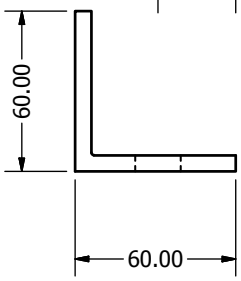


DRAWN SIMBA	9/8/2014	FLANGE BRACKET
CHECKED		TITLE
		SIZE
APPROVED		A4

SHEET 1 OF 1

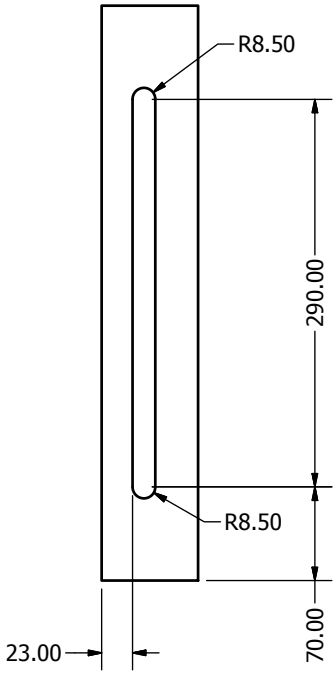


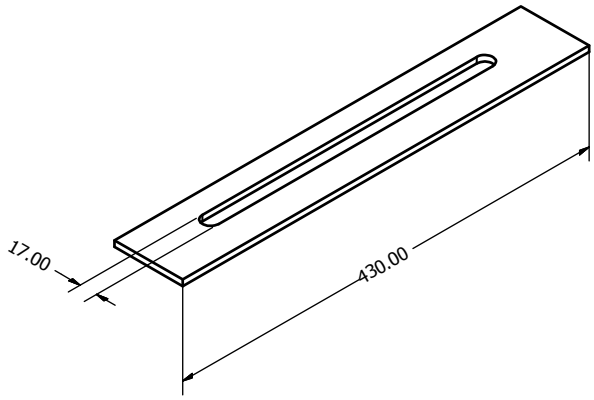


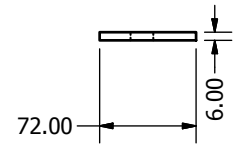


PARTS LIST			
QTY	MATERIAL	SCALE	CONTACT
4	MILD STEEL	1:2	0712325934

DRAWN Simba	9/12/2014	
CHECKED		TITLE Resting Rods
APPROVED		SIZE A4
		SHEET 1 OF 1

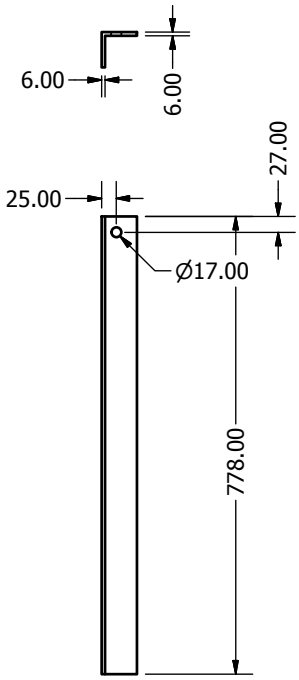


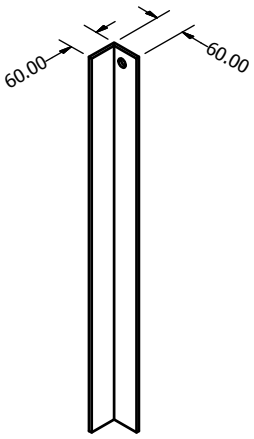




PARTS LIST			
QTY	MATERIAL	SCALE	CONTACT
4	MILD STEEL	1:4	0712325934

DRAWN Simba	9/12/2014	
CHECKED		TITLE
		Slotted Bottom Plate
APPROVED		SIZE A4 / REV
		SHEET 1 OF 1





PARTS LIST			
QTY	MATERIAL	SCALE	CONTACT
2	MILDSTEEL	0.11:1	0712325934

DRAWN SIMBA	9/8/2014	
CHECKED		TITLE
		LEG FOR SHOCK TUBE SUPPORT
APPROVED		SIZE A4
		SHEET 1 OF 1